Synthesis and Characterization of Novel non Noble Metal Catalysts for the Electrocatalytic Oxygen Reduction Reaction

Vorgelegt von
MSc.Chem. Nastaran Ranjbar Sahraie
Shiraz, Iran

von der Fakultät II-Mathematik und Naturwissenschaften
der Technischen Universität Berlin
zum Erlangen des akademischen Grades

Doktorin der Naturwissenschaften
Dr. rer. nat.

genehmigte Dissertation

Promotionsausschuss:
Vorsitzender: Prof. Dr. T. Friedrich (TU Berlin)
Berichter: Prof. Dr. P. Strasser (TU Berlin)
Berichter: Prof. Dr. C. Roth (FU Berlin)

Tag der wissenschaftlichen Aussprache: 27. März 2014
Berlin 2014
D83

Abstract

Renewable energy sources have received large attentions which target a clean energy revolution in near future. In particular, environmental driving forces and growing energy demands continue for renewable energy conversion. Polymer electrolyte membrane fuel cells (PEMFCs) and alkaline fuel cells (AFC) fed with pure hydrogen gas or hydrogen-rich fuels from renewable sources are appealing substitutes for conventional combustion engines in portable devices. Pt and Pt-alloy supported on carbon are currently used in cathodes and anodes of PEMFCs. High loadings of Pt in the cathode are necessary to surmount the intrinsically sluggish kinetics of ORR These high loadings mean high costs and are a substantial hurdle for widespread mass production of affordable FC-powered vehicles. Hence, there is a necessity for increasing the Pt mass specific activity of the catalyst by lower the Pt content through its alloying with other metals or developing novel Pt efficient material like core-shell structures. However, substituting precious metals with non noble metal catalysts (NNMCs) while maintaining high ORR activity and stability remains a critical long-term goal. To achieve this goal, an improved fundamental understanding of catalytically active structural features (active sites) in NNMCs is indispensible. During several last decades, a significant progress has been achieved in the synthesis, performance and understanding of the mechanism. Among many catalyst formulations, numerous nitrogen, metal and carbon precursors were used to synthesize different catalysts. It has been shown that these NNMCs are material-based, implying that it is necessary to investigate the catalytic activity of new precursor combinations to achieve higher activity. In this thesis, I have explored a number of different novel heteroatom (N, S, B) - doped and non noble metal containing carbon materials. I have systematically studied the influence of nature of the metal, nitrogen precursor, heteroatom, support type, synthesis strategy and synthesis parameters on the catalytic activity of the final catalysts. Additionally, by using a probe molecule, I have achieved a correlation between activity and surface site density, which enabled a deeper insight into the catalytic active site structure.

Zusammenfassung

In dieser Dissertation wurden neuartige Heteroatom-Nichtedelmetall-Kohlenstoff basierte Hybridkatalysatoren synthetisiert und diese anschließend physikochemisch und elektrochemisch charakterisiert. Die Arbeit untersucht systematisch den Einfluss von verschiedenen Syntheseparametern auf die elektrochemische Reaktivität für die Elektroreduktion von molekularem Sauerstoff. Es wurden verschiedene polymerbasierte Stickstoff Precursoren eingesetzt und ihren Einfluss auf den Stickstoffeinbau in die Hybridkatalysatoren untersucht. Der Einfluss des Übergangsmetalls und dessen Beladung wurde ebenfalls näher analysiert. Neuartige synergistische Effekte zwischen Übergangsmetallen wurden identifiziert, welche die Stabilität der Katalysatoren deutlich verbesserte. Es wurden auch der Einfluss von anderen Heteroatomen wie Schwefel, Phosphor und Bor auf die Struktur und die Reaktivität der Hybridkatalysatoren untersucht. Es wurde weiterhin eine neuartige, auf Kugelmühlen-basierende Synthesemethode entwickelt, die die Synthese hochaktiver Katalysatoren deutlich vereinfacht. Es wurden neuartige Katalysatoren entwickelt, die deutlich über der Sauerstoffreduktionsaktivität von Platinreferenzkatalysatoren lagen. Eine Adsorptionsmethode wurde angewendet, die eine Abschätzung der aktiven Oberflächenplatzdichte erlaubt und so eine direkte Korrelation zwischen aktiven Zentren und Aktivität ermöglicht. Insgesamt liefert diese Arbeit einen neuartigen Beitrag zum Verständnis der Synthese-Struktur-Aktivitätsbeziehungen von Nichtedelmetall-Katalysatoren für Brennstoffzellkathoden.

Die vorliegende Arbeit wurde unter der Leitung von Herrn Prof. Peter Strasser in der Zeit vom 1.1.2010 bis zum 17.3.2014 im Fachbereich Chemie am Institut für Technische Chemie der Technischen Universität Berlin angefertigt. Die praktischen Arbeiten wurden unter der Leitung von Frau MSc. Nastaran Ranjbar Sahraie

Contents:

1. Introduction 5

1.1. Goals, objectives and structure of this thesis 7

1.2. Acidic and Alkaline Hydrogen Polymer Electrolyte Fuel Cells (PEFCs) and Fuel Cell Electrocatalysis 10

1.3. State-of-the-Art Metal/Nitrogen/Carbon Biomimetic Analogs for ORR Catalysis 13

2. Experimental Part 24

2.1. Catalyst synthesis. 24

2.1.1. Carbon support pretreatment. 24

2.1.3. Electrode Preparation and Rotating Disk Electrode (RDE) Setup 30

2.2. TEM/SEM Characterization 36

2.3. BET Measurements 36

2.4. ICP Measurements 37

2.5. XRD Characterization 37

2.6. X-ray photoelectron spectroscopy (XPS) Characterization 38

2.7. Temperature Programmed Desorption (TPD) and Pulse Chemisorption Measurements 38

2.8. Thermo Gravimetric Analysis (TGA) 40

2.9. Elemental Analysis (EA) 40

3. Activity and Stability of Polyaniline-based non-noble Metal Catalysts for Oxygen Reduction Reaction (ORR) 41

3.1. Introduction 41

3.2. Motivation 41

3.3. Results and discussion 42

3.4. Conclusion. 68

4. Activity and Stability of Hexamethyltetramine (HMTA)-based catalyst synthesized via ball milling for ORR 69

4.1. Introduction 69

4.2. Motivation 70

4.3. Results and discussion 71

4.4. Conclusion

5. Heteroatom-doped Carbon derived from Ionic Liquids (ILs) with Tunable Enhanced ORR Performance: Nitrogen and Sulfur-/Phosphorus-/Boron- Co-Dopped Ketjen 96

5.1. Introduction 96

5.2. Motivation 97

5.3. Results and discussion 97

5.4. Conclusions 119

6. Activity and Stability of Carbonized Polyformamidine (PFA) for Oxygen Reduction Reaction 120

6.1. Introduction 120

6.2. Motivation 120

6.3. Results and discussion 121

6.4. Conclusion 133
7. Conclusions and Perspectives 135
8. List of Figures
9. List of Tables
10. Appendix

1. Introduction

The global energy challenge, with regarding population and economic growth, need to be managed and meet demand affordably, sustainably and securely. Limited fossil fuel energy supplies for future and climate policies to limit greenhouse gases, in particular, carbon dioxide (CO_2) promote the motivation for utilizing clean and renewable energy sources. The specification of a power-electronic interface is subject to few requirements related on one side to the renewable energy source and on the other side to its effects on the power-system operation. In this context, hydrogen (H_2) is a potentially emission-free alternative that can be produced from domestic resources. Fuel cells (FCs) as the devices which convert directly chemical energy into electrical energy are appealing substitutes for the conventional combustion engines in portable devices [1, 2]. The key drives for global investigations in fuel cell mobile technology stem from crucial features: i) pollution-free energy conversion; ii) more than two orders of magnitude efficiency (20-25 %) and iii) quiet operation with fewer moving parts compared to that of traditional combustion technologies [3, 4]. Polymer electrolyte membrane fuel cells (PEFCs), in particular proton exchange membrane fuel cells (PEMFCs), fed with pure hydrogen gas or hydrogen-rich fuels from renewable sources are largely under investigation as they can be simply utilized in cars [2, 5]. In this context, hydrogen (H_2) as a potentially emission-free alternative for fossil fuels can fulfil the key requirements of future energy resources [6, 7]. In the late of 1980s, department of energy (DOE) prompted the activities supporting its technology, especially for zero-emission vehicles [8].

Pt and Pt-alloy [9-11] electrocatalysts supported on carbon are currently used in cathodes and anodes of PEMFCs. High loadings of Pt in the cathode are necessary to surmount the intrinsically sluggish kinetics of ORR [12].These high loadings result in high costs and are the substantial hurdle for widespread mass production of affordable fuel cell-powered vehicles. Besides, due to Pt particle degradation, catalysts are not stable in operating conditions [13, 14]. Accordingly, on one hand, increasing the stability of Pt catalysts as a short term goal is attracting a lot of attention. On the other hand, substituting Pt as precious metal with non noble metal while maintaining high ORR activity and stability, remains critical in long term. Lately, few works were reported on stabilization of Pt nanoparticles on N-doped carbon supports which was attributed to the

interaction of Pt NPs and the heteroatoms doped on carbon support surface. Most likely, immigration, growth and agglomeration of the particles are hindered by fixing on N-doped materials[15, 16].

In order to replace Pt catalysts with cheap and naturally available materials, first row transition metals (Fe, Co, Mn, Cu or Ni) in conjugation with carbon/nitrogen ligand atoms created a family of non noble metal catalysts (NNMCs). These materials showed a comparable activity to Pt-based catalysts in acid electrolyte while their activity in alkaline medium is superior to Pt [17]. These catalysts imitate the molecular structure of a bio-inspired metal porphyrine ring active site in cytochrom molecules which are responsible for oxygen respiratory chain in nature [18]. Beginning in early 1960s Jasinski et al. [19] and Yeager et al.[20] reported the ORR activity of cobalt phthalocyanine in alkaline medium. Later Jahnke et al. [21] also showed the ORR activity of this macromolecule catalyst in acid environment. While very first catalysts suffered from low activity and stability, high temperature heat treatment and their supporting on high surface area carbons drastically increased their performances [22, 23]. Finally, the replacement of expensive macromolecules with metal, nitrogen and carbon precursors and their heat treatment brought about ORR electrocatalysts which are economically affordable. Thereafter, NNMCs have been extensively studied as promising long-term alternatives to Pt-based electrocatalysts for PEMFCs and alkaline fuel cells (AFCs) [24-28].

Studies on NNMCs showed that, assuredly, the nature of the metal is a determining factor in catalytic activity of these catalysts [18]. Apparently, iron is creating the most active materials while usually a bimetallic system including iron and typically cobalt exhibit a higher stability [17]. Additionally, numerous nitrogen precursors were used for syntheses of NNMCs which result in different activities of the final products [29-32]. In particular, there is one specific family of these materials based on electro-conductive heterocyclic polymers such as polyaniline (PANI) [17, 33] and polypyrole (PPY) [34] which have attracted the attention of researchers over the past 10 years. In these heterocyclic compounds, the molecules can be the source of carbon and nitrogen simultaneously. However, usually direct carbonization of these molecules result in low active catalysts and they need to be supported on high surface area carbons to show desired performances.

Although nitrogen is the mostly investigated element in non noble metal catalysis, it

was shown that other heteroatoms such as S, P and B can serve the same functionality to create ORR active materials. The nature of the heteroatom and the doping degree regulate the catalytic activity of the catalysts. [35-38]. It is noteworthy to mention that heat treatment (pyrolysis) of any mixture of nitrogen/metal/carbon precursors would result in a catalyst with ORR activity; however the achieved activity and stability depends largely on selection of precursors and synthesis strategy.

Special groups of sites with differently defined structures on which the ORR takes place are called active sites. The structures of NNMC active sites were investigated for first-reported macromolecules as their exact molecular structures were known [18, 39-41]. However, these structures are not well-understood in heat-treated catalysts due to the full decomposition of the precursors at high temperatures [42-48]. Therefore, the precise structure of the active sites, their robust formations in sufficient densities and their stabilization in NNMCs which are formed during high temperature pyrolysis are challenging issues in non noble metal catalyst research area. Correspondingly, one key question is whether metal is present in the active site or just participates in catalyst formation and thereafter is removed by leaching step. This unresolved challenge about the role of metal in the active site chiefly originates from the lack of suitable *in situ* techniques to probe the chemical composition and reactivity of the active site. A number of molecular probes, such as cyanide [49, 50] and carbon monoxide [50-54] were used to obtain insight into the nature of the active surface sites. Some of these studies relied on the poisoning interaction between the probe molecule and central metal ions under electrochemical environments. However, results remained inconclusive as no interaction was resolved.

In this thesis, we focused on acidic and alkaline PEFCs. They use hydrogen and can be manufactured in portable dimensions, meaning low weight and volume.

1.1. Goals, objectives and structure of this thesis

In order to address the replacement of Pt-based catalysts with highly performance NNMCs in acid and alkaline media, this thesis focused on the design of novel non noble metal materials using different precursors and synthetic parameters/strategies. The composition/morphology-ORR activity correlation provides us a better understanding of the nature of the active sites and their densities in different materials. Accordingly, we

explored the effect of various parameters including nature of the metal, precursor type, heteroatom, and support as well as mixing strategies including wet impregnation and ball milling (BM). All the synthesized catalysts were characterized physico-chemically and subsequently tested for electrochemical performances (activity and stability). After performance measurements towards ORR electrocatalysis, the most interesting samples were selected and tested by spectroscopic techniques to achieve deeper insight into metal and heteroatom chemical environments. Figure 1 outlined the individual work packages of this thesis.

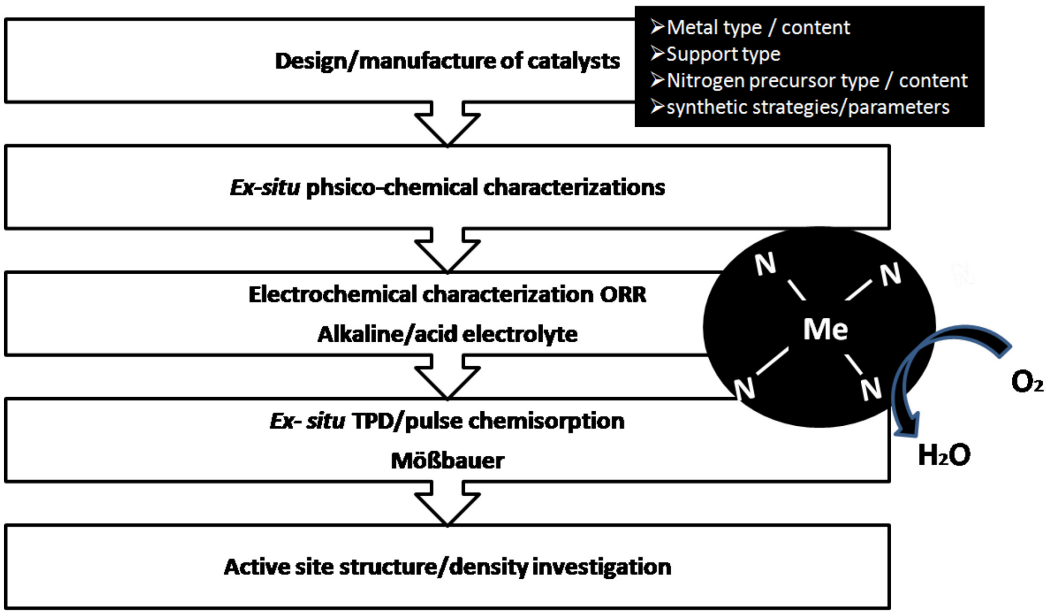

Figure 1. Individual work packages of this thesis.

To achieve this goal and due to the intrinsic higher activity of NNMCs in alkaline medium, initially, ORR activities of the synthesized materials were extensively assessed in alkaline medium. Thereafter, the best performing materials were tested in acid for PEMFC applications as well as their stability was investigated in both, acid and alkaline media. All the catalytic performances were compared with Pt 20 wt% as the reference catalyst. We hypothesize that, 1) the introduction of second metal in a bimetallic catalyst, 2) application of physicochemical ball milling mixing strategy and utilization of nitrogen rich precursor, 3) application of second heteroatom in a co-doped material and 4) carbonization of nitrogen containing polymer could result in active ORR catalysts with improved performances to that of state-of-the-art reported catalysts.

This thesis is structured into 6 chapters. After introduction and review on the subject, chapter 2 describes the experimental details of synthesis and instrumental characterization -physico-chemical and electrochemical- for the materials tested in chapters 3-6.

In chapter 3, our hypothesis was tested for how the introduction of second metal influences the ORR performance (activity and stability) bimetallic manganese-iron/polyaniline/carbon catalysts compared to monometallic, iron and manganese catalysts. Accordingly, the ORR activity and stability of various catalysts with different metal loadings and Mn:Fe molar ratios were investigated. Thereafter, the role of the support morphology and surface area for the best performing catalyst composition was explored. Moreover, to obtain insight into the active site structure, carbon monoxide was used as a probe molecule in temperature programmed desorption (TPD) and pulse chemisorption techniques to correlate the ORR activity and CO adsorption on catalyst surface. Nitrogen chemical environments in the final catalysts were followed by XPS spectroscopy technique.

In chapter 4, our hypothesis was tested for the influence of synthesis strategy and nitrogen content on the final activity of the catalysts. Accordingly, a novel synthetic procedure for the preparation of active non precious ORR catalysts is utilized. Two new aspects are explored. First the use of involving ball milling (BM) as a way to intimately mix the precursors, and secondly, the use of hexamethyltetramine (HMTA) as nitrogen source with high N/C ratio. Ball milling is a dry way to mix the metal, nitrogen and carbon support precursors and very different compared to wet impregnation for the materials from chapters 3, 5 and 6. In particular, the role of ball milling on catalyst morphology as well as achieving homogeneous nitrogen doping was investigated. Another innovation is the use of hexamethyltetramine precursor with high nitrogen percent which was used to correlate the nitrogen content of starting precursor and final doping degree. Additionally, the role of catalyst morphology originated from the ball milling effect on mass transfer and diffusion properties of the materials was studies. To the best of our knowledge, this is the first time that hexamethyltetramine (HMTA) was used as a nitrogen precursor for synthesis of an ORR electrocatalysts.

In chapter 5, our hypothesis was tested for the influence of heteroatom nature on the final ORR activity of the catalysts. Correspondingly, ionic liquids (ILs) with different heteroatoms were used to prepare and explore (co)doped carbon materials including

nitrogen-doped and nitrogen-boron/sulfur/phosphorous co-doped catalysts. Ionic liquids were used to functionalize the commercial carbon support. The ORR performances of these catalysts were correlated with the nature of the heteroatoms and physico-chemical characteristics. To the best of our knowledge, this is the first time that ionic liquids were used for doping of commercial carbon and not directly as the carbon source.

In chapter 6, the direct carbonization of unsupported polyformamidine as a nitrogen containing polymer was investigated. In particular, the influence of synthetic parameters, such as metal loadings, calcination temperature and time was correlated with catalytic activity of the materials.

1.2. Acidic and Alkaline Hydrogen Polymer Electrolyte Fuel Cells (PEFCs) and Fuel Cell Electrocatalysis

The concept of fuel cell dates back to 1839 from independent studies by Grove [55] and Schoebein [56]. Fuel cell functionality is identical to battery for obtaining electrical energy from chemical energy, but unlike a battery, reacting chemicals can be supplied to the electrodes and therefore the electrical power can be sustained as long as fuel and oxidant are provided. Fuel cells are classified primarily by the kind of electrolyte they employed and depending on their dimension can be manufactured for mobile or stationary applications. This classification determines the chemical reactions that take place in the cell, the appropriate catalyst, the temperature range in which cell operates in the optimum condition and most importantly the fuel required. These characteristics, in turn, affect the applications for which the corresponding devices are most suitable. There are six leading groups of fuel cells under investigation in twenty first century: Proton exchange membrane fuel cell (PEMFC), alkaline fuel cell (AFC), direct methanol fuel cell (DMFC), phosphoric acid fuel cell (PAFC), molten carbonate fuel cell (MCFC) and solid oxide fuel cell (SOFC). While stationary fuel cells can be used for backup power, distributed power generations and cogeneration, mobile fuel cells are attracting great interests for vehicles. These devices, in particular PEMFCs and AFCs, can be used almost in any application which typically uses batteries and generators such as special personal vehicles, mine vessels or space ships [5, 57]. As the only by-products, pure water and heat are reproducing which are further useful. Figure 2 shows a representative schema of acid and alkaline fuel cells. At the first glance, the major

differences are half cell reactions (cathode and anode) and the diffusing electrolyte species through the membranes.

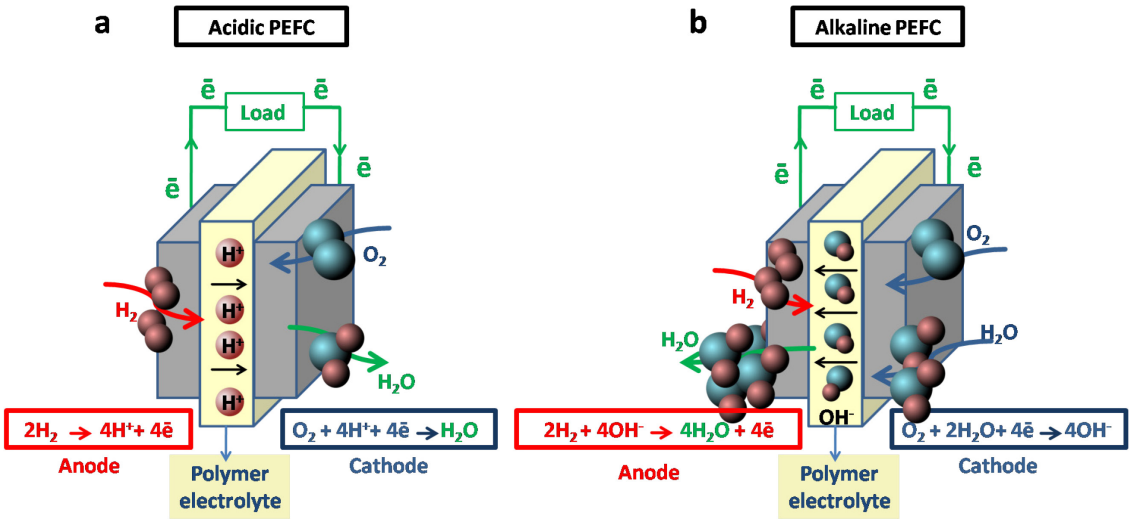

Figure 2. Schematic of a) acidic, b) alkaline PEFCs and corresponding anodic/cathodic reactions.

The simple overall reactions of a hydrogen/oxygen PEFC in acid and alkaline is depicted in Figure 2 (a) and (b) respectively. In acidic PEFC, on the anode side hydrogen as fuel is oxidized to protons and on the cathode side oxygen as oxidant is reduced to water by producing heat. Solid membrane separates the half reactions and transfers proton from the anode side to the cathode side. Contrary, membrane in AFC transmits hydroxide ions from the cathode side to the anode side. On the cathode, oxygen is reduced to hydroxide ions, which are transmitted by membrane to the anode side and react with hydrogen to produce water [5, 57]. These fuel cells operate at relatively low temperature (80 °C) which enables them to start-up quickly. For the operation, they should only be fed by oxygen at the cathode as the oxidant and hydrogen at the anode as the fuel. PEMFC and AFC are compared in more details in Table 1 [5, 57].

Table 1. Comparison of the acidic and alkaline PEFCs [5, 57].

Parameter	Acidic PEFC (PEMFC)	Alkaline PEFC (AFC)
Fuel feedstock	H_2-natural gas (at high temperatures)	H_2
Oxidant	O_2-air	O_2-air
Ion transferred	H^+	OH
Common electrolyte	nafion®	-Aqueous solution of potassium hydroxide soaked in matrix -Solid membrane electrolyte (name)
Operating temperature/°C	25 to 90	25 to 90
Common catalyst	Pt nanoparticles @ carbon support	Pt-Ni-non-noble metal
Efficiency	~58 %	~64 %
Typical electricity output	<250 kW	<20 kW
Applications	-Backup power (stationary application) -Specialty vehicles	-Military -Space
Advantages	-Solid electrolyte reduces corrosion & electrolyte management problems -Low temperature -Quick startup -Commercially available membrane	-Potential application of non noble metal catalysts with high activity in alkaline electrolyte -Improved cathode performance -Low cost components
Disadvantages	-Expensive catalysts and membrane -Sensitive to fuel impurities -Low temperature waste heat -Humidity dependence -Low sulfur and CO tolerance -Humidity dependence	-Sensitive to CO_2 in fuel and air -Electrolyte management -No commercially accessible anion exchange membrane -Carbonate precipitation

It is well justified to claim that PEMFC and AFC show approximately same performances. [58, 59]. However, it has to be mentioned that while Pt-based catalysts are highly active in acid electrolyte, their performing in alkaline medium is disadvantageous from both cost perspectives and kinetic points of view due to high hydrogen peroxide generation. Since the 1950s alkaline fuel cells (AFCs) were used for

space flights by NASA [59, 60], While at the very beginning, interest in alkaline fuel cells (AFCs) failed chiefly due to the leakage of electrolyte and carbonate precipitation poisoning effects. Recent researches in exploring solid anion exchange membranes and their replacement with liquid electrolytes in conventional AFC for hydroxide anion made a renaissance in alkaline fuel cell technology [61-63]. Furthermore, recently-developed non-Pt catalysts from very cheap starting precursors showed not only high activity at cathode for ORR in alkaline but also noteworthy tolerance to methanol or other cross over impurities in fuels.

1.3. State-of-the-Art Metal/Nitrogen/Carbon Biomimetic Analogs for ORR Catalysis

Life exists only through constant dissipation of energy while respiration is one of the basic concepts of this energy metabolism. Although decay of molecular oxygen as a four-electron/four-proton ($4\bar{e}/4H^+$) oxidant to water (H_2O) is a thermodynamically favorable reaction, due to its very sluggish kinetic, respiration proceeds only thanks to enzyme-catalyzed electron transfer between respiratory electron carriers. All these enzymes, such as cytochroms or hemoglobin, contain a binuclear porphyrine binuclear heme-Cu or mononuclear heme active site at which O_2 is reduced [18, 64].

Work on non noble metal catalysts (NNMCs) for the ORR electrocatalysis in PEFCs started in 1980 by a significant effort aimed at replicating this reactivity in artificial systems containing a heme (Fe)/Cu unit. First, the research focused on biomimetic studies in electrode-confined Fe porphyrins inspired from enzymes [65-67]. By early work of Jasinsky [19] who reported for the first time that cobalt phtalocyanine is ORR active in alkaline, pure metallomacromolecules or complexes (MeN_x, x=1-4) were used directly as ORR catalysts. These initial works were aimed almost exclusively at designing metal porphyrine compounds that, when immobilized on electrodes, would catalyze electrochemical O_2 reaction to H_2O regardless of their electrochemical potential or lifetime. These usually insoluble catalysts were deposited on the graphite disk as a film of poorly defined morphology either by spontaneous adsorption from a solution or by evaporation of the catalyst solution aliquot onto the electrode surface. Their activities could be influenced by the nature of the central metal and the ligands [68]. Usually, simple metal porphyrines (Me-N_4 chelates) degrade rapidly during catalytic O_2 reduction due to leaching of metal into electrolyte. Hence, they suffered from poor

stability, particularly in acid media. Supporting these complexes on carbon or graphite followed by high temperature heat treatment (pyrolysis) could not only increase their activity but also extensively stabilized the catalysts [69-71]. ORR activities of pure metal porphyrine molecules were directly attributed to the central metal. On the contrary, for heat-treated catalysts, it is more difficult to identify the active site structure due to the decomposition of molecules. Therefore, the nature of active surface sites has remained broadly controversial [42-48]. In 1988, Gupta et al. [72] used for the first time cheap nitrogen precursor, polyacrylonitrile, for synthesis of a Co/N-doped electrocatalysts which had supposedly the similar porphyrine type centers as active site. Later, these expensive macromolecules were succesfully replaced by various combinations of nitrogen-containing compounds, transition-metal inorganic salts and carbons which recently led to the catalysts with high ORR activity comparable with Pt; however their stabilities need further improvements [17]. Apparently, any selection of nitrogen/carbon/metal which goes through high temperature pyrolysis can show a degree of ORR activity. Noteworthy, a deeper insight to the exact structure of active site, its formation and strategies to increase the site density are the crucial issues for non noble metal catalysts.

The concept of special active site and its density on catalytic surfaces was introduced by Taylor in 1925[73]. The likelihood of actual existence of such centers and their probable chemical nature has been extremely discussed but still there is not a worldwide agreement about it for different materials. Although it has been accepted that in a great number of cases, catalytic reactions do indeed take place on special groups of sites with differently defined structures, representing a fraction of the total surface, in this manner called the active sites. Such an active site is the source of material functionality. Accordingly, a material exhibits function if it possesses chemical or physical functionality.

Reported literature mostly nominates two different viewpoints about the active site moieties for ORR in NNMC materials: i) metal-centre [74-76] and ii) metalfree-centers [45, 77-85]. For metal-center active sites, various theories were previously proposed by van Veen et al. [86-88], McBreen et al. [89], Schulenburg et al. [90], Scherson et al. [53] and Dodelet et al. [28, 91-98]. Some studies suggested the structures similar to the very incipient catalysts Me-N_x macrocycles like phthalocyanine (Pc) and porphyrine complexes/chelates in which non noble metal coordinated with variable number of

nitrogen atoms. This view was based on the enzyme molecular structures known to do oxygen reduction under physiological conditions. In molecular form, the metal centers which are connected to nitrogen atoms intrinsically exist. Since the metal complexes showed a well-defined molecular structure of metal complexes before pyrolysis, numerous investigations were performed on them to clarify the role of metal. It has been clearly shown that the mechanism of the reaction is very sensitive to the nature of the metal center in complex. Phthalocyanines with Fe and Mn at the center, promote 4-electron reduction, whereas Co, Ni and Cu phthalocyanines only promote 2-electron reaction. This effect confirms that electron density around metal center can dictate the reaction pathway. In addition to electron density, the catalytic activity of metal macrocyclic complexes has also been linked to the redox potential of Me (III)/(II). According to these reports, the driving force of ORR reaction can be correlated with the Me(III)/Me(II) formal potential of the catalyst [18]. A volcano-shaped curve have been obtained which shows the correlations between activity and the M(III)/(II) formal potential (see Figure 3) . Apparently, the redox potential of metal needs to be located in a defined potential window to achieve maximum activity, implying too positive or too negative potentials are not favorable for an active ORR catalyst.

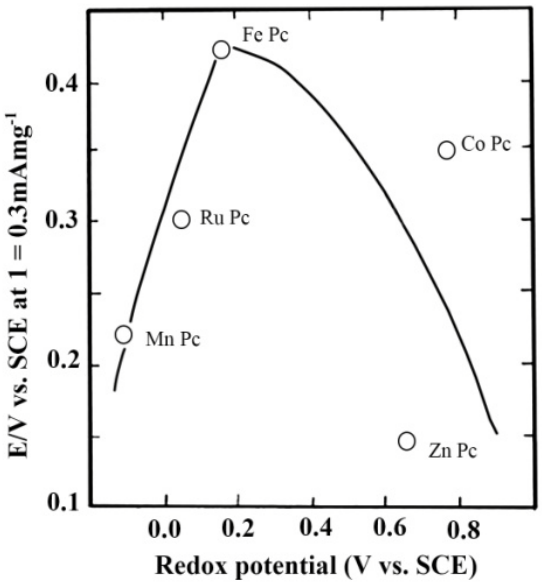

Figure 3. Volcano plot for ORR electrocatalysis of various metal phthalocyanines [18].

This shows that the metals which are difficult to oxidize (more positive standard redox potentials) as well as the metals which are easily oxidized (more negative standard redox potentials) are not appropriate catalysts for ORR. [18]. Apparently, among non noble metals, iron is the best performing metal, while manganese and cobalt occupying lower positions in volcano plot (see Figure 3) [18].

The active centers (Me-N_x) can be created during high temperature pyrolysis of metal and nitrogen precursors. If the molecules are supported on carbon, these centers are hosted in the micro/meso pores of high surface area carbon backbone. As it was mentioned previously, predicting the active sites of these catalysts is more difficult due to the decomposition of starting precursors[19, 24, 77, 91, 92, 99-112].

In contrast to the view for existence of metal in the active site structure, mainly evidenced on the ORR activity of nitrogen doped carbon nanostructures[113-119], some researchers proposed active site without coordinated metal ions [14, 120-122]. For quite some time, there was considerable doubt that a metal free catalyst for ORR existed, until Lalande et al. could show the unique influence of the nitrogen doping to the catalytic activity of carbon materials [96]. Thereafter, in 2006, ORR activity of metalfree N-doped material was reported by Matter et al. and Ozkan et al.[123]. Based on these ORR reports, it was suggested that the metal solely catalyze the ORR active site formation. In other words, it only promotes the creation of highly graphitized and N-functionalized nanostructure matrix with increased edge plane exposures which primarily contain carbon and nitrogen. Thereafter, metal is removed from the catalyst through acid leaching step and consequently does not take part in ORR [44, 124-126]. In these materials, plain carbons can be doped with heteroatoms, implying the chemical attachment of heteroatoms to the carbon backbone without any coordination with metal. According to this concept, doping or functionalizing can be a target-motivated procedure to stimulate specific characteristics of the carbon particularly its charge density profile. These characteristics can be electrical conductivity, stability or the reactivity of the material for different chemical reactions. The number of heteroatom functional groups which are incorporated into the carbon framework (doping degree) is an important controlling parameter for such characteristics. Nitrogen is by far, the most widely investigated heteroatom dopant. Interestingly, a mere doping degree of ~10% (nitrogen on carbon) drastically changes the properties of the carbon material compared to non-doped analogues. Density functional theory based on quantum mechanical

calculations indicated that due to the higher electronic affinity of nitrogen atoms, the carbon atoms adjacent to them possess increased positive charge density[127-129]. Indeed the number of reported metalfree nitrogen-doped carbons with different functionalities including ORR performances is nearly uncountable [130] although even in these nanomaterials, the positive effect of metal in functionalization, activation and stabilization of the resulting catalysts is clearly proved [42, 77, 91, 131-136].

This topic can be summarized as, all these reports evidence that metalfree compounds are indeed somewhat ORR active. However, it is now widely agreed that the presence of metal ions in the starting precursor materials results in the creation of active sites in which metal centers are coordinated to nitrogen groups. or graphitic surface [137].

Assuming that the presence of metal ions in the active site structure is critically necessary, the following fundamental questions arise which are largely unanswered to date: what is the location of the active site on the carbon support, i.e. on the edge versus in plane positions, what is the coordination number, x, and the oxidation state of the metal ion (Me-N_x) as well as what is the chemical environment of nitrogen groups (pyridinic, pyrrolic, graphitic and quaternary) [75, 76]. Depending on the type of heteroatom, the doping degree and the nature of bonding to the carbonaceous backbone the material properties vary significantly. In this context, the chemical environment of the incorporated heteroatom, such as nitrogen, is crucial to control the properties of the entire catalyst material. Basically, two types of nitrogen can be distinguished: chemical nitrogen and structural nitrogen. The former refers to the surface functionalities, such as amine or nitrosyl groups. The latter indicates nitrogen directly bonded into the backbone of the carbon material and can be named as graphitic, quaternary, pyridinic and pyrollic. The term quaternary has raised criticism among some material chemists, as this nomenclature suggests a sp^3 hybridized positively charged N atom in a tetrahedral bonding environment. In contrast, the quaternary nitrogen, shown in Figure 4, remains sp^2 hybridized, i.e. is planar. This is why the term graphitic nitrogen, which is typically used for nitrogen incorporated into the graphene at non-edge positions, is sometimes preferred for this type of bonding.

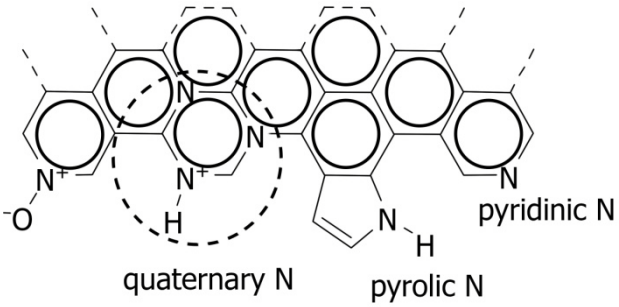

Figure 4. Schematic overview on possible nitrogen bonding sites on a carbon backbone.

The role of structural nitrogen to modify the carbon properties is dominant as it can more effectively influences the electron charge of carbon materials. Mukerjee et al. showed that graphitic structural nitrogen is the most active position of nitrogen in carbon backbone for ORR [76].

The chemical preconditions of other heteroatoms are not perfectly adapting for incorporation into carbonaceous materials. Nevertheless, the electronic situation in boron or the size of second row elements like sulfur and phosphorous make them appropriate candidates for doping of carbon[35-37].

Limited knowledge on active site structure of non-noble metal catalysts chiefly originates from the lack of suitable techniques to probe these site structures. In literature, different probes have been used to answer this challenging question, whether metal is present in the final active site or not. Different anionic or molecular probes, mainly cyanide [49, 50] and carbon monoxide [50-54] were used, which altogether addressed the macrocycles with or without experiencing high temperature treatment such as Fe-porphyrines and Fe-phthalocyanines. These studies are mainly based on the postulated interactions between these species and the metals in the active sites result in their potential poisoning effect on the electrocatalysis in rotating disk electrode (RDE) measurements. Electrochemical findings showed no CO adsorption or oxidation peaks in saturated electrolyte with CO. Additionally, there is nearly no change in the capacitive current features by switching from N_2 to CO[138]. In two recently published works an endeavor was devoted to explore the reversibility influence of CO adsorption based on the fact that Fe-porphyrines have dominant affinity for CO than Oxygen. In

these works electrochemical results for CO poisoning effect were in parallel with previously reported works [82, 139, 140], meaning no deactivating effect was detected.

It should be mentioned that in some studies, the catalytic ORR activity of Me/N/C samples has been also attributed to the iron carbide or iron nitride crystalline phases which are formed during the pyrolysis. These structures can be detected by powder X-ray diffraction (XRD) technique [141].

While the exact structure of the active site remains under debate, it is generally agreed that increasing the active site density can increase the catalytic activity. Assuming the critical role of heteroatom and metal in active center structure, doping degree and catalyst surface area influence the active site density. Additionally, it should be taken into regard that metal not only participate in active site but can catalyze the doping, therefore its initial (nominal) content can be quiet crucial in the formation and the final density of active sites [141].

Recently it was pointed out by Bezerra et al [142], when developing of catalysts with higher activities and stabilities by optimizing the synthetic pathways is at the center of attention, performing more fundamental studies on NNMCs are necessary. For Pt-based catalysts, based on numerous fundamental electrochemical investigations, kinetic studies on single crystals and in situ spectroscopy techniques, the ORR mechanism has been well-explored for both acid and alkaline electrolytes [143]. For non-Pt catalysts, however, the details of the ORR pathway or mechanism are less understood. Again, the rotating disk electrode method has been aiding our understanding of the ORR pathways on the NNMCs. The first model for ORR pathway was developed by Damjanovic et al. [144, 145] which was extended by further work of Wroblowa et al. [145] and Anastasijevic [146]. Mukerjee et al. [75] reported that the ORR reaction pathway can be an inner-sphere reaction involving more than one electron which needs a strong interaction of dioxygen with the active site on the electrode surface. The inner sphere mechanism implies chemisorption of the reactants on the catalyst surface. On the other hand, there are studies evidencing that the ORR reaction can also proceed through the outer-sphere reduction. This involves the transfer of two electrons across a hydration shell to molecular oxygen that is not molecularly adsorbed on the surface, in order to produce hydrogen peroxide. In other words, the outer-sphere process does not involve any oxygen interaction with the electrode surface and is totally independent of nature of catalyst [76]. As the 4ē pathway is favorable for ORR, therefore the necessity to promote

the inner-sphere electrocatalytic process by increasing oxygen adsorption is doubtlessly critical. On one side, the potential of the electrode and on the other side the catalyst nature can affect the interaction of molecular oxygen with electrode [75].

Generally, the ORR process shows mechanistic differences in alkaline and acid conditions. On non-noble metal catalysts, it was reported to be more facile in alkaline media compared to acid conditions. In order to understand the ORR pathways and investigate the rationale behind the more facility on non-noble metal catalysts in alkaline, it turned out useful to follow the effect of pH change on adsorption/desorption process at electrode interface [25].pH changes from acidic to alkaline conditions drastically influence the electrode potential which would in turn affect the double layer properties as well as the adsorption strength of different species. Correspondingly, the effect of working electrode potential on electrostatic attraction/repulsion interaction of different species and intermediates as well as their adsorption strength should be taking into account [147, 148]. Mukerjee et al. [76] proposed the mechanistic difference in alkaline and acid media. In a typical aqueous acidic/alkaline electrolyte with 0.1 M concentration, the double layer is assumed to be composed of the inner-Helmholtz plane (IHP) and the outer-Helmholtz plane (OHP) as depicted in Figure5.

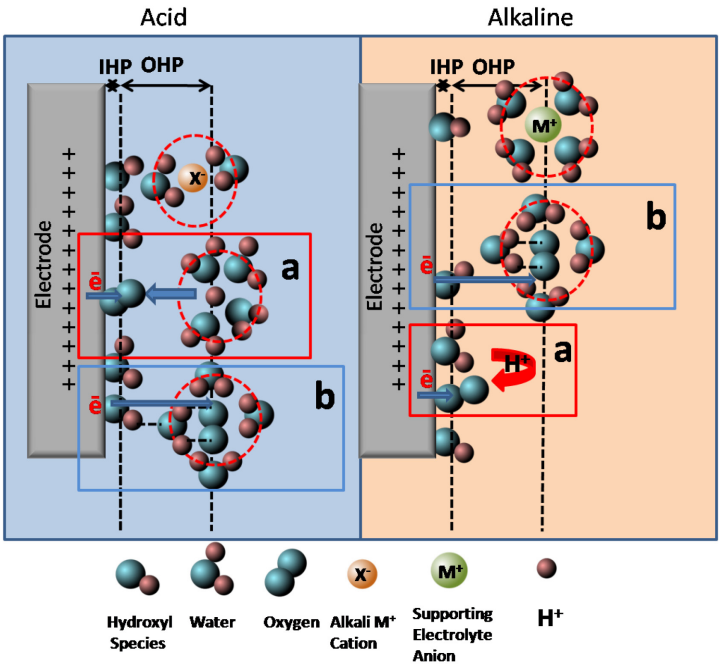

Figure 5. Schematic illustration of the double-layer structure during ORR in acid (left) and alkaline (right) conditions. Insets (a) inner-sphere and (b) outer-sphere electron transfer processes [75].

In oxygen saturated 0.1 M $HClO_4$, IHP is composed of chemisorbed molecular O_2, adsorbed hydroxyl species (OH_{ads}) and solvent water dipoles. On the other side, solvated molecular O_2 and ClO_4^- anions constitute the OHP. Clearly, protons (H_3O^+cations) populate the electrolyte as well. It is reasonable to assume that the cathode potentials during oxygen reduction in an operating fuel cell condition are positive of the potentials of zero charge (pzc) that is the potential where no net charges are present inside and just outside the double layer.

For potentials positive of the pzc, H_3O^+ distance is limited to OHP due to the repulsion of corresponding positive charges. The first electron transfers to adsorbed molecular oxygen to form superoxide (O_2^-), thereafter protonation of this superoxide is only likely by transfer of H_3O^+ from OHP to IHP. Due to the very high mobility of H_3O^+, this step is occurring very fast and cannot be the rate determining step. For an active ORR electrocatalyst, formed intermediates remains adsorbed on the catalyst active site to undergo 4ē and $4H^+$transfer and the final product (water) is released. The double layer electrostatic features are mostly identical in alkaline and acid double layer (see Figure 5a-alkaline). The only significant difference can be attributed to water molecules in alkaline media. At high pH values water molecules are not passive as solvent molecules but serve as the proton source for ORR. Hence for providing proton, there is no necessity to H_3O^+ species transfer from OHP to IHP, as the IHP is populated by water molecules. In this way, the progress of the ORR is facilitated by the presence of proton donor from adsorbed or solvated water molecules. After the first electron transfer to adsorbed dioxygen molecule from the electrode surface, superoxid can be reduced by any adjacent water molecule. Additionally, in alkaline media, due to the more negative electrode surface charge, adsorbed OH^- can be more easily replaced by O_2 molecules which in turn facilitate the ORR regarding that oxygen adsorption is prerequisite for this reaction.

Another reason which facilitates the ORR in alkaline is attributed to the potential change in different pH. By changing the pH to near 13 (for alkaline), the potential of proton containing redox couples changes by about ~ 0.83 V, this decrease in overpotential in alkaline media implies that strong chemisorption of O_2 to the electrode surface is not necessary and non-covalent forces such as long-term dipole-dipole interactions can also be sufficient. Formed superoxide is observed at E° = -0.3±0.03 V vs. SHE with corresponding$\Delta G°$= 30±2 kJ mol^{-1} with both O_2 and O_2^- in aqueous

solution [146, 149]. The potential of this redox couple (O_2/O_2^-) is independent of pH and remains unchanged by changing the electrolyte from acid to alkaline media. Contrary, the standard potential of another redox couple (H_2O/OH^-), changes from 1.229 V to 0.41 V vs. SHE as pH changes from 0 to 14. Blizanac et al. [150] proposed that significant decrease in overpotential for the first electron transfer in alkaline media is the main thermodynamic reason that a wide range of compounds can be used in alkaline media for ORR reaction. This unspecific outer-sphere pathway is the reason for the possibility of using a wide range of non noble metals and their oxides as electrode materials for ORR in alkaline media.

NNMCs are not only more active in alkaline electrolyte, but the 4ē transfer pathway is favored in this electrolyte. It has to be mentioned that outer-sphere electron transfer to from superoxide O_2^- is also contributing as the following equation1 shows:

$$O_{2(aq)} + \bar{e} \rightarrow (O_2^-)_{aq} \qquad E° = -0.33\,V\ vs.\ SHE \qquad (equation\ 1)$$

$$O2aq + \bar{e} \rightarrow \left(O2^{\overline{\ }}\right)aq \qquad E° = -0.33\,V\ vs.SHE \qquad (equation\ 2)$$

This higher selectivity for 4ē pathway in alkaline compared to acid electrolyte can be followed in Figure 5(b). In acid, usually even at high overpotentials no clear diffusion-limited region could be discerned, which hinted to the kinetic control in the whole potential range. On the contrary, a well-defined mixed kinetic-diffusion region is observed for alkaline electrolyte. These observations clearly indicate that peroxide reduction in alkaline media is kinetically favored such that any peroxide intermediate can be promptly reduced to water [76]. This is attributed to the strong binding of hydrogen peroxide on the active site which stabilizes this molecule on the electrode and facilitates further electron transfer. Oppositely, reduction of H_2O_2 in acidic media is not kinetically favorable which originates from weak binding to the active site and fast desorption from the electrode. Mukerjee et al. [76] demonstrated that stabilizing hydrogen peroxide as the ORR intermediate on active site is crucial to promote the 4ē ORR pathway. Likewise, the higher stabilities of these intermediates give rise to the so-called kinetic facility in alkaline media. This process can be explored regarding the pK_a values of H_2O_2 in stepwise ionization at 25 °C (pK_1=11.69 and pK_2≈20). Consequently,

the predominant peroxide species for pH < 12 is H_2O_2 whereas for higher pH (pH>12) is HO_2^-. Supposedly, an effective Lewis acid-base couple in alkaline media can be formed as Fe^{x+}- HO_2^-). Contrary, in acid media the lack of stabilizing interaction in Fe^{x+}-H_2O_2 facilitate peroxide desorption and its release into bulk [75].

Hence, it can be concluded that ORR shows significant mechanistic difference in alkaline and acidic media which fundamentally originates from the intrinsic difference in absolute potential of the electrode in different pH values, however the double layer structure is mostly identical in both environments. In acid, strong electrostatic interaction of OH^-_{ad} with electrode blocks the direct adsorption of molecular oxygen on active sites. On the contrary, in alkaline media, OH^-_{ad} not only blocks the O_2 adsorption but promotes inner-sphere electron transfere mechanism to precede the ORR through 4ē pathway.

2. Experimental Part

2.1. Catalyst synthesis.

2.1.1. Carbon support pretreatment.

As-received commercial carbon support, typically Ketjen EC 600JC (AkzoNobel) (100 mg) was ultrasonically dispersed in 0.5 M HCl (100 ml) for 30 minutes. Thereafter, it was kept for 24 hours under continuous stirring condition to remove the residues of the metal possibly present in as-received carbon. Afterwards, carbon was washed until neutralization and dried over night in drying oven at 60 °C in air. Carbon powder (100 mg) was activated by refluxing in concentrated nitric acid (69 wt%, 10ml) at 90 °C for 5 hours. The activation step was followed by washing/neutralizing/drying (at 60 °C/overnight) steps to achieve the pretreated carbon. For syntheses of some catalysts activated carbons were used which are mentioned in relating parts. In this thesis, the commercial carbon which was used without any acid treatment is called as-received carbon and after acid treatment as activated or pretreated carbon.

2.1.2. Synthesis strategies

Two different mixing techniques were used in this thesis: a) wet impregnation (adsorption) or b) ball milling. For wet impregnation strategy, starting precursors were mixed in the solution phase while ball milling is a dry mixing strategy. In both cases, achieving a homogeneous final mixture was the goal. In wet impregnation stirring time and in ball milling, ball milling time was optimized to gain the best catalyst mixture. In wet impregnation, after keeping the precursors under stirring condition, samples were dried in vacuum rotator to achieve the powder. Thereafter, the powders from both strategies experienced the same synthetic steps. The samples were mounted in ceramic crucibles and inserted in a horizontal single zone split tube furnace (Carbolite, Germany, see Figure 6) equipped with the flow controller. In order to remove oxygen from the oven tube, the temperature protocol started with at least 2 hours continuous nitrogen purging (at room temperature). Afterwards, the sequence was continued by heating ramp of 5 °C min^{-1} to target temperature in nitrogen (AirLiquide, Germany, 99.999 %) and kept for exact duration (mentioned in each chapter) and finally cooled down. All the powders were taken out of the oven when temperature was <50 °C. The details of pyrolysis steps were mentioned later for each chapter.

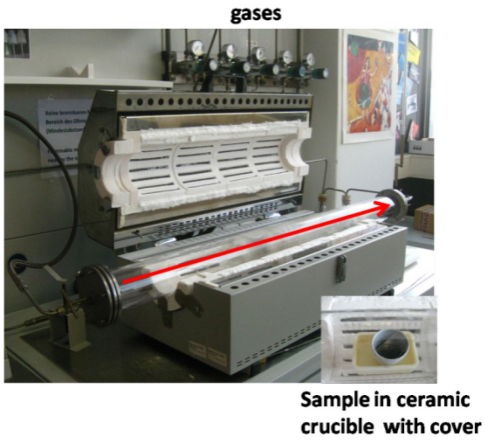

Figure 6. Tube furnace setup and sample in ceramic crucible with cover.

For metalfree samples, the synthesis procedure was ended with one-step pyrolysis. However, for metal-containing samples, additional acid leaching/pyrolysis steps were further used. In a typical acid leaching step, well-grinded powder was dispersed in 2 M H_2SO_4 (Sigma Aldrich) and refluxed in air at 90 °C for 8 hours to remove all un-reacted metal species. After the acid leaching, the samples were washed; neutralized and dried. The acid leached powders went through a second heat-treatment at 900 °C for 3 hours (2^{nd} pyrolysis). For some of the catalysts with best ORR electrochemical performances, an extra acid leaching and further heat-treatment (pyrolysis) steps were carried out (2^{nd} acid leaching/3^{rd} pyrolysis). The schematic of the representative synthesis strategy is depicted in Figure 7.

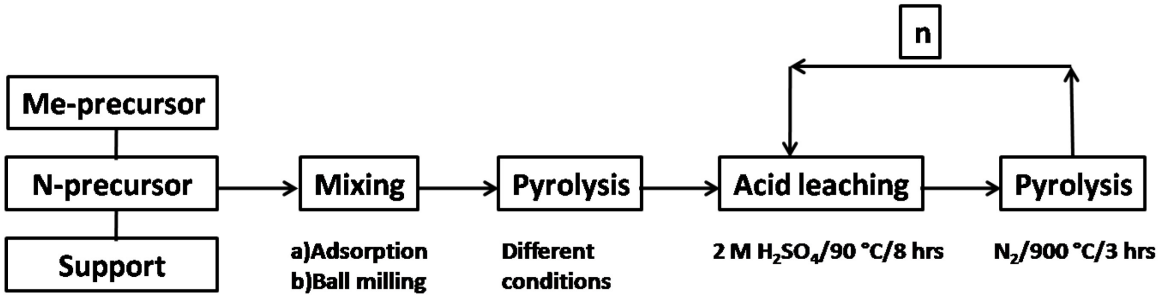

Figure 7. Schematic of the synthesis procedure for non noble metal catalysts (NNMCs).

In chapters 3, 5 and 6 the nominal weight percent of the metal was shown as X in sample formula (Me_X, X=metal weight percent) and in chapter 4 the nominal metal

precursor weight was depicted as X The details of synthesis in each chapter are summarized as the following:

Chapter 3-*Polaniline-based catalysts (PANI):* synthesis of PANI-based catalysts, metalfree PANI/Ketjen and metal containing samples ($Me_{Xwt\%}$/PANI/Ketjen, X=metal weight percent, PANI=polyaniline, Ketjen EC 600J) was performed via wet impregnation of nitrogen/(metal) precursors onto the acid-treated Ketjen. For a typical $Fe_{27wt\%}$ /PANI/Ketjen catalyst, 2 ml aniline (Sigma-Aldrich) was first dissolved in 500 ml 0.5 M HCl solution. Thereafter, 3 g $FeCl_3$ (anhydrous, Sigma-Aldrich) was added into the solution and tit was kept stirred for 2 hours to be fully mixed with aniline. After the complete dissolution/mixing of metal and aniline precursors, 5 g ammonium peroxydisulfate (APS, $(NH_4)_2S_2O_8$, Sigma-Aldrich), as the oxidant, was added drop wise for *in situ* polymerization of aniline while the mixture kept at < 10 °C. The polymerization started by formation of polyaniline, detecting by the color change, first, to blue and then green. The polymer suspension was kept at low temperature as long as no color change was observed. Nitric acid-treated Ketjen (0.4 g) was mixed with Fe/PANI under constant stirring for 24 hours to achieve uniformly distributed Ketjen and PANI suspension. Carbon supported Fe/PANI was refluxed for 5 hours and then vacuum-dried using a rotator evaporator. The subsequent heat treatment for the resulting dried powder was performed at 900 °C for 1 hour in N_2. The acid leaching (2M H_2SO_4/5h) and 2nd pyrolysis (900 °C /3 hour/N_2) were performed to achieve the final catalyst.For Mn-based catalysts, $MnCl_2$ (anhydrous, Sigma-Aldrich) was used as the metal precursor. All the monometallic samples -Metal=Fe or Mn- were synthesized based on the above-mentioned procedure by changing the metal precursor type and amount for different metal loadings while aniline, APS and support contents kept unchanged. For bimetallic catalysts with total metal (Me) 27wt%, three different molar ratios of Mn:Fe were synthesized: Mn:Fe=1:3, Mn:Fe=1:1 and Mn:Fe=3:1. For some best performing mono- and bimettalic catalysts, the 2nd acid leaching (2M H_2SO_4/90 °C/5h) and 3rd pyrolysis (900 °C/3h/N_2) were performed. A typical metalfree PANI/Ketjen was synthesized by *in situ* polymerization of aniline as mentioned above without addition of metal precursor. Thereafter, PANI was impregnated on Ketjen (stirring, refluxing, drying). Finally, PANI/Ketjen dried powder went through 4 hour pyrolysis (900 °C/4h/N_2).

In order to investigate the influence of pyrolysis temperature and nature of support on ORR activity, $Fe_{27wt\%}$/PANI/Ketjen composition was selected and was pyrolysed at three different temperatures, 500, 700 and 900 °C (1st pyrolysis). All these samples went through the acid leaching and 2nd pyrolysis (900 °C/3h) to attain the final catalysts. Additionally, to investigate the influence of the support type, commercial graphene oxide (NanoInnova Technologies) and multiwalled carbon nanotube (Bayer) without any acid treatment (as-received) were impregnated with 27 wt% Fe and PANI (pyrolysis temperature at 900 °C). The synthesis steps and conditions were as the same for Ketjen-supported samples.

To gain insight into the intrinsic activity of polyaniline (PANI) and the influence of metal and support on its activity, control catalysts were synthesized and characterized as the following: PANI (4 hour pyrolysed), $Fe_{27\ wt\%}$/PANI (1h 1st pyrolysis, acid leaching and 3 hour 2nd pyrolysis), PANI/Ketjen (4 hour pyrolysed).

Chapter 4- Hexamethyltetramine-based catalysts: Hexamethyltetramine (HMTA) was synthesized by the facile and fast reaction of 10 g formaldehyde (40 wt%) with excess ammonia (200 ml, 30 wt%) in solution. As-synthesized HMTA was supported on Ketjen EC 600J by wet impregnation and by subsequent heat treatment was used for N-doping of carbon support. Two series of catalysts were synthesized, metalfree (HMTA-C) and metal containing (HMTA-Fe-C) samples. In order to achieve a homogeneous distribution of the nitrogen and metal precursors, a pre-mixing step was applied. For a typical synthesis , 2 g of HMTA was first dissolved in water, then 200 mg carbon support (as-received) was sonicated in HMTA solution for 30 minutes. For the metal containing sample, metal precursor, 40 mg iron acetate (FeAc, Aigma-Aldrich), was dissolved simultaneously with HMTA (2 g) in water and sonicated with carbon support (200 mg). After 6 hours continuous mixing, the well-dispersed suspension was heated up to 60 °C on the heating plate to evaporate water. The resulting mixture was further processed by ball milling (BM) step for 100, 300 or 500 minutes. In this case, the known number of stainless steel balls (10 mm) (10 balls for 200 mg Ketjen) was added to the precursors inside the sample holder made from stainless steel (see Figure 8). Mixing was performed by planetary ball miller (Spex Mixer-Miller 8000M) (see Figure 8).

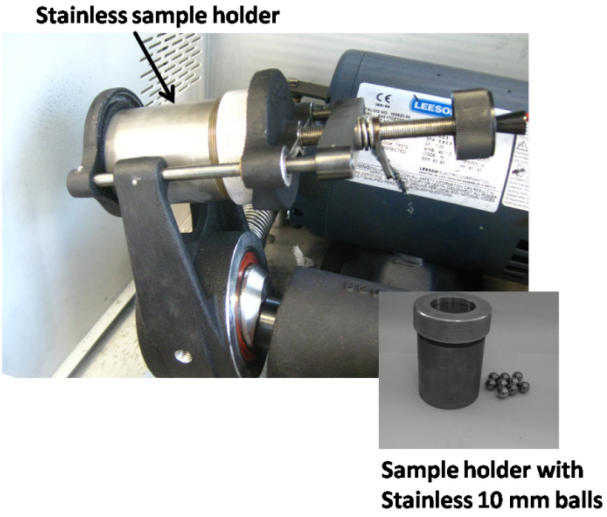

Figure 8. Ball miller setup and sample holder with stainless balls.

Thereafter, the metalfree sample was pyrolysed for 2 hours at 900 °C in N_2 atmosphere. For metal containing sample, 1st pyrolysis (900 °C/1h/N_2), acid leaching (2M H_2SO_4/5h/90 °C) and finally 2nd pyrolysis (900 °C/1h/N_2) were performed to achieve the final catalyst. The catalysts were named in different synthetic steps as the following: $HMTA_x$-Fe_y-C-z, where x refers to the nitrogen precursor (HMTA) content (g), y refers to the metal precursor (iron acetate, FeAc) content (mg) and z shows the synthesis step: z=1 (mixing before ball milling), z=2 (mixing after ball milling (BM), before pyrolysis), z=3 (ball milled sample and 1st pyrolysed) and z=4 (acid leached sample and 2nd pyrolysed).

In order to optimize the precursor content and ratios, various catalysts were synthesized with different nominal metal and nitrogen precursor ratios. The precursor contents used in the syntheses of different catalysts with 200 mg Ketjen are summarized in Table1.

Table 2. Summary of precursor composition used in the syntheses of different catalysts with 200 mg Ketjen (as-received).

Catalyst	Precursors employed for synthesis with 200 mg Ketjen (as-received)	
	HMTA (g)	FeAc (mg)
$HMTA_2$ –Fe_{400}-C	2	400
$HMTA_2$ –Fe_{40}-C	2	40
$HMTA_2$ –Fe_{20}-C	2	20
$HMTA_2$ –Fe_2-C	2	2
$HMTA_4$ –Fe_{40}-C	4	40
$HMTA_6$ –Fe_{40}-C	6	40
$HMTA_1$-C	1	-
$HMTA_2$-C	2	-
$HMTA_4$-C	4	-
$HMTA_6$-C	6	-

Chapter 5- ***Ionic liquid-based catalysts***. Cyano functional-containing ionic liquids including *N,N*-ethyl-methyl-imidazolium-dicyanamide (EMIM-dca), *N,N*-ethyl-methyl-imidazolium-tetracyanoborate (EMIM-tcb) and phosphorus-containing additive tetraethyl-phosphonium-bromide (TEPBr) were acquired from Sigma-Aldrich, Merck and TCI, respectively. 3-methyl-thiazol-3-ium-dicyanamide (THIA-dca) was synthesized by letting thiazole and iodomethane react towards THIA-iodide and subsequent anion metathesis towards THIA-dca. The detailed synthesis protocol was adopted from a published work focused on the synthesis of IL synthetic strategies [151]. In this study, commercially available Ketjen EC 600J was functionalized using the aforementioned ionic precursor systems. For a typical synthesis of the discussed materials, 400 mg of Ketjen (as-received) was dispersed in 100 mL of deionized water. The precursor (N: 550 mg EMIM-dca / S/N: 550 mg THIA-dca / P/N: 550 mg EMIM-dca + 385 mg TEPBr / B/N: 550 mg EMIM-tcb) was added to the dispersion, followed by the addition of ferric chloride ($FeCl_3$, anhydrous, Sigma-Aldrich) in the case of metal catalyzed synthesis (e.g. 311 mg for X/N_Fe_{27} materials). In this case X, is heteroatom

and 27 shows the weight percent of metal. The dispersions were stirred overnight for homogenization. Thereafter, the dispersion volumes were reduced by half in the rotary evaporator and were transferred to ceramic crucibles that were placed in the tube furnace equipped with a gas inlet. The samples were thermally treated under a continuous flow of argon gas (~4 L min^{-1}), first being heated during 2 h towards 100 °C. After holding the temperature at 100 °C, the sample was further heated during 2.5 h towards 900°C. After 1 h pyrolysis at 900 °C, the samples were allowed to cool down naturally. The metal free samples were used directly without further treatment while the samples synthesized with ferric chloride went through an acid leaching step and 2^{nd} pyrolysis. They were refluxed at 110 °C overnight; after cooling down to room temperature the carbonaceous part was isolated by centrifugation and subsequently undergoing washing with deionized water until pH 7 was reached. The 2^{nd} thermal treatment under argon gas was performed with exactly the same temperature profile before using the samples for further analysis and application. For some samples one further step of acid-leaching and heat treatment were applied to investigate their effects on the catalyst activity

Applying this method, numerous carbon systems functionalized with different heteroatom doping profiles were synthesized: EMIM-dca was used for merely nitrogen-doped systems. THIA-dca was applied for obtaining nitrogen- and sulfur-co-doped materials. Nitrogen- and boron-co-doping was achieved using EMIM-tcb. For co-doping with nitrogen and phosphorus no single precursor was accessible, instead a mixture of EMIM-dca and TEPBr was used. The molecular structures of the precursors depicted in chapter 5.

Chapter 6. ***Polyformamidine-based catalysts.*** The details of this synthesis is reported in a previously published work [152].

2.1.3. Electrode Preparation and Rotating Disk Electrode (RDE) Setup

Ink formulation. The ink formulations of the NNMCs were based on the optimized loadings of the catalysts. Depending on the catalyst composition/surface properties, the optimized volumes of deionized ultrapure water (18 MOhm, Sartorius, Germany), 2-propanol (Sigma-Aldrich) and 5 wt% solution of Nafion® in alcohol (Sigma-Aldrich) were added to the powder in a 5-ml glass vial. The valus used in different chapters of

this work to achieve the optimized catalyst film on the electrode surface are summarized in Table 3.

Table 3. Catalysts ink formulation applied in preparation of optimized thin film for various catalysts.

Chapter	$M_{Catalyst}$ (mg)	V_{Water} (ml)	$V_{Isopropanol}$ (ml)	V_{Nafion} (µl)
3	15.7	0.850	0.100	50
4-metalfree	15.7	0.650	0.300	50
4-metal containing	15.7	0.750	0.200	50
5	15.7	0.850	0.100	50
6	15.7	0.800	0.180	20
Pt/C 20wt%	5	3.98	1.00	20

The ink preparation includes the following steps: a) an exact amount of well-grinned powder was weighted by a precise balance in a glass vial, b) The ink mixture was horn sonicated for 15 minutes using a Branson sonifier-150 with the output 8 to result in a homogenized catalyst suspension, c) a homogeneous ink was achieved after the sonication, d) a 10-µL aliquot of catalyst suspension was pipetted onto the freshly polished glassy carbon (GC) electrode, e) After applying the drop, GC was kept at 60°C in a drying oven for 10 minutes to obtain a homogeneous and flat thin catalytic film on the electrode surface.

Formation of thin catalyst film on electrode. The glassy carbon (GC) rotating disk electrode (PINE Instruments) with 5 mm in diameter was polished using the polishing machine (Buehler, see Figure 9) in two consequent steps: first, on Nylon pads (NYLON PSA 2-7/8) using Buehler Alpha Micropolish Alumina (1 µm) and washed with deionized water, Second, on Microcloth pads (PSA 2-7/8) using Buehler Gamma Micropolish Alumina (0.05 µm) and washed with deionized water. Each step includes one minute polishing.

Figure 9. Polishing machine used in preparation of the electrode.

In order to remove the polishing paste particles from the electrode surface, 5 minutes sonication of electrode in ultrasonic bath was performed, first in a mixture of aceton:deionized water 1:1 and afterwards in deionized water.

Rotating disk electrode (RDE) setup. Electrochemical measurements of the synthesized catalysts were carried out in a standard three compartment custom-made electrochemical glass cell connected to the PINE Instrument Company electrochemical analysis system (USA) (see Figure 10(a)) working with a Biologic (VSP-5, France) biopotentiostat. Working electrode (WE) was glassy carbon disk (5 mm Ø, surface area 0.19635 cm^2) (PINE Instrument, USA) while, commercial reversible hydrogen electrode (RHE, Gaskatel) and platinum gauze (5X5 cm, Alfa Aesar) used as reference (RE) and counter (CE) electrodes, respectively (see Figure 10 (b-c)). Freshly-made 0.1 M of $HClO_4$ (pH 1) prepared by diluting of 70 % redistilled $HClO_4$ (Sigma-Aldrich) and 0.1 M of KOH (Sigma-Aldrich) (pH 13) were used as acid and alkaline electrolytes, correspondingly. The electrolytes were saturated with highly pure nitrogen (99.999 %) and oxygen gases (99.998 %) prior to the measurements for 20 minutes. During purging the electrolyte with gases, the working electrode (WE) was kept out of the electrolyte and no potential was applied into the WE. Then, working electrode was immersed into the electrolyte under controlled potential. All the RDE measurements were operated at room temperature and atmospheric pressure under blanketing of the electrolytes with proper gases (Figure 10(b).

Figure 10. Rotating disk electrode (RDE) setup, a) overall view of RDE, b and c) details of the electrochemical cell and electrodes, 1) RDE set-up, 2) working electrode (WE), 3) counter electrode (CE), 4) reference electrode (RE), 5) gas connections, d-e) glassy rotating disk electrode (RDE).

2.1.4. Activity for Oxygen Reduction Reaction (ORR) using Linear Sweep Voltammetry (LSV)

Sequential techniques for electrochemical characterization. A typical ORR measurement for non noble metal catalyst was started in N_2-saturated electrolyte. This measurement includes the sequence of the following techniques: 1) chronoamperometry (CA), 2) cyclic voltammetry (CV) and 3) electroimpedance spectroscopy (EIS). For all the measurements, electrode was inserted into electrolyte when the potential was kept under 1 V vs. RHE by chronoamperometry technique. After reaching a constant current, the technique was switched to cyclic voltammetry (CV). First, twenty continuous cyclic

voltammetries were recorded from 1 to 0 V vs. RHE with the scan rate of 100 mV s^{-1} at the stationary electrode for the cleaning of the catalyst surface. In order to evaluate the electrolyte resistance and perform the iR correction, electroimpedance spectroscopy (EIS) was performed at the stationary electrode. Then, two CVs were recorded with the scan rate of 10 mV s^{-1} from 0 to 1 V vs. RHE at 1500 rpm (round per minute) to evaluate the background capacitive current (I_{cap}) on the working electrode. Afterwards, the solution was saturated with oxygen, after the identical CA step as was applied for N_2-saturated electrolyte, linear sweep voltammetry (LSV) was measured with the scan rate of 10 mV s^{-1} at 1500 rpm with cathodic scan.

Corrections for capacitive current. To extract the faradic current (I_f) originating from the ORR, the recorded current during downward scan in O_2-saturated electrolyte was corrected by subtracting the I_{cap} recorded in N_2-saturated electrolyte, $I_f = I - I_{cap}$, defined as negative for a reduction reaction.

iR corrections with EIS. All electrode potentials were corrected for ohmic losses using electrochemical impedance spectroscopy (EIS) and are referred to RHE for all the measurements in this thesis. To determine the ohmic resistance, impedance spectra were recorded at every potential/current step between 10 kHz and 1 Hz with modulation amplitude of 10 mV.

In this work, the electrochemical parameters are defined as following:

- **Onset potential (E_{onset}):** The potential at which faradic current (I_f) reached -1 mA cm^{-2} in the cathodic scan.
- **Diffusion-limiting current (I_d):** the faradic current at 0.4 V vs. RHE.
- **Half wave potential ($E_{1/2}$):** the potential at which current reached half of the diffusion current (I_d at 0.4 V vs. RHE).

- **Kinetic current (I_k):** Kinetic current (I_k) is a theoretical current that would be measured if O_2 diffusion were infinitely fast. I_k for a given loading is only controlled by the ORR kinetics of the catalyst. The relationship between I_k and I_f is the Koutecky-

Levich equation: $I_k = I_f I_{lim} / I_f - I_{lim}$. I_k is defined < 0 for reduction scan and >0 for oxidation scan.

- **Mass activity (I_m):** mass activity of NNMCs is defined by Equation 3:

$$I_{mass\ (NNMC)} = -\frac{I_k}{m_{catalyst}}\ (mA\ mg^{-1}) \qquad (eq\ 3)$$

Where I_{mass} is the current density ($I_{mass} > 0$) and $m_{catalyst}$ is the NNMC loading on glassy carbon (mg cm^{-2}). The potential at which I_m is reported is 0.8 V vs. RHE.

- **Current density J (mA cm^{-2}):** Electrocatalytic current was normalized on geometrical electrode surface area (A=0.19835 cm^2) which was defined as the current density for different catalysts.

- **Tafel plot.** Kinetically controlled current (I_k) measured at a rotation speed of 1500 rpm in the potential range of 1-0.7 V vs. RHE were used to derive the Tafel slopes (mV $decade^{-1}$) of different samples. Regarding to this, working electrode potential (V vs. RHE) was plotted vs. log I_k and the corresponding Tafel slope was used to compare the catalytic activities of samples.

2.1.5. Electrochemical Long-term Cycling Stability Experiments

The ″lifetime″ stability test with 9000 cycles in the potential window of 0.5 to 1.2 V versus RHE in N_2-saturated electrolyte at the scan rate of 50 mV s^{-1} on stationary electrode was used to evaluate the stability of non noble metal catalysts in the alkaline and acid media. After performing the stability tests, the electrolytes were saturated with O_2. The corresponding mass activities after 4500 and 9000 cycles were compared with the initial activity of the catalysts (after 20 cycles). The observed losses in the mass activities of the catalysts after the stability tests were used as the criteria for the stability comparison.

2.1.6. Methanol Tolerance-Methanol Oxidation Reaction (MOR)

To test the methanol tolerance of the synthesized catalysts, a solution of 10 W/W% of methanol was injected into the O_2-saturated electrolyte (KOH) after 150 second starting

the record of linear sweep voltammetry (scan rate of 10 mV s^{-1}, 1500 rpm, room temperature). Current density (J) chronoamperometric response at 0.8 V vs. RHE obtained for the catalysts and compared with the voltammograms in the absence of methanol.

2.1.7. Reference Catalysts

All the activity and stability results in this thesis were compared with commercial platinum nanoparticles (20 wt%) on Vulcan XC-72 (in this thesis labeled as Pt/C) from E-TEK with the loading of 10 μg_{Pt} cm^{-2}.

The identical procedure as described in section 2.1.3 was used for the reference catalyst to prepare the ink, electrode and catalyst film. The optimized ink formulation for Pt/C is summarized in Table 3.

2.2. TEM/SEM Characterization

Transmission Electron Microscopy (TEM) combined with energy dispersion X-ray spectroscopy (EDX) were used to investigate the structure/surface morphology and composition of non-noble metal catalysts. Transmission electron microscope FEI TECNAI G^2 20 S-TWIN which equipped with a GATAN MS794 P CCD-detector was used and operating at an accelerating voltage of 200 kV. For TEM sample preparation a small amount of well-grinded powder was dispersed in 2-propanol by ultra sonication. An aliquot was pipette on a Cu-grid with holey carbon films (PLANO, Germany) and dried for 5 minutes in oven at 60 °C.

2.3. BET Measurements

The N_2-physisorption measurements were performed on an Autosorb-1-C from Quantachrome Company. A BET glass tube was filled with a known amount of catalyst powder to provide a minimum surface area of 10 m^2 for an accurate measurement. All the samples were first degassed by heating the powder for 24 hours at 60°C in vacuum. Before and during the BET measurements, the sample was cooled by the flow of liquid nitrogen and continuously loaded by nitrogen. After saturation of catalyst surface by N_2, the gas pressure was reduced which result in desorption of molecules from the surface. The BET-specific surface area calculated by Quantachrome Software and DFT model was used to determine the pore size distribution of carbon material.

2.4. ICP Measurements

Metal contents of different catalysts were determined by optical emission spectroscopy using inductive coupled plasma as ionization source (ICP-OES) performed by Varian 715-ES. In this case, the initial (nominal, after synthesis) and the final (after acid leaching steps) weight percent of metals (Fe, Mn) were followed by ICP. The samples had to be pre-treated by microwave heating at 180 °C to digest all moieties of the catalyst including carbon support. In a typical ICP sample preparation, ~ 5 mg of the dry sample powder was weighted in a quartz tube and dissolved in a mixture of concentrated acids including: 2 ml sulfuric (98 wt%), 2 ml nitric (69 wt%) and 6 ml chloric (37 wt.%) acids. It is necessary to remove the formed gases as the result of acid addition from the samples before heating step in microwave by fast stirring of the solution overnight under fume hood. Sample digesting step was performed by Microwave (CEM SP-D Discover). This step includes heating up the solution to 180 °C with a constant ramp of 10 °C min^{-1}. Temperature was kept constant for 20 minutes, while the gas pressure (N_2) stabilized to the maximum 18 bar with maximum output of 200 watt. This heating step was followed by cooling with the help of N_2 flow. After this digesting step, mostly, the reaction solutions were transparent; however in rare cases small residues of carbon was visible in the solution. In order to avoid any contamination during ICP-OES measurements, the solutions were paper-filtered to remove the residual carbon particles. After filtration, they were diluted to 30 ml and ultimately analyzed with ICP-OES instrument. The exact amounts of the dissolved metal in samples were determined using normal standard calibration method. For each measurement, one blank sample (0 ppm metal) and three standard solutions with known concentrations were measured.

2.5. XRD Characterization

Diffraction reflexes for all the catalysts were recorded by a D8 Advanced X-ray diffractometer from Brueker AXS equipped with a position sensitive LynxEye detector (PSD) with a Cu Kα tube operating at a voltage of 40 kV and current of 40 mA. XRD patterns collected with following parameters: step size of 0.01° for 2θ range from 10 to 90 holding time of 7 seconds per step, variable divergence slit of 4 m, PSD Iris from 13. The XRD sample holder was a single crystal silicon (Si) disk with no background XRD reflex. The catalyst powder was mounted on the center of the disk as a flat and smooth

layer. TOPAS (Brueker AXS, version 4-2) was used to analyze all the recorded XRD patterns. The crystalline features visible in the catalyst structure were evaluated using a software package MDI Jade 8 by fitting the peaks with predefined peak positions in software.

2.6. X-ray photoelectron spectroscopy (XPS) Characterization

Samples discussed in different parts of this thesis were measured at different instruments. PANI-based were characterized by X-ray photoelectron spectroscopy at the ISISS beamline of the synchrotron facility BESSY of the Helmholtz-Zentrum Berlin. A detailed description of the setup can be found elsewhere [153]. Samples were mounted onto a sapphire sample holder and introduced into the spectrometer. Experiments were carried out at room temperature (RT) in ultra-high vacuum (UHV). Hexamethyltetramine-based (chapter 3) and Ionic liquid (IL)-based (chapter 5) catalysts were characterized at Thermo Scientific K_α XPS spectrometer with dual electron / ion beam flood source for charge neutralization. Samples were mounted onto the conductive carbon tape or soft indium foil. Excitation energy source was Mg K_α (1253.6 eV).

2.7. Temperature Programmed Desorption (TPD) and Pulse Chemisorption Measurements

TPD and Pulse chemisorption experiments were performed by Thermo scientific TPD/R/O 1110 instrument (illustrated in figure 11(a)) under a helium flow of 20 ml min^{-1} as a carrier gas. A small amount of sample (100-150 mg) was mounted in a quartz reactor (Figure 11(b) assembling in a furnace whose temperature was continuously recorded by thermocouple inserted in the catalyst reactor. The sample was mounted in two layers of quartz wool which trap the sample inside the tube. The reactor composed of two inner and outer quartz tubes to reduce the dead volume of the gas.

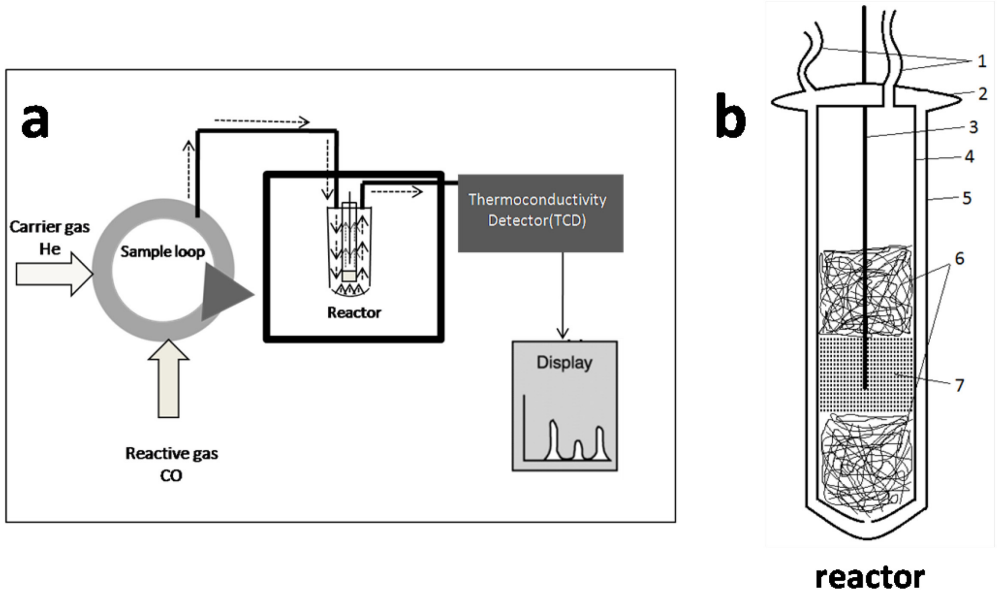

Figure 11. a) Pulse chemisorption and TPD instrument. b) Schematic of reactor: 1) gas inlet/outlet, 2) sample holder cap, 3) thermocouple, 4) internal bulb, 5) external bulb, 6) glass wool, 7) sample.

The tube was covered by a metal cap with two positions: open/close. The cap should be kept in the open position during the measurement for gas access and kept closed during the removal of the tube from the instrument. All the samples were thermally pre-treated to avoid any contamination which could originate from adsorption of undesired molecules on catalyst surface such as carbon species or water. In order to perform heat pre-treatment, in a gas flow of inert gas (helium), the temperature was increased to 600°C with a linear temperature ramp of 20 ºC min^{-1} and kept constant for 15 minutes to remove all the contaminations. Thereafter, samples were cooled down with the stream of nitrogen to 30°C. All the adsorption processes in both pulse chemisorption and TPD carried out at ~-80 C by keeping the reactor in a bath of acetone and dry ice. In pulse chemisorption, CO consumption and in TPD the desorbed gas were monitored through a thermal conductivity detector (TCD). TCD detector worked based on the changes in gas conductivity resulting from changes in gas composition. The CO molecules are dragged by the carrier gas as far as TCD which principally measures the concentration difference of the desorbed gas versus a reference flow.

For pulse chemisorption measurements, 6 continuous identical CO pulses at intervals of 15 minutes, each comprised of 338 ml CO conveyed onto the helium stream passes

over the catalyst. CO uptake (per mole) could be monitored through the TCD which was mounted in the downstream. In TPD, the CO is first loaded on the catalyst kept at low temperature. After achieving the saturation, the sample was submitted to a linear increase of temperature to 600 °C. CO desorption results in a peak record by TCD.

The inert gas flow, interval between CO pulses and the number of pulses had been optimized for the system before carrying out the measurements.

2.8. Thermo Gravimetric Analysis (TGA)

The thermal behaviors of catalyst precursors going through heat treatment were investigated by a thermal gravimetric analyzer (Perkin Elmer, STA 8000). The samples were heated at 5 °C ramp from room temperature to 800 °C (maximum affordable temperature by the instrument) in a 100 ml/min nitrogen flow and weight loss was recorded.

2.9. Elemental Analysis (EA)

In order to determine the elemental composition of all the synthesized catalysts in different synthesis steps, elemental analysis was performed by Thermo Electron, Flash EA 1112 analyser.

3. Activity and Stability of Polyaniline-based non-noble Metal Catalysts for Oxygen Reduction Reaction (ORR)

3.1. Introduction

Polyaniline (PANI)-derived non-noble metal catalysts for the electrocatalytic reduction of oxygen have been reported since a few years [17, 33]. In these materials, PANI serves as the nitrogen and in part as a carbon source. Zelenay et al. in 2011 reported a Fe/PANI/Ketjen catalyst with an activity comparable with Pt/C in acid electrolyte [17]. Besides, they showed that introduction of cobalt (Co) in synthesis of a bimetallic catalyst FeCo/PANI/Ketjen improved the catalyst stability which most likely originated from a synergistic effect of metals. However, the FeCo-bi-metallic catalyst exhibited a substantially lower catalytic ORR activity compared to the Fe catalyst. Additionally, volcano plot of the electroreduction of O_2 on different metal phthalocyanines shows that Fe, Co and Mn create the most active catalysts [18], implying that the catalysts synthesized by other metals than Fe can be promising alternative to the high reported Fe catalysts. However, it has to be mentioned that presence of Fe is usually necessary to increase the activity in bimetallic catalysts synthesized with Co and Mn. The best performing catalyst reported on MnFe showed lower activity compared to the state-of-the-art catalyst [154].

3.2. Motivation

Based on previous reports on Mn containing macrocyclic ORR catalysts and the unusually high ORR activity of PANI based materials, the electrocatalytic activity and stability of monometallic manganese (Mn) and bimetallic MnFe/PANI catalysts are investigated. For the synthesis of these materials, polyaniline (PANI) was used as the nitrogen and carbon source with metal precursors providing the metal ions believed to be required for high catalytic activity. The Me/PANI precursors were impregnated on different commercial supports. The nature of the metal and its loading, the synergistic effect of Mn and Fe and the nature of the support were correlated with the ORR electrocatalysis of the final non-precious catalyst materials in both alkaline and acid electrolytes. Additionally, temperature programmed desorption (TPD) and pulse chemisorption techniques using carbon monoxide as the probe molecule were used to investigate the nature and density of active surface sites. XPS characterizations were

performed to assess the chemical environment and oxidation states of the metal and nitrogen in mono- and bi-metallic samples. To the best of our knowledge, this is the first report on the use of Carbon monoxide for the characterization of the active surface sites.

3.3. Results and discussion

The details on the syntheses of PANI-based catalysts were provided in section 2.1.2. In this chapter, the metal containing samples are labeled as $Fe_{X\ wt\%}$/PANI/Ketjen where X referring to the nominal (initial) weight percent of the metal. In order to follow the decomposition of starting precursors during 1st pyrolysis step, in particular the influence of metal type and content on final weight loss, thermogravimetry analysis (TGA) was performed for different precursor mixtures. TGA profile of the representative catalyst, $Fe_{27wt\%}$/PANI/Ketjen, is illustrated in Figure 12. The thermolysis process can be divided into three major regions occurring within the respective ranges of temperature: At 100 °C, decomposition initiated with a relative high slope which results in 70 wt% mass of starting precursors by increasing the temperature to 300 °C. Further temperature increase to 400 °C shows a residual weight of 53 wt%. Between 400 and 700 °C, decomposition slowly yields to around 30 wt% of the initial material weight.

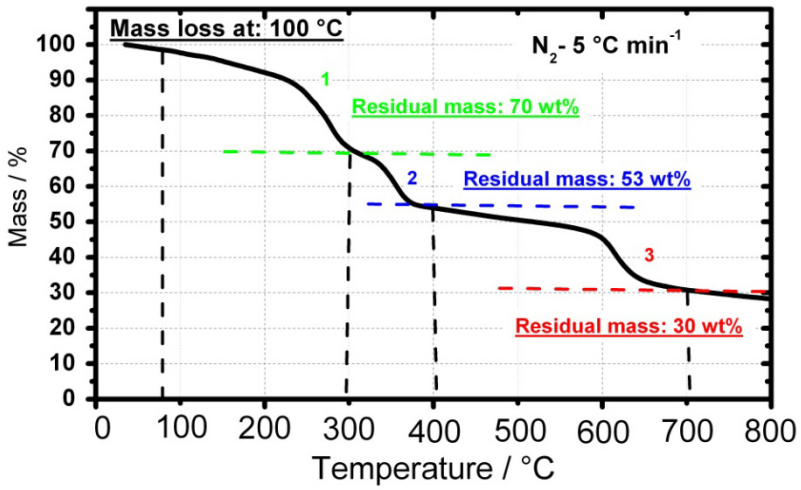

Figure 12. TGA profile of $Fe_{27wt\%}$/PANI/Ketjen in N_2 from 0 to 800 °C (5 °C min^{-1}).

TGA measurements of all monometallic (Me= Fe or Mn) and bimetallic materials (MnFe) are depicted in Figure 13(a) and Figure 13(b), respectively. There is a difference between TGA profiles of different precursor mixtures, in particular, in the

third step of decomposition, implying that metal type and content has an effect on the decomposition process. However, for all the catalysts, ~30 wt% of starting mass remained after the heat treatment up to 800 °C.

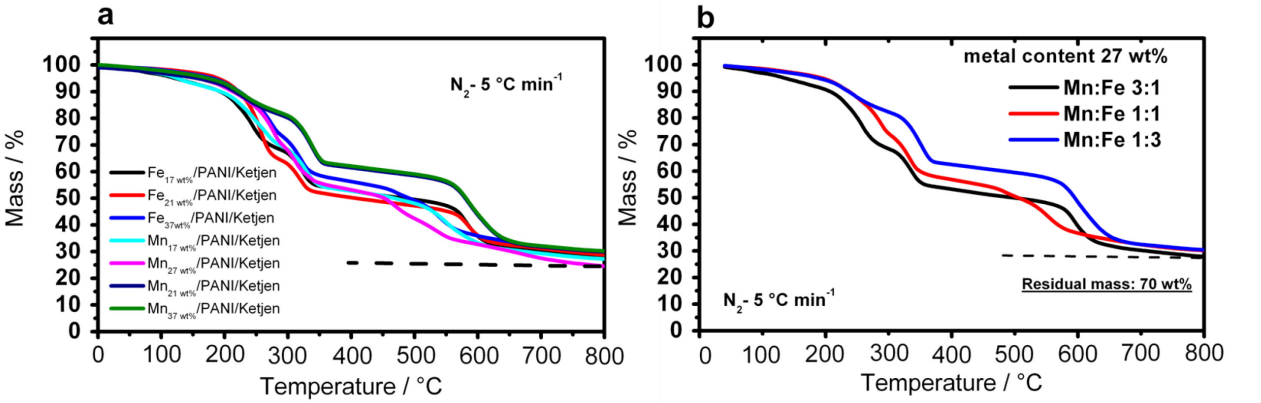

Figure 13. TGA profiles of a) monometallic Mn and Fe catalysts with different metal loadings, b) bimetallic Mn:Fe catalysts with 27 wt% metal loading with different M:Fe ratios in N_2 from 0 to 800 °C (5 °C min^{-1}).

Catalyst composition and morphology were characterized by powder X-ray diffraction (XRD) and transmission electron microscopy (TEM) techniques. XRD patterns of as-received Ketjen, after 4 hours heat treatment (at 900 °C), PANI/Ketjen and Fe/PANI are depicted in Figure 14 and 15, respectively. Apparently, heat treatment has no any significant influence on the graphitization degree of commercial Ketjen as the pyrolysed (PANI)/Ketjen shows the same peaks as the commercial Ketjen. Supposedly, the temperature of pyrolysis of 900 °C is too low for graphitization. In this case, relatively broad peaks are observed in all the samples. The most intense peak at 2θ=25° (002) and a weak peak at 43° are in agreement with the diffraction pattern of graphite-2H. Interestingly, (002) reflection of the pyrolysed PANI shows a slight shift towards lower diffraction angles. This shift represents an expansion of the distance between the graphene layers in the graphite structure. It is possible that N incorporation result in this observation (see Figure 14). Moreover, the crystal structure of PANI/Ketjen after 4h pyrolysis is different than the other samples due to the presence of an additional reflection at ~62°. This additional reflection can be explained by the formation of different d spacing in graphite structure.

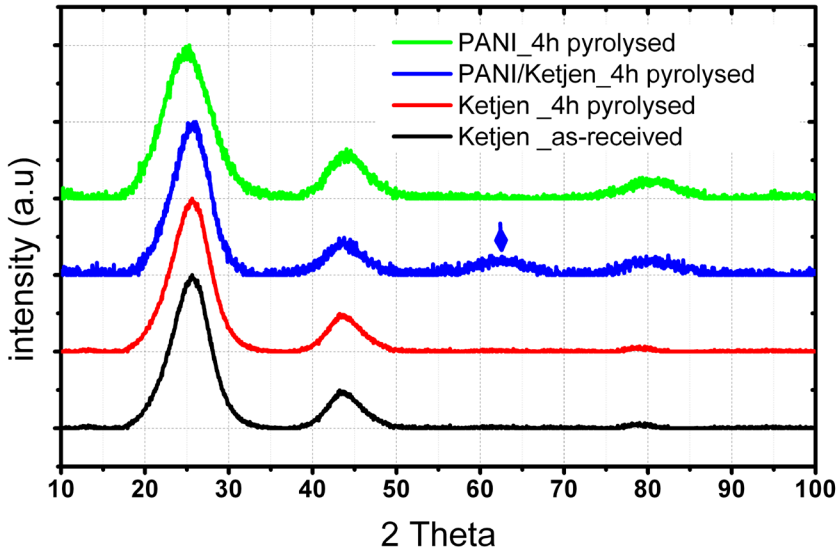

Figure 14. XRD patterns for various control catalysts: as-received commercial Ketjen (black line), Ketjen 4h-pyrolysed at 900 °C (red line), PANI/Ketjen 4h-pyrolysed at 900 °C (blue line) and unsupported PANI 4h-pyrolysed at 900 °C (green line).

The XRD patterns for the representative sample, $Fe_{27wt\%}$/PANI/Ketjen monometallic catalyst, in different synthetic steps are compared to Ketjen EC 600J (as-received) in Figure 15. Unpyrolysed $Fe_{27wt\%}$/PANI/Ketjen material (Figure 15(b) shows a well-defined crystalline structure, assignable to the excess of the oxidant, APS, before heat treatment with the most significant peaks at 2θ= 11.8 °, 17.6°, 18.2°, 22.2°, 26.6° and 30.4°. Additionally, small amount of iron salt peaks (2θ=31.2°, 36.4° and 45.1°) can be detected. However, the very broad polyaniline peaks which should be located at 2θ=20.8°, 44.4° and 61.6° cannot be observed (see Figure 15(b) [33].

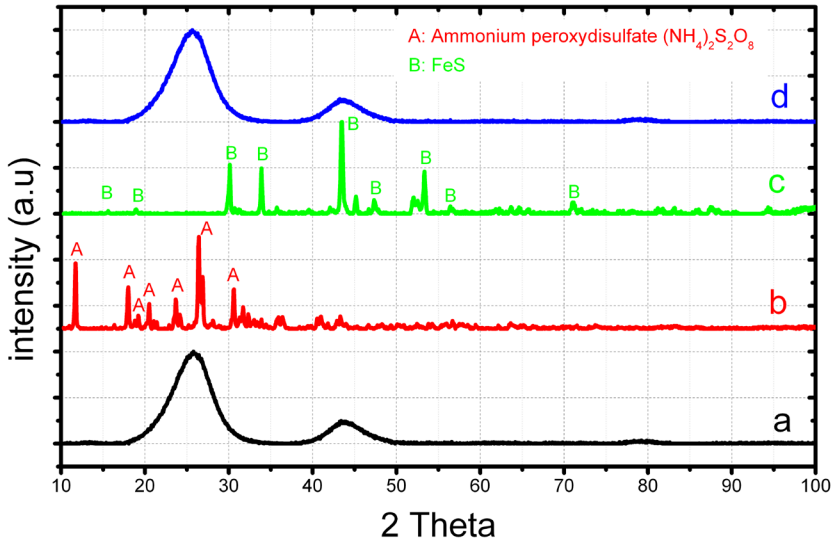

Figure 15. XRD patterns for $Fe_{27wt\%}$/PANI/Ketjen catalyst in different synthetic steps compared with Ketjen: a) Ketjen (as-received), b) catalyst precursors before pyrolysis, c) after 1st pyrolysis but before acid leaching, d) after acid leaching and 2nd pyrolysis.

In Figure 15(c), when APS is decomposed due to the first heat treatment step, the peaks can be attributed to the crystalline phase of FeS (Troilit) (2θ= 17.4°, 19.2°, 29.12°, 31.9°, 33.7°, 35.7°, 43.3°, 47.4°, 54.0°, 63.5° and 70.8°), and to a lesser degree to metallic iron (2θ=44.8° and 64.5°) which was formed at high temperature in the presence of decomposed APS and metal [155]. After the acid leaching/2nd pyrolysis step, the XRD patterns are similar to the as-received Ketjen pattern as the majority of crystalline metal moieties are removed from the material (see Figure 15(d)).

For the representative manganese sample, $Mn_{27wt\%}$/PANI/Ketjen, change in the structure and composition of the material regarding the synthetic steps was identical to the iron catalyst as depicted in Figure 16. Before heat treatment, crystalline structure of APS is clearly distinguished in XRD (see Figure 16(b). In this case, after the 1st heat treatment MnS is formed with peaks appeared at 2θ= 29.6°, 34.37°, 49.3°, 58.75°, 61.52°, 72.18°, 79.9°, 82.54° and 92.62° as depicted in Figure 16(c). After acid leaching, the representative peaks relating to MnS disappeared and the identical diffraction pattern to that of Ketjen (Figure 5(a)) was recorded.

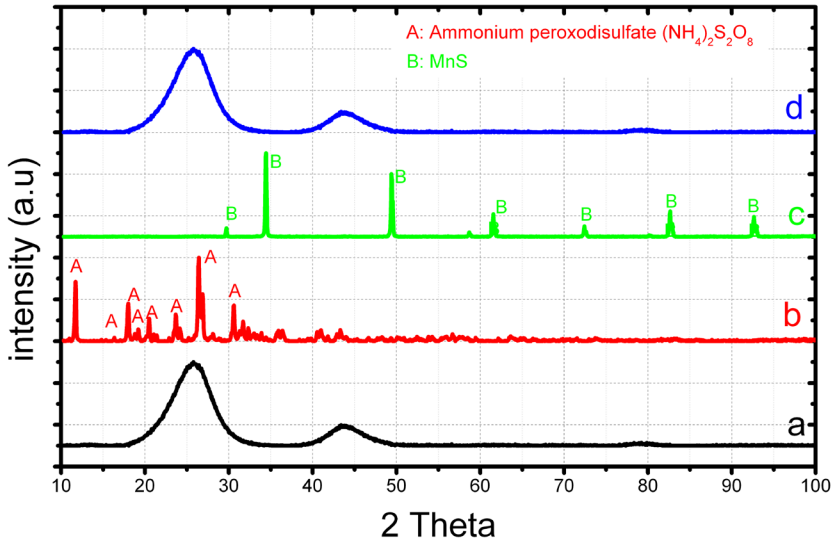

Figure 16. XRD patterns for $Mn_{27wt\%}$/PANI/Ketjen catalyst in different synthetic steps compared with Ketjen: a) Ketjen (as-received), b) catalyst precursors before pyrolysis, c) after 1st pyrolysis but before acid leaching, d) after acid leaching and 2nd pyrolysis.

In bimetallic (MnFe) catalysts, the same structure and composition as in monometallic samples is observed before heat treatment (see Figure 17(b)). After heat treatment, the XRD reflections relating to MnS are observed with slightly shifts in the peak positions. This observation means the incorporation of Fe in the MnS structure (see Figure 17(c)). In all these catalysts, obviously, Mn has more affinity to create metal sulphide than Fe, even in the samples in which iron ratio is higher. These XRD patterns suggest that Fe should be the main metal component in the final material after acid leaching while the manganese preferentially formed MnS which is dissolved during the leaching step. Most likely, Fe participates more than Mn in the catalyst backbone coordinated with nitrogen and carbon. These observations are in agreement with ICP-OES results which are summarized in Table 4. It has to be mentioned that metal ratios in the final products are different from the starting ratios. In all the final catalysts, independent of starting ratios, higher iron content than manganese content is detected (see Table 4).

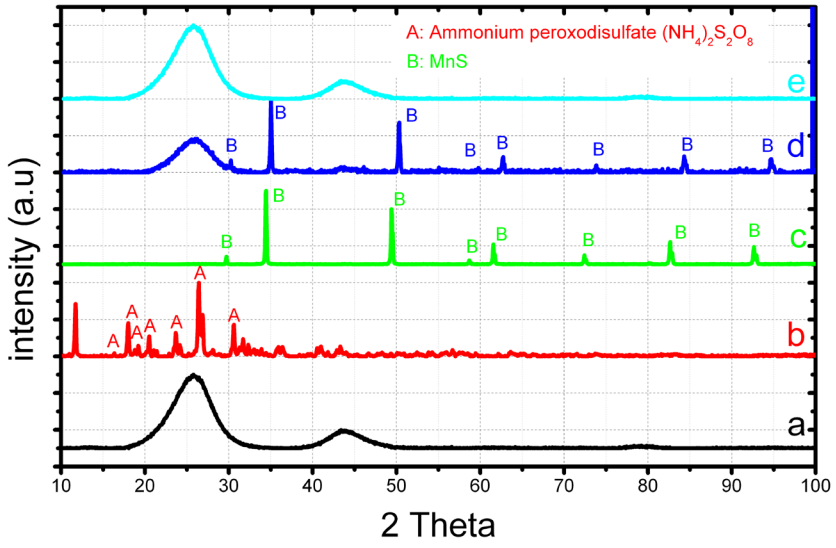

Figure 17. XRD patterns for bimetallic Mn:$Fe_{27wt\%}$1:1/PANI/Ketjen catalyst in different synthetic steps compared with Ketjen: a) Ketjen (as-received), b) catalyst precursors before pyrolysis, c) after 1st pyrolysis but before acid leaching, d) after 1st acid leaching and 2nd pyrolysis, e) after 2nd acid leaching and 3rd pyrolysis.

As it can be seen in Figure 17(d), after 1st acid leaching/2nd pyrolysis, the metal moieties (mostly MnS) removed from the catalyst and graphitization peak can be observed. However, in some catalysts, particularly with high metal loadings <21 wt%); one leaching step is not enough to remove all the metal residues, as the sulphide phase is still detectable by XRD (see Figure 17(d)). Therefore, these catalysts were subjected to a 2nd acid leaching and 3rd pyrolysis to achieve the featureless XRD patterns for any metal salt. This identical final structure as depicted in Figure 18(e) was confirmed for all the final products which were tested by RDE. Additionally, the influence of extra acid leaching/pyrolysis on the ORR activity of the catalysts was investigated.

Elemental analysis (EA) for nitrogen was applied to determine the nitrogen content of all the materials. The corresponding results for starting precursors and final catalysts are summarized in Table 4

Table 4. ICP-OES results of Fe and Mn for final catalysts after 1st acid leaching / 2nd pyrolysis, and Elemental analysis (EA) for nitrogen level in various catalysts in starting precursor and final materials. $Me_{X\ wt\%}$/PANI/Ketjen, X=metal wt%.

Catalyst	Final catalyst (Me wt%)	Starting precursor (N wt%)	Final catalyst (N wt%)
$Fe_{17\ wt\%}$/PANI/Ketjen_900 °C	3.8	10.4	8.23
$Fe_{21\ wt\%}$/PANI/Ketjen_900 °C	8.2	10.25	7.64
$Fe_{27\ wt\%}$/PANI/Ketjen_900 °C	11.7	9.54	7.2
$Fe_{27\ wt\%}$/PANI/Ketjen_700 °C	11.3	9.21	11.78
$Fe_{27\ wt\%}$/PANI/Ketjen_500 °C	8.2	9.45	15.2
$Fe_{37\ wt\%}$/PANI/Ketjen_900 °C	13.2	9.25	6.89
$Mn_{17\ wt\%}$/PANI/Ketjen_900 °C	2.5	10.56	7.49
$Mn_{21\ wt\%}$/PANI/Ketjen_900 °C	6.9	9.96	7.16
$Mn_{27\ wt\%}$/PANI/Ketjen_900 °C	10.45	9.03	6.22
$Mn_{37\ wt\%}$/PANI/Ketjen_900 °C	12.8	9.55	5.85
Mn:Fe 3:1 /PANI/Ketjen_900 °C	Mn:4.4/Fe:5.2	8.98	7.6
Mn:Fe 1:1 /PANI/Ketjen_900 °C	Mn:3/Fe:65.2	9.59	7.3
Mn:Fe 1:3 /PANI/Ketjen_900 °C	Mn:1.8/Fe:6.8	9.68	6.02

Expectedly, high-temperature heat treatment decreased the nitrogen content in the final catalysts. However, the detected nitrogen level in the final catalysts after two pyrolysis steps is high and ranges between 5.8 and 8.2 wt%. Increasing the metal content from 17 wt% to 37 wt% results in higher nitrogen loss ranges from 7.5 wt% to 5.8 wt%, respectively. There is no significant difference between the nitrogen level of the materials synthesized with iron and manganese precursors with identical metal loading. Interestingly, for bimetallic materials (all with 27 wt% metal), the nitrogen content is in the range of monometallic 27 wt% catalysts (~6 wt%). This observation shows that metal content plays a crucial role to regulate the nitrogen doping in the final catalysts; however the nature of metal is not conclusive. On the other side, pyrolysis temperature plays an important role for the final nitrogen content of the catalyst. By decreasing the temperature from 900 to 500 °C, the nitrogen doping increases from 8 to 15 wt% for $Fe_{27wt\%}$/PANI/Ketjen.

WDX-based elemental mapping of the sample Mn:$Fe_{27\ wt\%}$=1:1/PANI/Ketjen is shown in Figure 18. Obviously, nitrogen is not homogenously distributed on the surface. Nitrogen-rich regions on the catalyst surface (light green) are distributed in low nitrogen containing parts (dark blue).

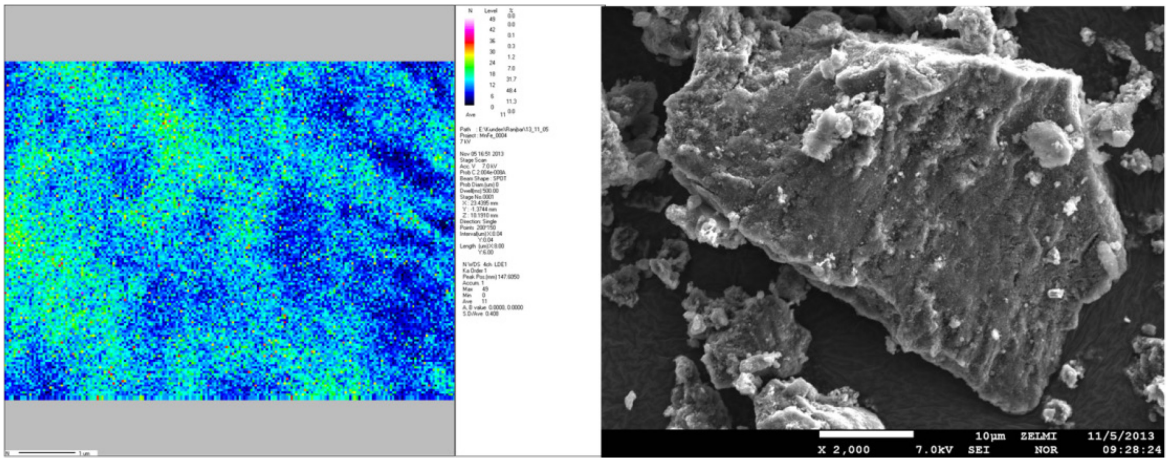

Figure 18. WDX-based elemental mapping of Mn:$Fe_{27\ wt\%}$=1:1/PANI/Ketjen at 7 kV.

In the next step, X-ray photoelectron spectroscopy (XPS) was used as a technique to explore the surface chemical environment of nitrogen (N) in $Fe_{27wt\%}$/PANI/Ketjen and Mn:Fe 1:1/PANI/Ketjen. Accordingly, the peak fitting for the N1s core level spectra (see Figure 19) reveals two major chemical environments for the nitrogen atoms within the materials while there is a pronounce similarity between the two samples. Both spectra show two significant peaks at ~398.3 eV and ~400.8 eV, referring to pyridinic and quaternary graphitic nitrogen binding sites [156-159] Thus it can be concluded that – according to XPS data – the nitrogen is almost fully incorporated into the carbon backbone of the material. Only very limited amounts of nitrogen atoms might be present as oxidized nitrogen groups, to which the broad contribution at higher binding energies might partially refer to [156, 158, 160]. Nevertheless, this the asymmetric shape of the spectrum are more likely to be described as satellite features caused by $\pi \rightarrow \pi^*$ interactions in nitrogen atoms in aromatic environment.

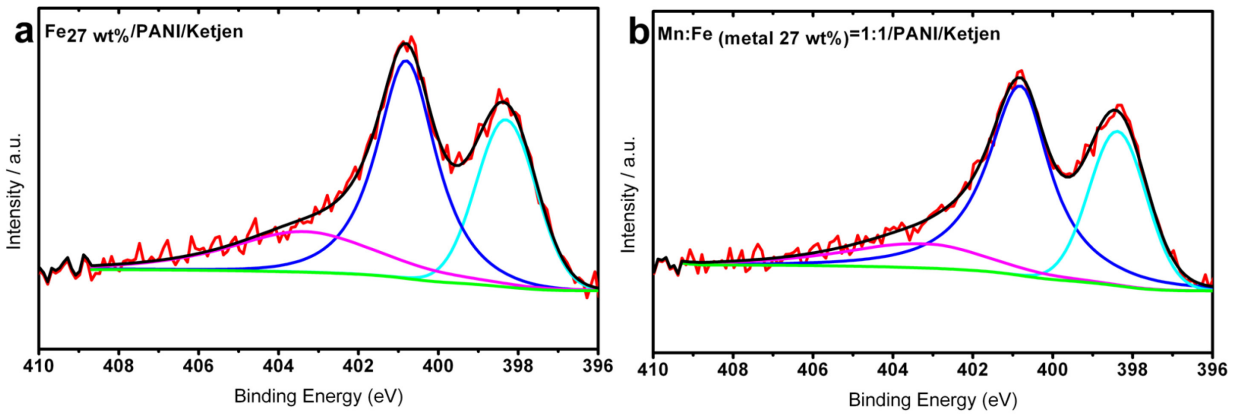

Figure 19. N1s core level of representative catalysts, a) $Fe_{27wt\%}$/PANI/Ketjen, b) Mn:$Fe_{27wt\%}$=1:1/PANI/Ketjen.

In order to gain further insight into the catalyst nanostructure, we performed TEM investigations on different control and target catalysts. PANI nanostructure as-synthesized (before pyrolysis) is depicted in Figure 20. The morphology shows a network composed of PANI fibers.

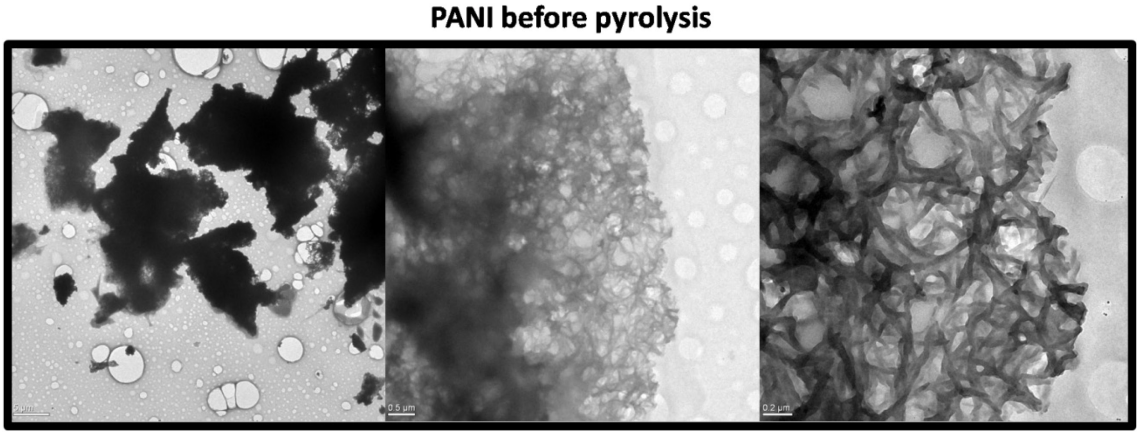

Figure 20. TEM micrographs of polyaniline (PANI) after *in situ* polymerization in the presence of oxidant (APS).

After pyrolysis, the structure of PANI fibers changes to a graphene-like morphology. TEM micrographs of PANI (4-hour pyrolysed) and $Fe_{27wt\%}$/PANI (after 1st pyrolysis, acid leaching and 2nd pyrolysis) are compared in Figure 21. Apparently, pyrolysis at 900

°C creates a well-defined graphene sheets in both samples. Noteworthy, in the presence of iron, the graphene layers grow to a higher degree as depicted in Figure 21(e).

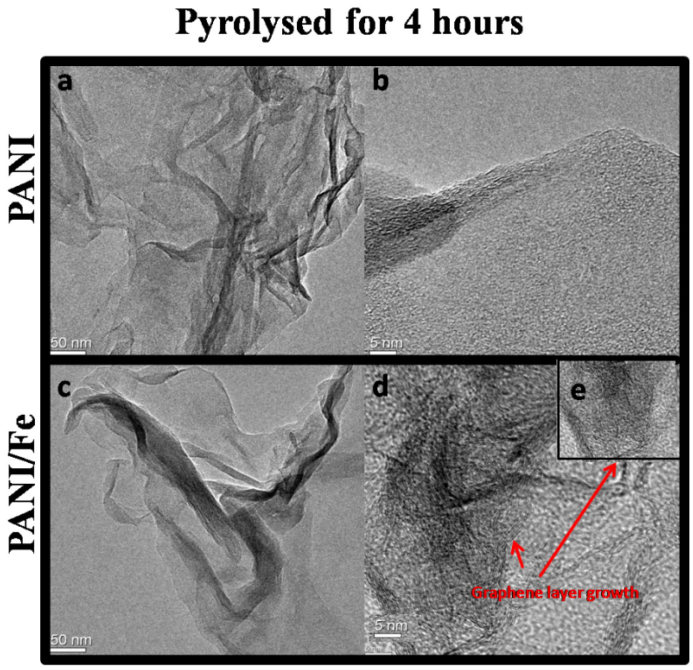

Figure 21. TEM micrographs of a) PANI, b) unsupported PANI/Fe pyrolysed at 900 °C/4h.

The morphology of the control catalyst, PANI/Ketjen is illustrated in Figure 22. In this case, the morphology shows a composite structure composed of graphene, originated from PANI heat treatment, and Ketjen particles.

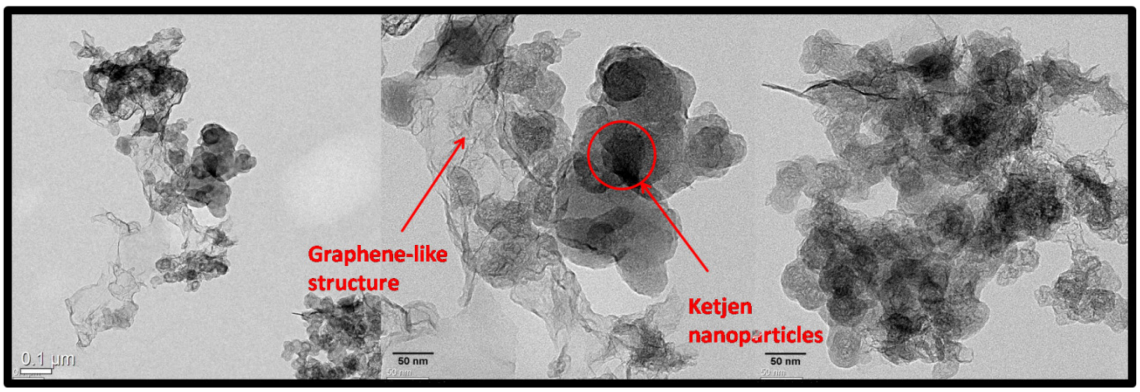

Figure 22. TEM micrographs of composite PANI/Ketjen control catalyst pyrolysed at 900 °C for 4 hours.

The TEM micrographs of the representative iron containing sample, $Fe_{27\ wt\%}$/PANI/Ketjen, in different synthetic steps are shown in Figure 23. After 1st heat treatment, a composite of PANI/Fe graphitic nanostructures (graphene-like structure) with relative light contrast mixed with Ketjen nanoparticles with dark contrast is observed (see Figure 23(a-b)). Metal aggregates encapsulated into the graphitic shell before acid leaching step can be seen in Figure 23(c). The electron diffraction pattern shown in Figure 23(d) indicates a crystalline nature of the metal moieties. After acid leaching, removal of metal particles results in an onion-like graphitic structure. The final catalyst is a composite of Ketjen nanoparticles and graphitic shells as it can be seen in Figure 23(e-f).

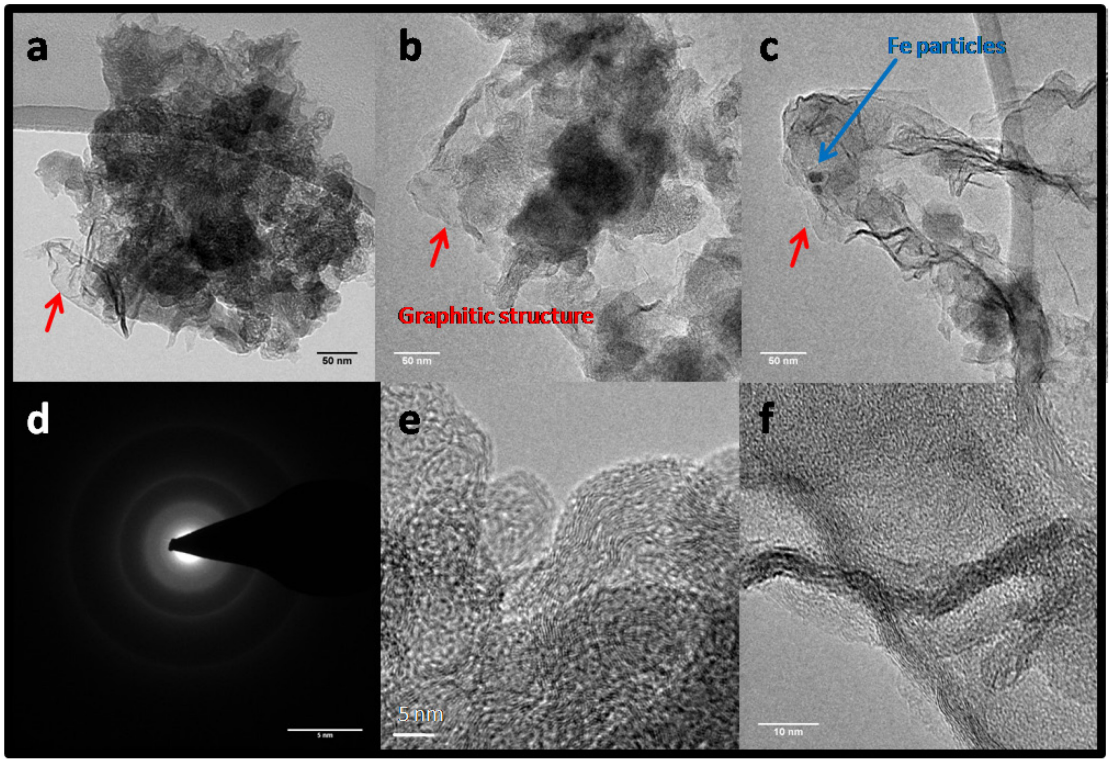

Figure 23. TEM micrographs of $Fe_{27wt\%}$/PANI/Ketjen in different synthesis steps: a-b) after 1st pyrolysis, composite structure of catalyst, c) metal-based particles hosted inside the catalyst composite of graphene and Ketjen, d) electron diffraction pattern of the metal-based particles, e-f) the catalyst structure after acid leaching and final pyrolysis steps result in the removal of metal from the catalyst.

Figure 24 illustrates the bright field (BF) and corresponding dark field (DF) TEM micrographs of $Fe_{27wt\%}$/PANI/Ketjen catalyst before the acid leaching step. Metal-based particles aggregate in carbon structure can be clearly detected in DF images. EDX confirms the presence of metal in catalyst composition.

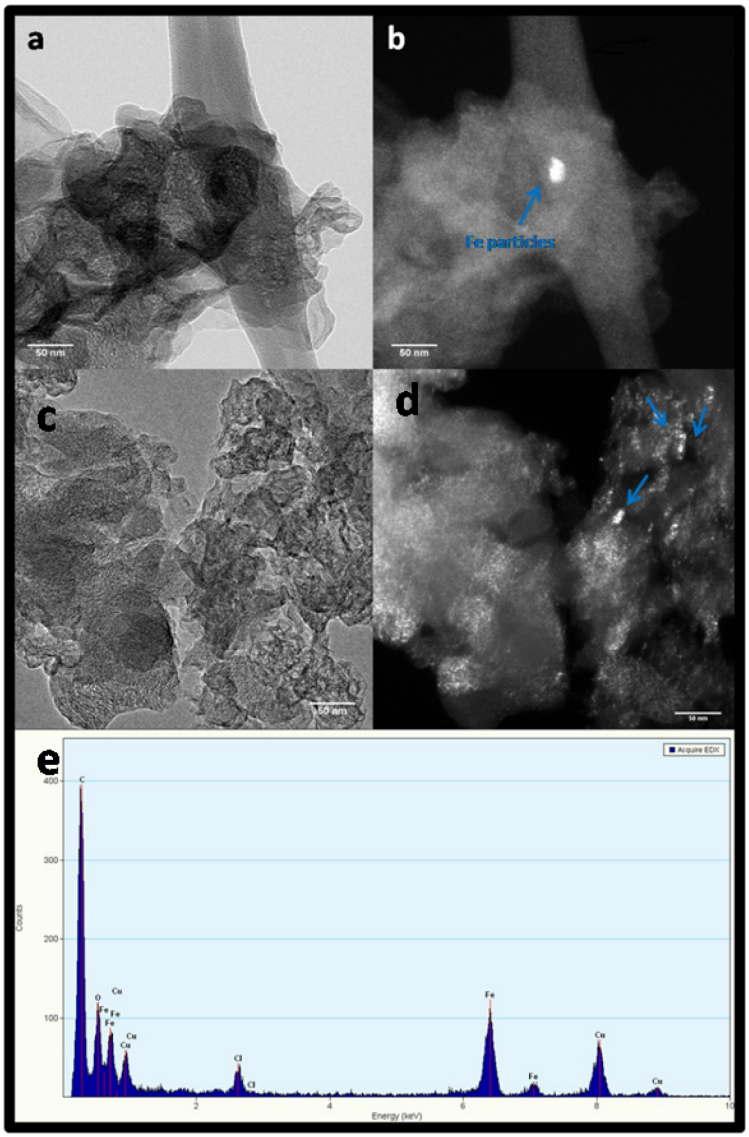

Figure 24. TEM micrographs of $Fe_{27wt\%}$/PANI/Ketjen after the first pyrolysis and before the leaching step, a) and c) bright field (BF) image; b) and d) dark field (DF) image; e) EDX results.

The same morphology is observed for the representative bimetallic sample $Mn:Fe_{(27wt\%)}$=1:1/PANI/Ketjen, as illustrated in Figure 25. After heat treatment, metal

moieties are formed inside the composite structure of graphene sheets and Ketjen particles. These metal residues remove from the catalyst after acid leaching.

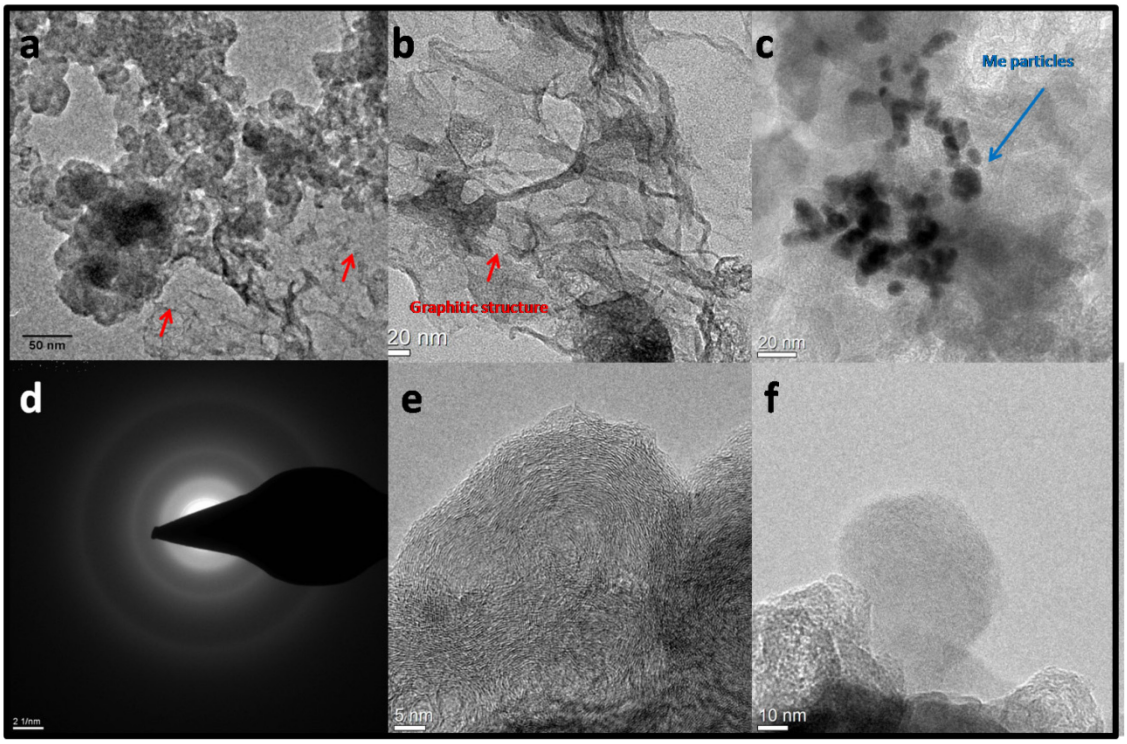

Figure 25. TEM micrographs of Mn:$Fe_{27wt\%}$=1:1/PANI/Ketjen in different synthesis steps: a-b) after 1st pyrolysis, composite structure of catalyst, c) metal-based particles hosted inside the catalyst composite of graphene and Ketjen, d) electron diffraction pattern of the metal-based particles, e-f) the catalyst structure after acid leaching and final pyrolysis steps result in the removal of metal from the catalyst.

In order to study the changes in surface area of the synthesized materials, nitrogen isotherms were recorded. In Figure 26 hysteresis of various monometallic and bimetallic samples with nominal 27 wt% metal in comparison to Ketjen as the support are depicted. The loop position shifts to higher relative pressure by changing the sample from Ketjen to metal containing samples. Corresponding values for all the synthesized materials are summed up in Table 5. Apparently, BET is decreasing from 1400 $m^2\ g^{-1}$ for Ketjen to 340 $m^2\ g^{-1}$ for $Fe_{27\ wt\%}$/PANI/Ketjen. This decreasing trend is seen for all the catalysts while BET surface area for monometallic materials ranges from 300 to 450 $m^2\ g^{-1}$. Noteworthy, the final surface areas of the bimetallic catalysts are significantly higher, typically 875 $m^2\ g^{-1}$ for $MnFe_{27wt\%}$/PANI/Ketjen.

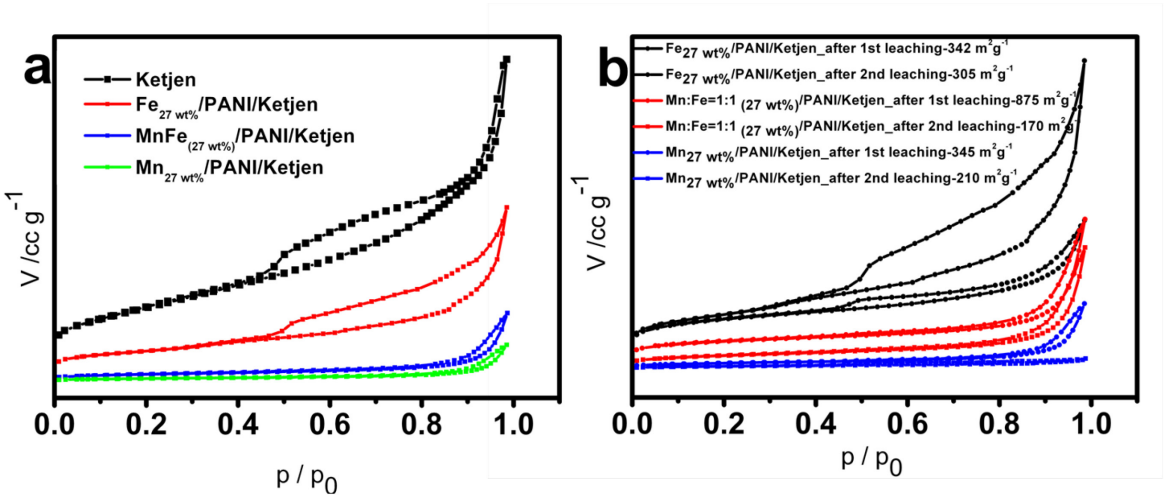

Figure 26. BET surface area of different catalysts compared with Ketjen a) after the 1st acid leaching and 2nd pyrolysis, b) after 2nd leaching and 3rd pyrolysis.

There is no clear trend which shows the effect of nominal metal content on BET surface areas. Interestingly, performing the 2nd leaching and 3rd pyrolysis steps decrease the BET surface area (see Figure 26(b)). Typically, for the monometallic sample $Fe_{27wt\%}$/PANI/Ketjen the BET surface area decreases from 342 to 305 m^2 g^{-1} after the extra leaching/pyrolysis step.

Table 5. BET surface area of various catalysts synthesized with different metal composition and contents.

Catalyst	Surface area m^2 g^{-1}
Fe 17 wt%/PANI/Ketjen	450
Fe 21 wt%/PANI/Ketjen	338
Fe 27 wt%/PANI/Ketjen	340
Fe 37 wt%/PANI/Ketjen	323
Mn 17 wt%/PANI/Ketjen	325
Mn 21 wt%/PANI/Ketjen	309
Mn 27 wt%/PANI/Ketjen	345
Mn 37 wt%/PANI/Ketjen	301
Mn:Fe 3:1 /PANI/Ketjen	840
Mn:Fe 1:1 /PANI/Ketjen	875
Mn:Fe 1:3 /PANI/Ketjen	760

Our composition and morphology characterizations show that there is a high similarity between the monometallic and bimetallic samples synthesized with iron and/or manganese. Thereafter, the electrochemical activity of these materials was evaluated to investigate the nature of metal on the catalytic performance of the materials.

Electrochemical characterization.ORR activity data for six control catalysts including, as-received Ketjen, pretreated Ketjen in nitric acid, pyrolysed Ketjen (acid pretreated/900 °C/4h), pyrolysed PANI (900 °C/4h), pyrolysed Fe/PANI (900 °C/4h) and supported PANI on Ketjen (900 °C/4h) were collected on RDE. Linear sweep voltammetries (LSVs) of the corresponding catalysts in 0.1 M KOH are shown in Figure 27. Obviously, pretreatment of Ketjen in concentrated acid and following pyrolysis leads to slight improvement of catalytic activity. In this case, the onset potential shifts from 0.16 to 0.28 for as-received Ketjen and pyrolysed Ketjen (acid pre-treated/900 °C/4h), respectively. This indicates that pretreatments create few active sites for oxygen reduction, but the final materials are not active enough, furthermore these catalysts do not show defined diffusion current regimes.

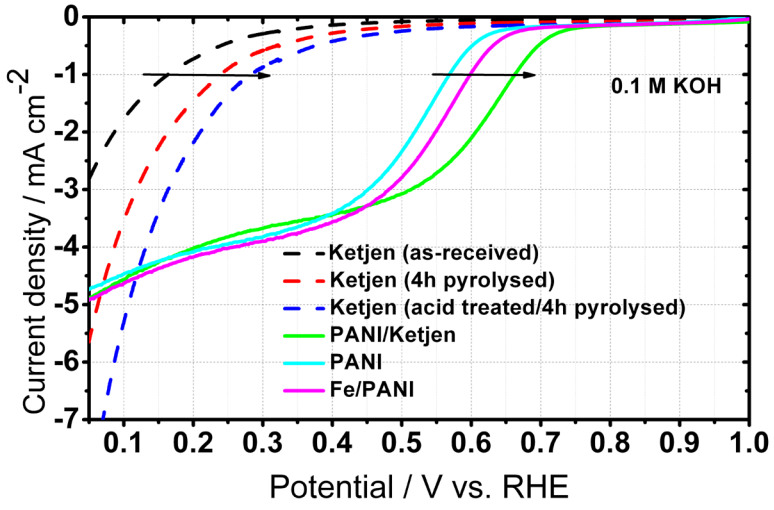

Figure 27. Electrocatalytic oxygen reduction of control catalysts. Influence of pyrolysis, addition of metal and support on catalyst onset potential. Conditions: 1500 rpm. O_2-saturated electrolyte of pH 13 at room temperature, catalyst loading 0.8 mg cm^{-2}.

Thereafter, PANI and Fe/PANI pyrolysed for 4 hours were electrochemically tested. Apparently, pyrolysed PANI leads to significant increase in ORR activity by showing

the onset potential of 0.57 V vs. RHE (see Figure 27). Interestingly, addition of iron can improve the activity, evidenced by the further positive shift to 0.6 V. Similarly, coating of PANI on Ketjen can increase the activity to 0.66 V vs. RHE. At a glance, improvement in onset potential resulting from addition of metal is less significant than supporting of PANI on Ketjen. One can conclude that among the control catalysts, PANI/Ketjen shows the best activity representing onset potential of 0.66 V vs. RHE; however the onset potential of carbonized PANI coated on Ketjen is still far from the ORR target. Nonetheless, diffusion regime of none of the catalysts is well-defined.

Since coating of PANI on Ketjen and addition of metal in Fe/PANI increase the activity of the material, further experiments were performed for Fe/PANI supported on Ketjen. In Figure 28, the ORR results are depicted for $Fe_{27\ wt\%}$/PANI/Ketjen in different synthetic steps: a) after 1st pyrolysis, b) directly after acid leaching, c) after 2nd pyrolysis and d) after 2nd acid leaching and 3rd pyrolysis.

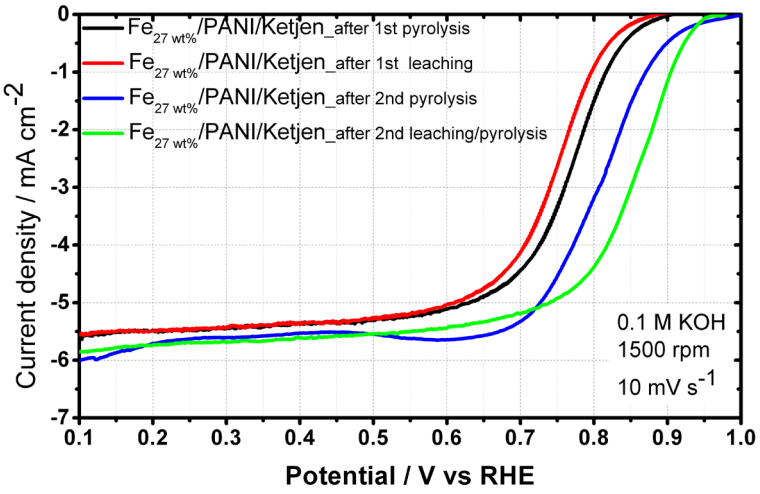

Figure 28. Electrocatalytic oxygen reduction of monometallic $Fe_{X\ wt\%}$/PANI/Ketjen (x= metal weight %) with various nominal iron loadings. Conditions: 1500 rpm. O_2-saturated electrolyte of pH 13 at room temperature, catalyst loading 0.8 mg cm^{-2}.

Simultaneous addition of metal and Ketjen in synthesis process result in further improvement of electrocatalysis. The 1st pyrolysis of Ketjen supported PANI in the presence of metal precursor (27 wt%) improves the onset potential to 0.81 V vs. RHE. After acid leaching, the activity decreases slightly (onset potential of 0.79 V), but 2nd pyrolysis improves significantly the onset potential to 0.87 V vs. RHE. Based on these

results, we can conclude that acid leaching is an essential step to create active material; however the 2nd pyrolysis is a critical step to refresh the clean catalyst surface. Supposedly, metal-based particles block the active sites of the material and acid leaching can remove them. The 2nd acid leaching and 3rd pyrolysis result in further positive shift in onset potential to 0.9 V vs. RHE.

In order to study the effect of pyrolysis temperature on ORR activity, $Fe_{27\ wt\%}$/PANI/Ketjen was pyrolysed at 500, 700 and 900 °C. The corresponding LSVs are shown in Figure 29. Obviously, increasing the temperature from 500 °C to 900 °C improves the onset potential from 0.74 to 0.87. Therefore; the following syntheses were performed at 900 °C to achieve the highest ORR activity.

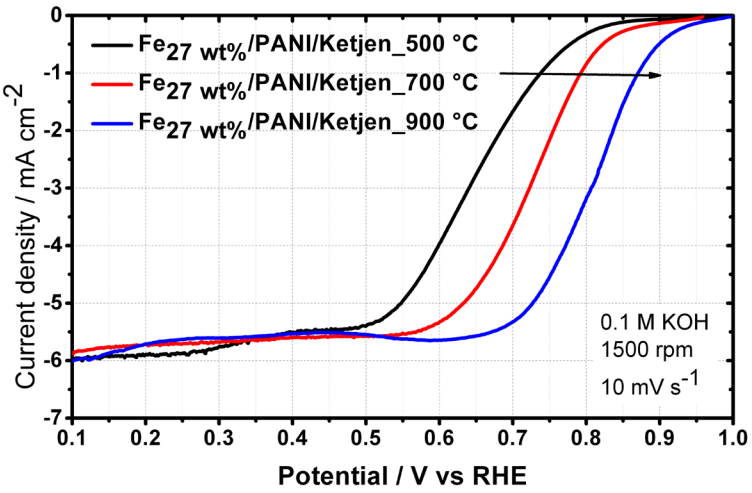

Figure 29. Electrocatalytic oxygen reduction of monometallic $Fe_{27\ wt\%}$/PANI/Ketjen (x= 27 wt%) pyrolysed at 500 °C (blue curve(700 °C (red curve) and 900 °C (black curve). Conditions: 1500 rpm. O_2-saturated electrolyte of pH 13 at room temperature, catalyst loading 0.8 mg cm^{-2}.

Doubtlessly, presence of metal is a crucial prerequisite for high activity of the final catalyst. To achieve the optimal metal content, ORR measurements performed for four various contents of metal including 17, 21, 27 and 37 wt%. LSVs recorded in O_2-saturated 0.1 M KOH of these samples is depicted in Figure 30(a) and electrochemical data are summarized in Table 6. Increasing the metal content from 17 wt% to 27 wt%, first, shifts the onset potential from 0.78 to 0.87 V; however more iron -37 wt%- negatively shifts the onset potential to 0.83 V. These results show that iron is necessary to achieve high

catalytic activity, however there is a saturation level for its content, thereafter activity is hindered (37 wt%).

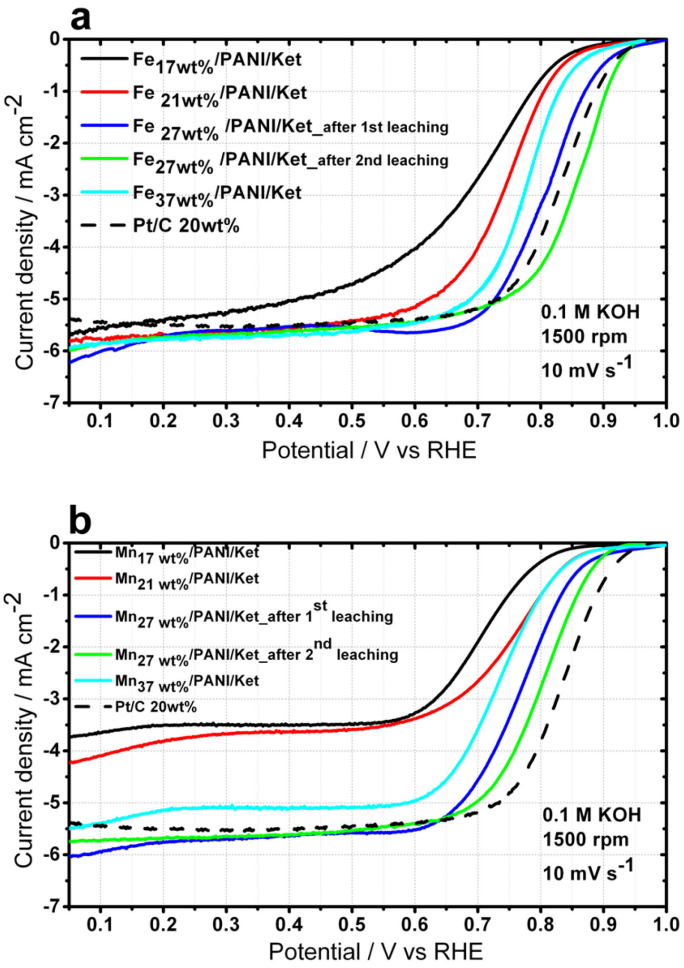

Figure 30. Influence of nominal metal loading (17-37 wt%) on ORR activity of various monometallic catalysts. Electrocatalytic oxygen reduction of monometallic a) $Mn_{27\ wt\%}$/PANI/Ketjen (x= 27 wt%) b) $Fe_{27wt\%}$/PANI/Ketjen pyrolysed at 900 °C with various nominal metal loadings compared with Pt. Conditions: 1500 rpm. O_2-saturated electrolyte of pH 13 at room temperature, catalyst loading 0.8 mg cm^{-2}.

In order to investigate the influence of metal nature on the activity of the final materials, iron was replaced by manganese in the synthesis. Four different loadings of manganese were evaluated for ORR activity (17, 21, 27 and 37 wt%). The same trend as was previously observed for the influence of iron content on activity is repeatedly detected for manganese samples (see Figure 30(b)). For the best performing manganese

catalyst (27 wt%) onset potential measured at 0.83 V. Additionally, performing the 2nd acid leaching and 3rd pyrolysis increase the activity of the best performing 27 wt% iron and manganese catalysts as it is depicted in Figure 30. Noteworthy, for monometallic iron catalyst with 27 wt% metal loading, the activity is higher than Pt/C 20 wt% reference regarding onset potential. Contrary, for $Mn_{27wt\%}$/PANI/Ketjen after the 2nd leaching the activity is still lower than Pt/C catalyst (see Figure 30 (b)).

The synergistic effect of the two metals on the final activity was investigated by synthesis of bimetallic catalysts with metal loading of 27 wt%. Three different molar ratios including Mn:Fe 3:1, Mn:Fe 1:1 and Mn:Fe 1:3 were studied towards ORR. The corresponding results for bimetallic catalysts in alkaline medium are shown in Figure 31. While the Mn:Fe=3:1 shows an activity similar to monometallic manganese sample with onset potential of 0.82 V vs. RHE, increasing the iron content in Mn:Fe 1:1 improved the activity by showing the onset potential of 0.92 V vs. RHE. Further increased in the iron ratio had not any further effect on the onset potential.

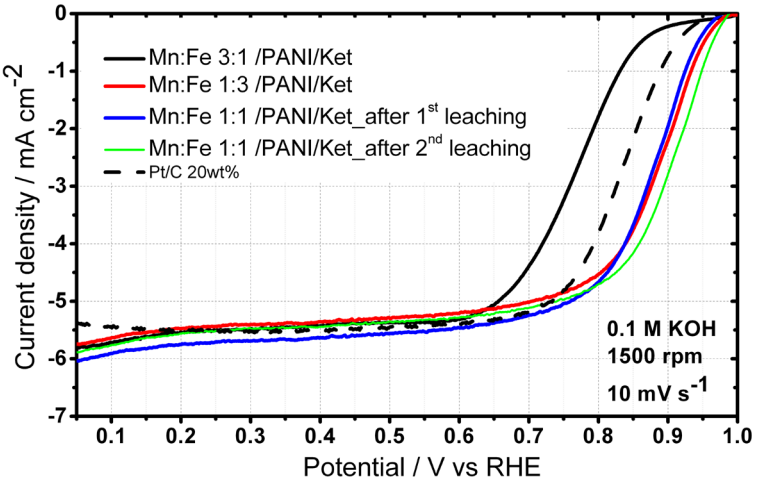

Figure 31. Influence of Mn:Fe ratio in bimetallic catalysts on ORR activity. Electrocatalytic oxygen reduction of bimetallic $MnFe_{27\ wt\%}$/PANI/Ketjen (x= 27 wt% metal) pyrolysed at 900 °C with different metal ratios compared with Pt/C 20 wt%. Conditions: 1500 rpm. O_2-saturated electrolyte of pH 13 at room temperature, non noble metal catalyst loading 0.8 mg cm^{-2}.

Noteworthy, performing the additional acid leaching and pyrolysis increase the activity, as the onset potential of 0.95 is observed for Mn:Fe=1:1 ratio. All the

bimetallic catalysts, except Mn:Fe=3:1 showed a more positive onset potential compared to the reference Pt/C catalyst in 0.1 M KOH.

The ORR activity of the best performing mono- and bimetallic catalysts in alkaline were further tested in acid electrolyte (see Figure 32). As shown above additional acid leaching and pyrolysis improved the activity, therefore all the catalysts went through 2nd acid leaching/3rd pyrolysis step before characterization in acid. As generally expected for NNMCs, the catalysts show lower activity in acid compared to Pt/C catalyst with onset potential of 0.91 V vs. RHE. The $Mn_{27wt\%}$/PANI/Ketjen catalyst represents a relatively negative onset potential of 0.82 V vs. RHE. Monometallic $Fe_{27wt\%}$/PANI/Ketjen and bimetallic Mn:$Fe_{27wt\%}$ 1:1/PANI/Ketjen catalysts show similar activity with onset potential of 0.88 and 0.87 V vs. RHE, respectively. Figure 32 depicts the ORR activity of the best performing mono- and bimetallic catalysts compared to the Pt/C reference in both alkaline and acid media.

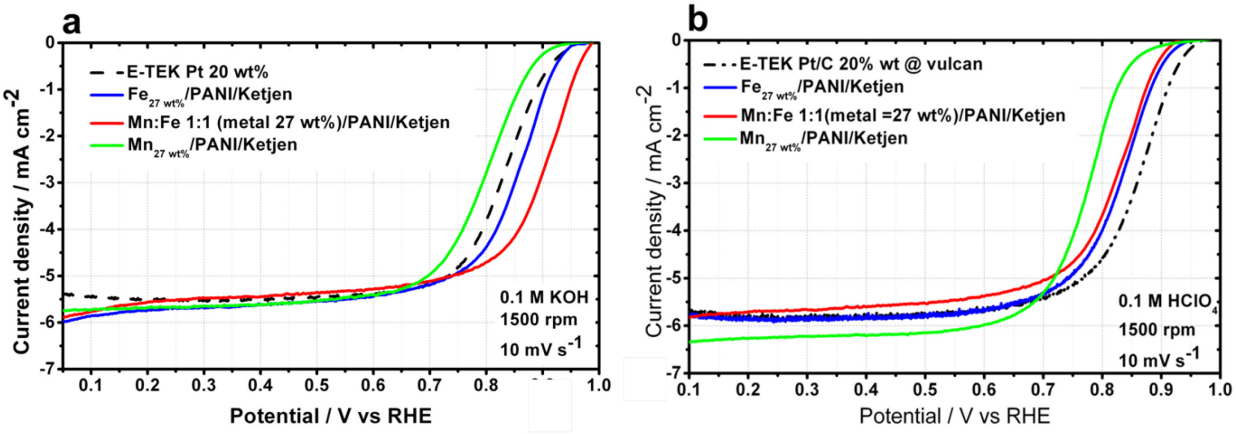

Figure 32. ORR activity of the catalysts in alkaline and acid electrolytes. Electrocatalytic oxygen reduction of best performing mono- and bimetallic catalysts pyrolysed at 900 °C compared with Pt/C 20 wt% a) in 0.1 M KOH (pH 13), b)in 0.1 M $HClO_4$ (pH 1). Conditions: 1500 rpm. O_2-saturated electrolyte at room temperature, non noble metal catalyst loading 0.8 mg cm^{-2}.

The corresponding onset potential (E_{onset}), half wave potential ($E_{1/2}$) and mass activity (I_m) for various catalysts in alkaline medium are summarized in Table 6.

Table 6. Electrochemical characterization results regarding onset potential (E_{onset}), half wave potential ($E_{1/2}$) and mass activity (I_m) for various mono- and bimetallic catalysts.

Catalyst	E_{onset} (V vs. RHE)	$E_{1/2}$ (V vs. RHE)	I_m (mA $mg_{catalyst}^{-1}$)
Fe $_{17\ wt\%}$/PANI/Ketjen	0.79	0.7	1.12
Fe $_{21\ wt\%}$/PANI/Ketjen	0.81	0.74	1.7
Fe $_{27\ wt\%}$/PANI/Ketjen	0.87	0.81	9.5
Fe $_{27\ wt\%}$/PANI/Ketjen_after 2nd leaching	0.9	0.85	25.66
Fe $_{37\ wt\%}$/PANI/Ketjen	0.82	0.78	3.85
Mn $_{17\ wt\%}$/PANI/Ketjen	0.75	0.7	0.5
Mn $_{21\ wt\%}$/PANI/Ketjen	0.8	0.76	1.7
Mn $_{27\ wt\%}$/PANI/Ketjen	0.83	0.77	3.85
Mn $_{27\ wt\%}$/PANI/Ketjen_after 2nd leaching	0.85	0.81	7.5
Mn $_{37\ wt\%}$/PANI/Ketjen	0.8	0.74	1.55
Mn:Fe 3:1 /PANI/Ketjen	0.83	0.77	3.5
Mn:Fe 1:1 /PANI/Ketjen	0.92	0.88	45.32
Mn:Fe 1:1 /PANI/Ketjen_after 2nd leaching	0.95	0.9	46
Mn:Fe 1:3 /PANI/Ketjen	0.93	0.88	33.75

To assess the influence of the nature of the support on the catalytic activity of the final catalysts, the optimized composition of monometallic iron catalyst ($Fe_{27wt\%}$/PANI/Ketjen) was selected for impregnation of nitrogen and iron on graphene oxide (GO) and multi-walled carbon nanotube (MWCNT) as supports. In Figure 33 the ORR activity of these catalysts illustrated compared to $Fe_{27wt\%}$/PANI/Ketjen and Pt/C 20wt% catalysts. In this case, onset potential of 0.8 and 0.79 V vs. RHE was recorded for $Fe_{27wt\%}$/PANI/GO and $Fe_{27wt\%}$/PANI/MWCNT, respectively.

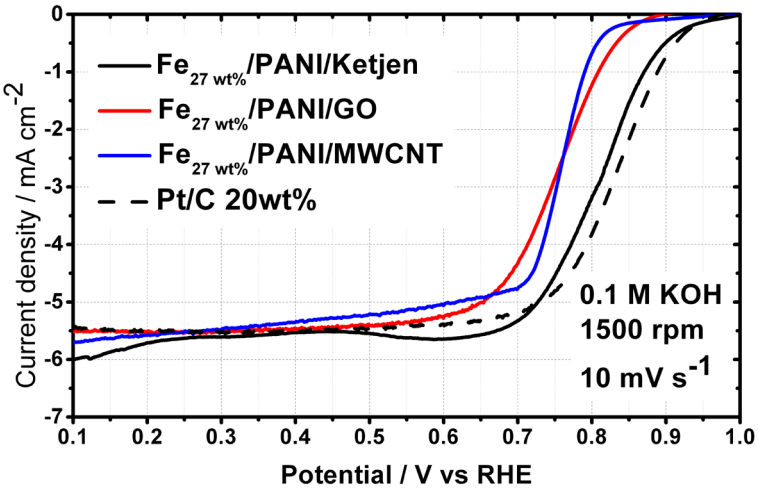

Figure 33. Influence of nature of support on ORR activity. Electrocatalytic oxygen reduction of $Fe_{27wt\%}$/PANI/Ketjen, best performing mono catalyst- pyrolysed at 900 °C supported on Ketjen (black solid curve), graphene oxide (GO) (red solid curve) and multiwalled carbon nano tubes (MWCNTs) (blue solid curve) compared with Pt/C 20 wt% Conditions: 1500 rpm. O_2-saturated 0.1 M KOH, pH 13, electrolyte at room temperature, non noble metal catalyst loading 0.8 mg cm^{-2}.

It can be concluded that Ketjen supported catalysts are more active than GO and MWCNT materials. It can be possibly coordinated with the graphitization degree of the support, meaning high graphitization of GO and CNT hindered the ORR electrocatalysis.

The stability of the best performing catalysts by cycling was investigated in both alkaline and acid media. As shown in Figure 34(a), the catalysts are stable in alkaline even after 9000 cycles. The slight mass activity decrease observed in alkaline electrolyte which is mostly in first step of stability test (between 20 -4500 cycles) compared to the second step (between 4500-9000 cycles). The same stability is observed for Pt/C at high pH, as shown in Figure 34(c). In acid medium, the mass activity of the catalysts decreases more significantly as illustrated in Figure 34 (b). In acid medium, bimetallic Mn:Fe=1:1 shows the highest stability compared to other NNMCs.

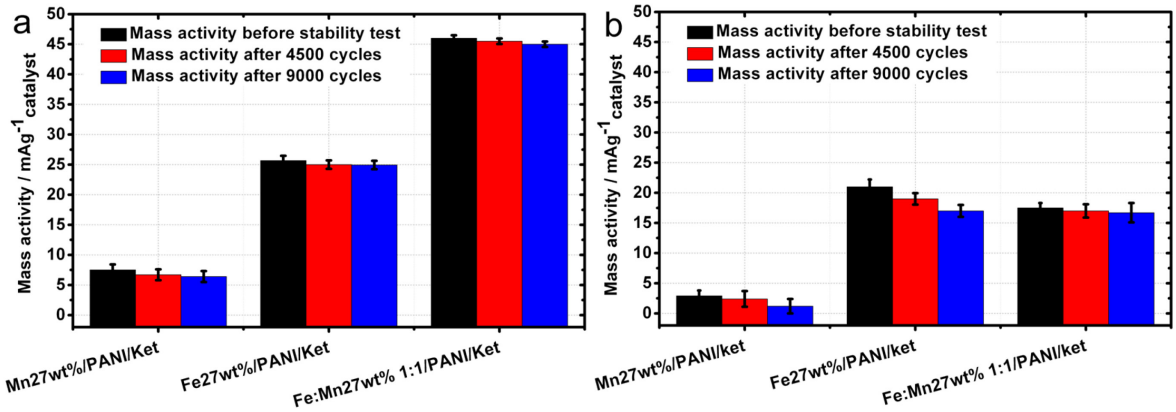

Figure 34. Stability cycling test result of best performing catalysts. Mass activity in a) alkaline and b) acid electrolytes before and after cycling stability tests.

In order to investigate the number of active sites and their chemical environment, pulse chemisorption and TPD measurements were performed by using carbon monoxide (CO) as the probe molecule. Correlating the observed electrocatalytic ORR activities with CO adsorption experiments provides insight into the active site structure and helps finding an answer to the key question, whether metal exists in these sites or not. In pulse chemisorption, variation of the signal associated with peak integration is followed as a function of catalyst activity while in TPD, desorption temperature as a function of metal type is correlated with the metal type.

In pulse chemisorption measurements, peak area corresponds to a pulse of defined volume of carbon monoxide in a helium carrier gas passed over a catalyst sample kept at ~-80 °C. The quantification of the signal loss by integration with and without sample allows us to calculate the quantity of the CO molecules adsorbed on the catalyst. The observed decrease in the carbon monoxide peak area is attributed to irreversible retention of chemisorbed CO on the catalyst. Preliminary measurements showed no interaction between the probe molecule and synthesized materials at room temperature which can be interpreted as weak bonding of the adsorbate molecule and adsorbent surface. To intensify this interaction, further measurements were performed on catalysts which were kept at ~-80ºC.

The PANI/ketjen (metalfree-CN_x) catalyst which was synthesized in the absence of metal and knowingly used as a control material shows no adsorption of CO (no change

in peak area) as it is shown in Figure 35(a). In catalysts synthesized with metal, the CO was effectively adsorbed on surface, resulting in saturation after usually two first injections (see Figure 35(b)). Based on these very first observations, we could conclude that the metal plays a key role in adsorption process.

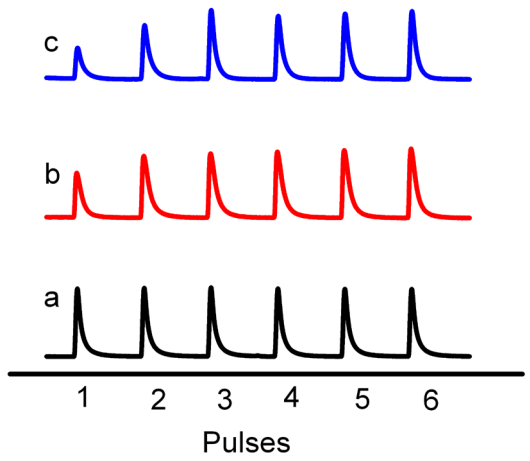

Figure 35. Carbon monoxide (CO) pulse chemisorption profile for a) PANI/Ketjen (CN_x metal-free catalyst), b) $Fe_{27wt\%}$ /PANI/Ketjen after 1st acid leaching/2nd pyrolysis, c) $Fe_{27wt\%}$ /PANI/Ketjen after 2nd acid leaching/3rd pyrolysis.

Although after 1st acid leaching, majority of the metal/metal sulphide moieties are removed from the catalyst but in higher metal loadings, still trace amounts are present in the resulting catalyst recognized by XRD and TEM. To verify that the observed CO interaction is not with metal/metal sulphide particles embedded mostly in carbon texture but rather with metal bonded with nitrogen, we performed a further leaching/pyrolysis step, which results in removal of all the metal particles (based on TEM, XRD). Interestingly, this additional step leads to higher CO adsorption (see Figure 35(c)). This implies that the further leaching step is not only critical to improve the electrochemical activity but is also meaningful in pulse chemisorption results. Lower CO adsorption and lower ORR activity before additional leaching step are likely due to the blocking of active sites by metal particles which limits accessibility of these sites for oxygen in ORR and CO in pulse chemisorption. These results (Figure 35) in combination with RDE results which showed an improvement in onset potential both in acid and alkaline media strengthen our concept that adsorption is taking place on metals present in the active site and not the metal/metal sulphide species present in the catalyst texture. Pulse

chemisorption measurements were performed for mono- and bimetallic catalysts and the CO uptake (mmol $g_{catalyst}^{-1}$) is correlated with mass activity mA $mg_{catalyst}^{-1}$ of the corresponding catalysts in alkaline electrolyte as shown in Figure 36. Apparently, the CO uptake can be positively correlated with the catalyst mass activity, meaning by increasing the catalytic activity of the catalyst, the CO uptake increases. Mn:Fe=1:1 and Fe catalysts (27 wt% metal content) which presented the best performance regarding activity in RDE measurements in acid and alkaline electrolytes, show the highest CO uptake (see Figure 36). The difference in activity of these catalysts in alkaline and acid electrolytes can be attributed to the different mechanism of ORR in two media. Additionally, the small difference in CO adsorption in Fe and Mn:Fe=1:1 catalysts can be relevant to the presence of various metal centres and their interaction with CO.

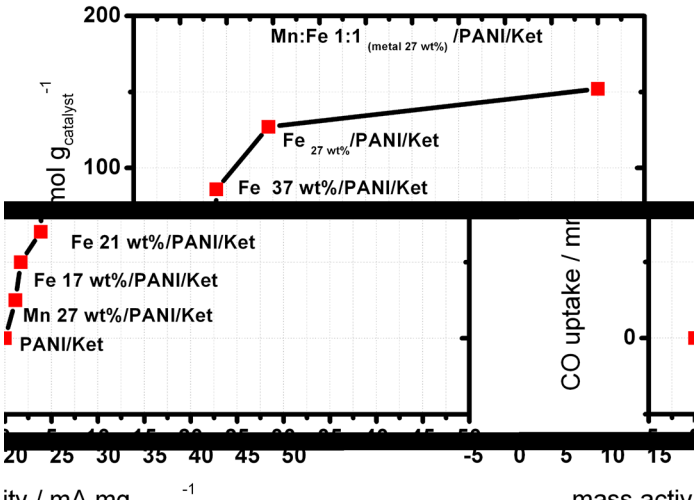

Figure 36. Correlation of mass activity and CO adsorpt ion. Carbon monoxide (CO) uptake (mmol $g_{catalyst}^{-1}$) based on pulse chemisorption correlated with mass activity (mA $mg_{catalyst}^{-1}$) after 1st acid leaching/2nd pyrolysis in 0.1 M KOH based on RDE measurements.

It has to be emphasized that how many CO is adsorbed on one single site and what the active site density is are still controversial.

TPD measurements were applied as a qualitative method to show the presence of different metals in the active site structure. When the temperature is high enough to sustain the activation energy for CO desorption and the process is thermodynamically feasible, the link between the atoms of adsorbate/adsorbent is broken and the phenomena of TPD take place. As depicted in Figure 37, when temperature rises, desorption rate increases and eventually goes through a maximum and finally drops to

zero (baseline) as the surface is completely depleted of adsorbate. A desorption spectrum is a record of the concentration of desorbed gas as a functions of temperature. The shape and the position of the peak maxima (temperature) are related to the desorption process. The representative TPD spectra of $Fe_{27\ wt\%}$/PANI/Ketjen, $Mn_{27\ wt\%}$/PANI/Ketjen and Mn:Fe (metal 27 wt%)/PANI/Ketjen with different ratios are illustrated in Figure 37. Obviously, the desorption temperature and the number of peaks are related to the metal type which is deductively initiating from bond energy of metal and CO molecule. In a monometallic, iron and manganese catalysts, the desorption maxima showed up at ~-14 °C and at ~35 °C respectively. However, in bimetallic MnFe catalysts the presence of a small shoulder at ~-33 °C and one major peak at ~67 °C intensify the possibility of a bimetallic centre coordinated with N in catalyst structure.

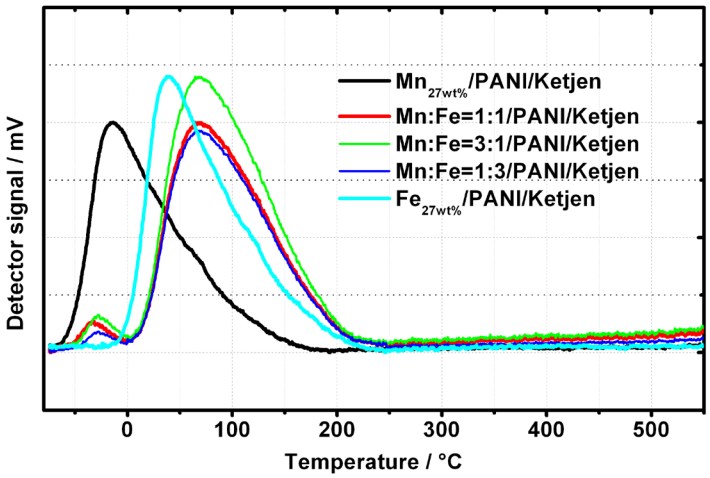

Figure 37. Temperature programmed desorption (TPD) spectrum of three different catalysts (a) $Fe_{27\ wt\%}$/PANI/Ketjen; (b) Fe-Mn (metal 27 wt%)/PANI/Ketjen; (c) $Mn_{27\ wt\%}$/PANI/Ketjen.

The major peak intensity is significantly higher compared to the weaker peak; however this difference can be justified by the metal ratio in final catalyst (see Table 5). Broad peaks can be attributed to various numbers of atoms and their positions connected to Fe and/or Mn which can induce different electron densities on the metal. TPD peaks appearing at various temperatures prove the existence of diverse modes for CO adsorption on active sites which can mainly originate from changes in Me-CO bonding energies.

For all the bi-metallic samples a dominant peak is detected at higher temperature and a shoulder at lower temperature. The position of peak for samples with different MnFe

ratios in TPD is changing slightly as a function of metal content; however a clear trend correlating metal content and peak position is not discernible (see Figure 37).

3.4. Conclusion.

Our results show that i) monometallic manganese catalyst is not active enough for ORR, meaning the best performing $Mn_{27wt\%}$/PANI/Ketjen showed the overpotential of 0.03 V vs. RHE compared to Pt/C in alkaline electrolyte, ii) addition of iron as the most active metal for ORR in non noble metal catalyst groups and application of 2nd acid leaching/3rd pyrolysis are necessary to achieve high performing catalysts, iii) we could show that synergic effect of iron and manganese can increase the ORR activity and stability of bimetallic catalyst with optimum molar ratio (Mn:Fe 1:1) which is superior to Fe and Pt/C reference catalysts in alkaline, iv) bimetallic Mn:Fe=1:1 final catalyst showed a comparable activity to Fe monometallic and slightly lower activity compared to Pt/C in acid electrolyte, v)our monometallic iron catalyst showed a higher activity compared to the previously reported PANI catalysts in alkaline and acid by optimization of the synthesis conditions, in particular application of 2nd acid leaching/3rd pyrolysis [17, 154, 161], vi) for the first time, we could use pulse chemisorption and TPD to attain insight to the active site structure of non noble metal catalysts.

4. Activity and Stability of Hexamethyltetramine (HMTA)-based catalyst synthesized via ball milling for ORR

4.1. Introduction

Catalysts owe their catalytic activity to chemical/ physical functionalities or to specific structure or morphology [162]. An example of catalytic functionality is the heteroatom doping to a carbon backbone or the ability to coordinate to metals, while the introduction of porosity to catalyst is a morphology change. The catalytic function of a doped material combined with porous structure is ultimately based on a change in the electron charge profile which is originated from the replacement of the heteroatom with carbon as well as the pore volume which are helpful for the material to fulfill its tasks [120].

An efficient, yet underexplored strategy for introducing structural modifications to a catalyst is ball milling (BM). High energy ball milling is a process, in which the moving balls transfer their kinetic mechanical energy to the milled material which may result in breaking of chemical bonding, fracturing the material particles or creating novel morphology in the final product. Therefore, ball milling has been used as a mechano-chemical synthesis method for the fabrication of novel nanostructures with tunable and unique functionalities [163-165]. Recently, Dodelet et al. synthesized porous NNMCs by using ZIF via ball milling strategy which results in high ORR performance electrocatalysts. Supposedly, introduction of porous/hollow nanostructures by using ZIF as well as effective N-doping in these materials via BM strategy influenced drastically the electrocatalysis of the prepared materials towards ORR [163, 166-168]. For NNMC showing ORR activity, nitrogen doping degree and BET surface area can determine the active site density which affects the kinetics of the oxygen reduction reaction. Besides, the pore size distribution of the catalyst structure can drastically influence the diffusion of the oxygen and water which are mirrored in diffusion regime of the reaction [166]. Therefore, synthesis by ball milling can be a promising process in ORR electrocatalysis as it influences the doping degree and the morphology of the final products.

Hitherto, various functionalities have been incorporated into the material backbone by ball milling in the presence of appropriate gases or precursors. However, the influence of ball milling on morphology to create the porous structure was just reported in the presence of templates (e.g. ZIF), while in the absence of ZIF templates, reported

works showed cracking of the particles occur as the result of this processing [166]. Additionally, numerous nitrogen precursors are reported for synthesis of NNMCs; as it is agreed that these catalysts are material-based materials. This means that utilization of a novel nitrogen precursor can change the characteristics of the final products. Hexamethyltetramine (HMTA) (Urotropin) with the formula of $(CH_2)_6N_4$ (four "corners" are nitrogen atoms and "edges" are methylene bridges) is a colorless crystalline powder with a symmetric tetrahedral cage-like structure which easily dissolves in water. The crystalline structure of this precursor in XRD is depicted in Figure 38. To the best of our knowledge, this N-precursor was not previously used in synthesis of the ORR electrocatalysts.

4.2. Motivation

In this chapter, hexamethytetramine (HMTA) as a nitrogen precursor with a high atomic N/C ratio was used for the nitrogen doping of the commercial carbon Ketjen via dry ball milling strategy. This is the first time that this nitrogen precursor is used in the synthesis of ORR active materials. The key objectives of this work are to correlate the catalytic activity of materials towards ORR with the starting nitrogen content on the final N-doping degree as well as the influence of ball milling on homogeneity of nitrogen functionality and morphology of the final catalysts. The activity regarding kinetic and diffusion features of different catalysts was mainly coordinated with the nitrogen content, BET surface area, disordered carbon content and ball milling time.

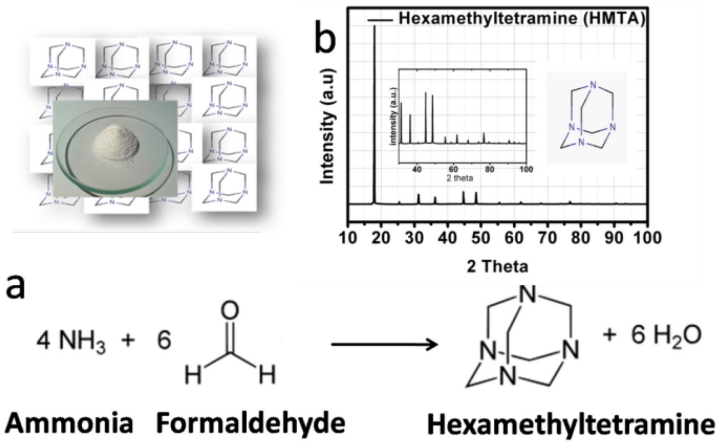

Figure 38. A) Synthesis schematic of hexamethyltetramine (HMTA), b) crystalline structure of HMTA provided by powder XRD.

4.3. Results and discussion

The details of the synthesis are provided in section 2.1.2. In this chapter, the catalysts were named in different synthetic steps as the following: $HMTA_x$-Fe_y-C-z, where x refers to the nitrogen precursor (HMTA) content (g), y refers to the metal precursor (iron acetate, FeAc) content (mg) and z shows the synthesis step: z=1 (mixing before ball milling), z=2 (mixing after ball milling (BM), before pyrolysis), z=3 (ball milled sample and 1st pyrolysed) and z=4 (acid leached sample and 2nd pyrolysed).

In order to explore the morphology and composition of the synthesized materials, TEM/SEM, EA, ICP, powder XRD and XPS techniques were applied. First, to investigate the influence of BM on nanoscale morphology of the catalysts, TEM and SEM micrographs regarding different ball milling time (BMT) and synthesis steps were recorded. TEM micrographs of representative sample for the mixed precursors before BM, $HMTA_2$-C-1, in comparison to the ball-milled $HMTA_2$-C-2 for 500 min is depicted in Figure 39(a) and (b), respectively.

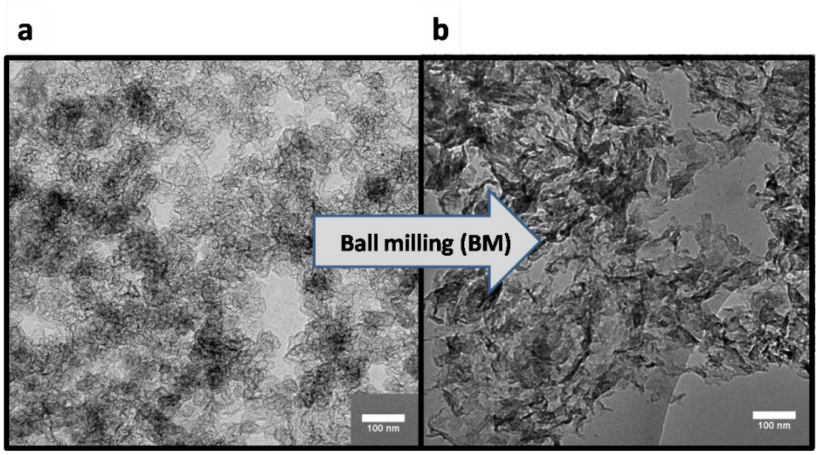

Figure 39. TEM micrographs of a) $HMTA_2$-C-1, mixed precursor before ball milling, b) $HMTA_2$-C-2, ball-milled precursors for 500 min.

At first glance, the morphology of the sample before ball milling, $HMTA_2$-C-1**,** shows isolated Ketjen particles overlaying each other similar to the as-received Ketjen. After BM for 500 min, $HMTA_2$-C-2 morphology changes drastically to a sponge-like structure as illustrated in Figure 39. This observed structure is very similar to the mesoporous carbon material morphology.

TEM micrographs were recorded for $HMTA_2$–Fe_{40}-C in different synthetic steps, as it is depicted in Figure 40. Expectedly, the sample before BM shows the dominant morphology of Ketjen composed of individual particles (see Figure 40(a)).

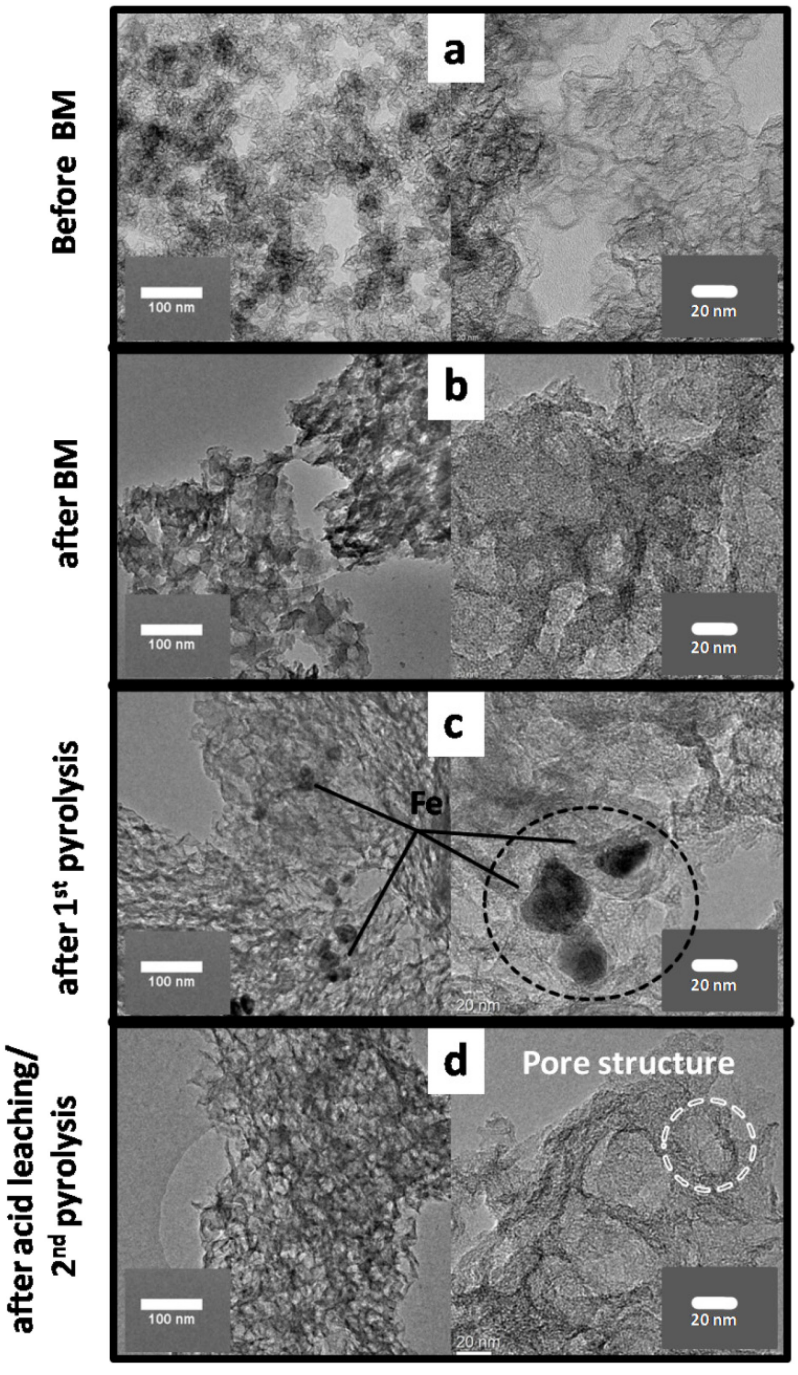

Figure 40. TEM micrographs of $HMTA_2$–Fe_{40}-C, a) the precursors before ball milling $HMTA_1$–Fe_1-C-1, b) ball-milled sample (500 min), $HMTA_2$–Fe_{40}-C-2, c) after the 1st pyrolysis $HMTA_2$–Fe_{40}-C-3, d) after acid leaching step/2nd pyrolysis, $HMTA_2$–Fe_{40}-C-4.

After BM of all the precursors for 500 minutes, the morphology of detached Ketjen particles was changed to a mesoporous-like structure (Figure 40(b).

At the next step, the heat treatment at 900 °C, $HMTA_2$–Fe_{40}-C-3, iron-based particles distributed in the catalyst became apparent while the carbonaceous backbone retained its continuous network morphology similar to the previous step as can be seen in Figure 40(3d). These particles formed as the result of iron acetate (FeAc) pyrolysis at high temperature. Final product after acid leaching and 2nd pyrolysis steps, $HMTA_2$–Fe_{40}-C-4 show the same carbon framework structure without metal moieties (see Figure 40(d)). However, the pores were better defined and grew to a small extent after removal of metal and further heat treatment (see Figure 40(d)). From TEM micrographs, the pore size of ~ 20 nm can be estimated.

Likewise, the catalyst nanostructures were studied regarding the influence of ball milling time (BMT) on the final porous structures. TEM micrographs of $HMTA_2$–Fe_{40}-4 after 100, 300 and 500 minutes ball milling are depicted in Figure 41.

A close look at these micrographs show that after 100 minutes BM the structure is a composite of the carbon nanoparticles and the preliminary formed mesoporous carbon network. However, the spherical morphology of the Ketjen nanoparticles is still observed. Supposedly, 100 minutes ball milling was not sufficient for the agglomeration of the particles to create the final target structure. Increasing BMT to 300 minutes result in a transition structure between 100 and 500 minutes BM; individual particles can even be detected after 300 min BM.

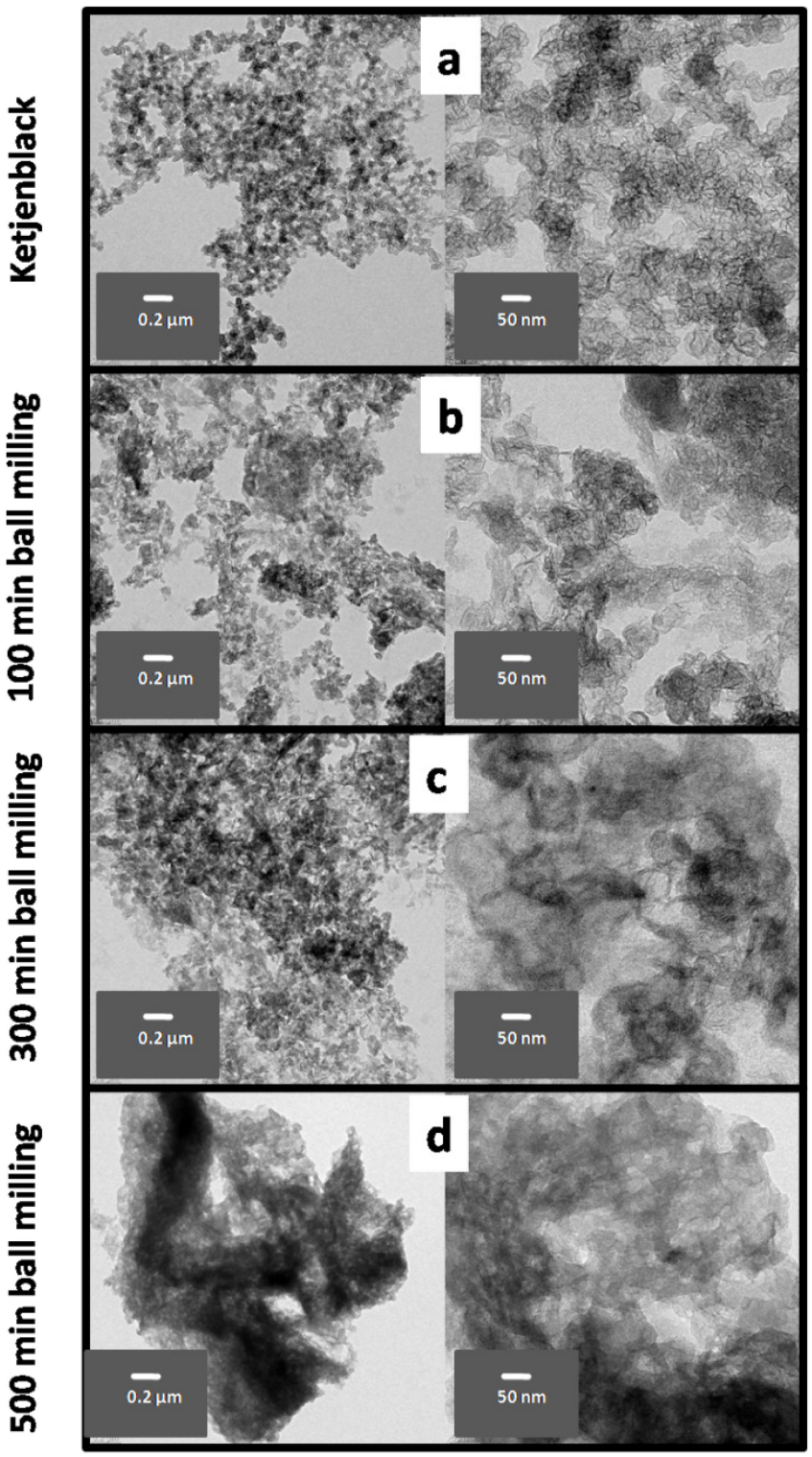

Figure 41. The influence of ball milling time (BMT) on catalyst morphology. TEM micrographs of catalyst $HMTA_2$–Fe_{40}-C, a) before ball milling, b) after 100 min BM, c) after 300 BM, d) after 500 BM.

SEM micrographs were recorded for the prepared samples and are shown for the representative $HMTA_2$–Fe_{40}-C in three critical steps, mixed precursors before BM, after BM and after 1st pyrolysis in Figure 42.

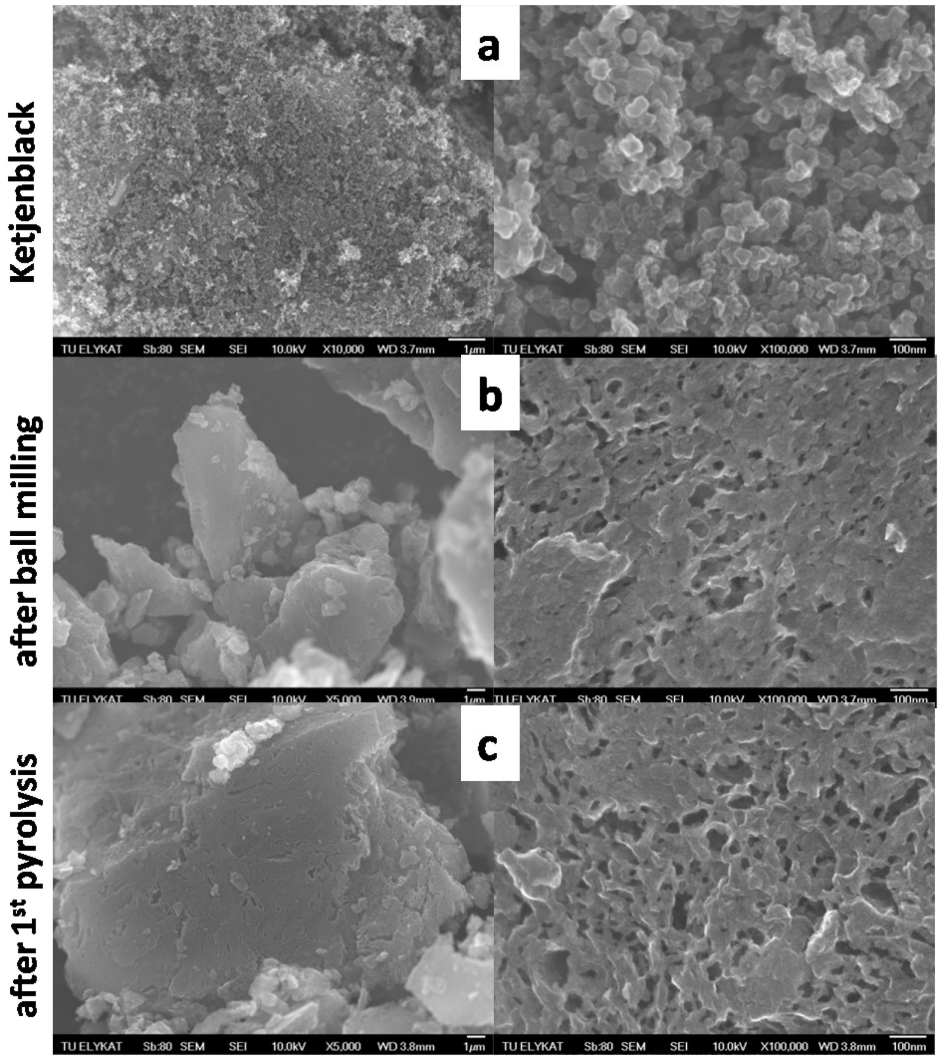

Figure 42. Influence of ball milling (BM) on catalyst morphology. SEM micrographs of a) mixed precursors before ball milling $HMTA_2$–Fe_{40}-C-1, b) ball-milled sample for 500 min $HMTA_2$–Fe_{40}-C-2, c) after 1st heat treatment $HMTA_2$–Fe_{40}-C-3.

Expectedly, before BM, the morphology detected by SEM was mainly the Ketjen nanoparticles as depicted in Figure 42(a). After performing the BM step for 500 min, SEM micrographs in agreement with TEM, show a sponge-like mesoporous structure

(see Figure 42(b)). After pyrolysis, the morphology remained mainly unchanged as can be seen in Figure 42(c).

Additionally, the SEM section micrographs of this sample in a cracking position after BM and 1st pyrolysis are illustrated in Figure 43 with different magnifications. These micrographs confirm the formation of a 3D mesoporous network structure formed by BM of the individual carbon nanoparticles. In accordance with TEM results, SEM confirms that morphology changes from individual particles to a widespread 3D mesoporous structure.

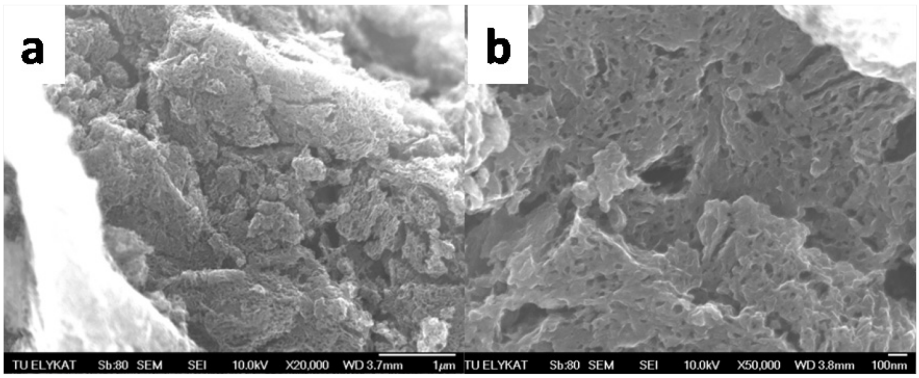

Figure 43. SEM section micrograph of ball-milled precursors (500 min BMT) and after the 1st pyrolysis, $HMTA_2$–Fe_{40}-C-3.

In summary, TEM and SEM techniques revealed the formation of mesoporous-like structure by agglomeration of Ketjen semi-spherical particles (10-20 nm). Most likely, this structure was created first by mechanochemical grinding of particles and subsequent agglomeration of them at high temperature during the BM step. Noteworthy, the BMT significantly influences the homogeneity of the final structures. For the syntheses of further samples, 500 minutes BMT was applied as the optimized time.

BET technique was used to extract more information about the specific surface area and pore size distribution of the synthesized materials treated by BM compared to the starting high surface area Ketjen support. Figure 44(a) details the BET isotherms of the Ketjen (black hysteresis) compared to the representative sample $HMTA_2$–Fe_{40}-C in two important synthesis steps: $HMTA_2$–Fe_{40}-C-2 after BM (red hysteresis) and the final catalyst which went through the pyrolysis and acid leaching steps ($HMTA_2$–Fe_{40}-C-4) (blue hysteresis).

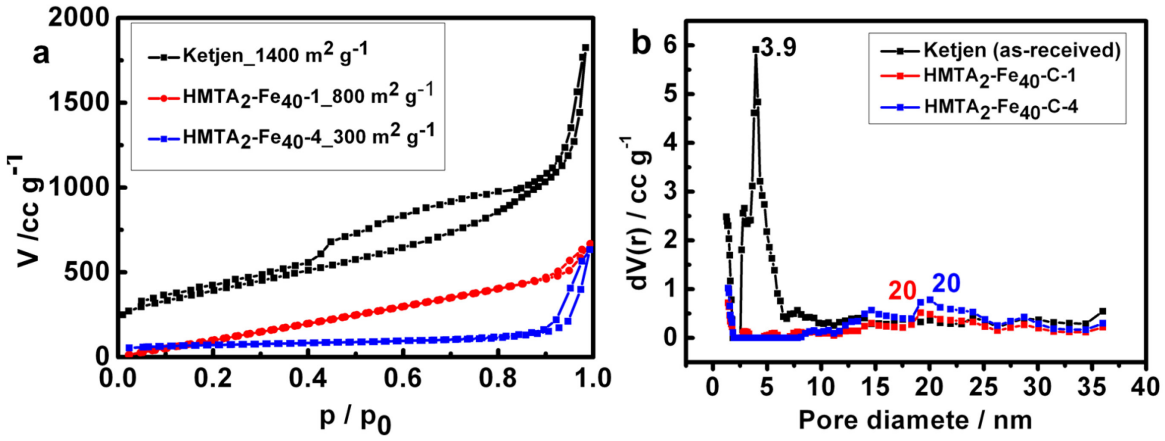

Figure 44. a) Nitrogen sorption isotherms and b) pore size distributions of the $HMTA_2$-Fe_{40}-C at two synthesis steps, directly after ball milling, $HMTA_2$-Fe_{40}-1 (red) and final catalyst, $HMTA_2$-Fe_{40}-4 (blue) compared to Ketjen (black).

Clearly, there are significant differences in the recorded isotherms. The difference is mainly related to the location of the hysteresis loop and its width. The loop positions in ball-milled samples shift to the higher relative pressures implying the increase in pore size diameter. This feature was confirmed by TEM/SEM micrographs which showed the formation of porous material with pore size of ~20 nm. Interestingly, ball-milled sample showed the typical isotherm usually observed for mesoporous materials. Additionally, active surface areas of 1400 m^2 g^{-1}, 800 m^2 g^{-1} and 300 m^2 g^{-1} were recorded for Ketjen (support), $HMTA_2$-Fe_{40}-C-2 and $HMTA_2$–Fe_{40}-C-4, respectively**.** These results show that in the first step of the synthesis, which is BM of the precursors- the surface area decreased to 800 m^2 g^{-1}. Then, further heat treatment and acid leaching steps resulted in another pronounced decrease in the BET surface area (300 m^2 $g_{catalyst}^{-1}$). The pore size distribution data calculated from the adsorption branch of the nitrogen were applied to investigate the effect of the BM step on the pore size distribution in the synthesis course. Figure 44(b) shows the size distribution of Ketjen, $HMTA_2$-Fe_{40}-C-2 and $HMTA_2$-Fe_{40}-C-4. Interestingly, while Ketjen showed a sharp (narrow) size distribution in the range of 2.5-6.5 nm with the maximum at the pore size of 3.9 nm, ball milled samples show a very broad range of size distribution (6.5-25 nm) with the maximum at a pore size of 20 nm. For as-received Ketjen and ball milled samples, $HMTA_2$–Fe_{40}-C-2 and $HMTA_2$–Fe_{40}-C-4, the pore size distribution ranges in mesoporous size (> 2 nm); however, these results clearly show that BM formed larger

pores in the materials.BET values of all the final catalysts are summed up in Table 7. For all the samples, the same trend was observed in BET surface area in different synthesis steps. Noteworthy, the decrease in surface area for metal–free samples is larger. This observation will be discussed regarding nitrogen content in more details in EA part. Additionally, by raising the metal content from 2 to 400 mg, BET surface area increases from 432 $m^2\ g_{catalyst}^{-1}$ to 803 $m^2\ g_{catalyst}^{-1}$

Table 7. Elemental analysis and BET surface area results for different metal containing and metalfree samples at two different synthesis steps, directly after BM and the final catalyst.

Catalyst	Characterization			
	Combustion N wt%	BET ($m^2\ g^{-1}$)	O wt%	Fe wt%
$HMTA_2$–Fe_{400}-C-1	35.14	824	5	4.5
$HMTA_2$–Fe_{400}-C-4	**1.7**	300	0.7	0.81
$HMTA_2$–Fe_{40}-C-1	34.12	803	4.2	0.4
$HMTA_2$–Fe_{40}-C-4	**1.65**	303	0.51	0.12
$HMTA_2$–Fe_{20}-C-1	35.55	795	5.1	0.18
$HMTA_2$–Fe_{20}-C-4	**1.5**	417	0.36	0.04
$HMTA_2$–Fe_2-C-1	36.5	812	4.51	0.05
$HMTA_2$–Fe_2-C-4	**1.3**	432	0.21	0.01
$HMTA_4$–Fe_{40}-C-1	39.12	750	3.1	0.18
$HMTA_4$–Fe_{40}-C-4	**1.4**	386	0.35	0.03
$HMTA_6$–Fe_{40}-C-1	46.5	721	4.6	0.16
$HMTA_6$–Fe_{40}-C-4	**1.45**	354	0.31	0.02
$HMTA_1$-C-1	31.2	702	3.2	-
$HMTA_1$-C-3	**3.2**	488	0.37	-
$HMTA_2$-C-1	38.35	690	4.13	-
$HMTA_2$-C-3	**3.6**	239	0.51	-
$HMTA_4$-C-1	38.47	580	3.12	-
$HMTA_4$-C-3	**4.4**	210	0.17	-
$HMTA_6$-C-1	46.5	500	4.6	-
$HMTA_6$-C-3	**8.25**	198	0.51	-

Clearly, for all the catalysts two consecutive decreases in BET surface area are observed. The first decrease could be attributed to the destruction of small pores of Ketjen particles. After heat treatment, BET is further decreased. This observation could be attributed to the blocking of the Ketjen pores as the result of N-doping during pyrolysis. Additionally, observed BET isotherms are in agreement with the TEM/SEM results. Based on nanostructure morphology, one can explain the changes in isotherm shapes and pore size distribution. For Ketjen, high BET surface area of 1400 $m^2 g^{-1}$ is observed which mostly originates from small pores range from 2.6-6.5 (see Figure 44(b)). In ball-milled samples, the decrease in surface area arose from the particle agglomeration which led to the destruction of small pores which is mirrored in the size distribution profile. For these samples, pore size profile shows broad distributions range from 6.5-25 (see Figure 44(b)). Interestingly, in ball-milled samples, pore size distribution between 2.5-6.5 nm is zero, in which size range, Ketjen show the maximum pore size distribution. Heat treatments and leaching of the ball-milled samples result in further decrease to ~300 $m^2 g^{-1}$ in surface area, most likely due to the filling of pores by nitrogen heteroatom. Size distribution was mainly remained unchanged after the heat treatments/acid leaching in the final catalyst, $HMTA_2$–Fe_{40}-C-4.

Powder X-ray diffraction (XRD) patterns were recorded for various catalysts to explore the crystalline nature of the materials. The XRD reflections in the course of synthesis for the representative $HMTA_2$-C and $HMTA_2$-Fe_{40}-C samples compare to the Ketjen are illustrated in Figure 45. Apparently, Ketjen XRD pattern is composed of two dominant graphite peaks ($2\theta=25°$ and 43°) which originate from the preferred orientation in the commercial carbon. For ball-milled samples, in the first step of the synthesis, directly after BM and before pyrolysis, $HMTA_2$-C-2 sample represents the crystalline structure of starting nitrogen precursor HMTA (see Figure 45). After the heat treatment step, nitrogen precursor was decomposed and the final structure of the metalfree catalyst ($HMTA_2$-C-3) is identified as the graphite crystalline structure (see Figure 45(a)). Final structure of the synthesized material exhibits its most prominent diffraction line at $2\theta=25°$, representing the typical (002) reflex for a graphite-like stacking. This is an evidence of a layered motif within the carbonaceous material. The high intensity shows that the dominant structure motif of the carbon backbone is a stacking of sp^2-hybridised carbon layers. Although, they are limited in their extensions,

indicated by a relatively broadened shape of the diffraction lines. The (100) reflexes at angles of 2θ=43° exhibits lower intensity. This showed that the extension of the layers themselves is decreasing which in turn result in a lower degree of condensation. Interestingly, higher-order reflexes with relatively high peak intensities appeared at 2θ≈61° and 81°. A reflex line at 2θ≈14° with the lowest intensity represented another d-spacing in the graphite structure. These changes in graphite structure referred to the influence of BM step, implying that Ketjen lost its preferred orientation after BM treatment.

For metal containing sample, $HMTA_2$-Fe_{40}-C-2, after BM, crystalline structure shows the characteristic pattern of HMTA, as expected. Heat treatment of the precursors results in decomposition of nitrogen precursor and formation of a mixture of crystalline phases including iron, iron nitride and iron carbide (cohenite) in this sample (Figure 45(b)). After acid leaching, the catalyst structure remains mainly unchanged, however it is expected that iron moieties are removed following this step. Due to the overlay of the cohenite and iron nitride reflexes with iron reflex (2θ ≈ 44°), it is difficult to confirm the effect of leaching on the removal of iron. The reflexes identified for different species are depicted in Figure 45(c). However, TEM and ICP (Fe <1 wt%) results after the acid leaching confirmed that only very small residues of the metal are present in the final catalyst. Moreover, the same graphitized reflex lines could be identified for the final catalyst as explained for metalfree sample.

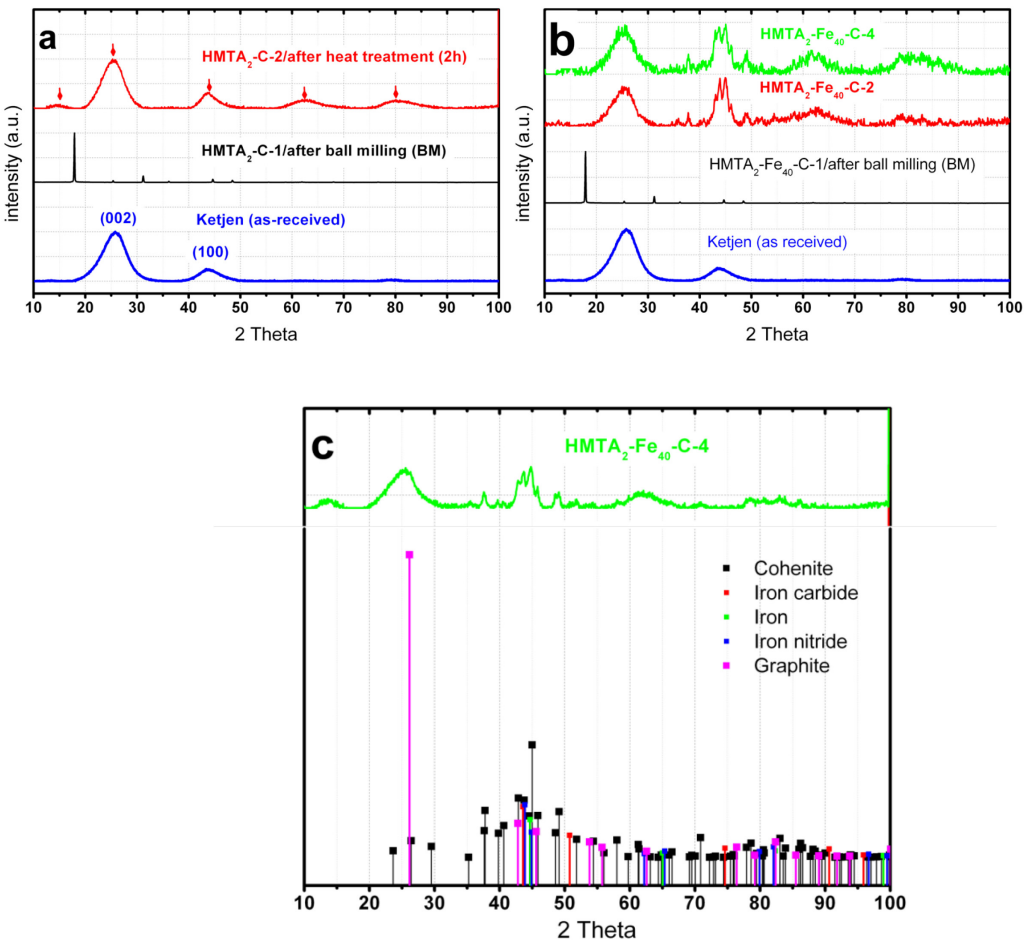

Figure 45. Powder X-ray diffraction patterns of representative metalfree and metal containing samples, a) metalfree sample, $HMTA_2$-C and b) metal containing sample $HMTA_2$-Fe_{40}-C, c) the identified reflexes for different species in $HMTA_2$-Fe_{40}-C.

These patterns were reproducible in each series of metalfree and metal containing the catalysts. Based on XRD patterns, it was clearly observed that in all the catalysts, graphitic structure with numerous orientations are observed after BM step, while in the presence of metal, extra peaks relating to the metal moieties are identified. The presence of disordered graphite was previously reported in the samples synthesized by BM [163, 166-168]. In these works the most intensive (002) peak was observed at 2θ~26.5° and some other peaks at ~10°, 46° (100, 101), 55° (004) and 77° (110) which refer to the different d-spacing in the carbon framework. It is proposed that BM can distort the graphite structure and reduce the size of the (002) plane which is usually mirrored in the broadening of this peak or shifting of above-mentioned peaks. Herein, our ball milled

samples show the most intensive peak (002) at 2θ~25 which is slightly shifted from the position reported previously (2θ~26.5, d-spacing of 0.34 nm). The appearance of the peak with weak intensity at 2θ~14 (d-spacing of 60 nm) can represent a large shift of the (002) peak from 26.5°. Additionally, the other two peaks of 55° and 77° shifted to 61° and 81°, respectively. Therefore, it can be concluded that our XRD patterns are in agreement with other works based on the carbonaceous materials synthesized via BM. Based on these XRD patterns, we can claim that BM is a machano-chemical synthesis strategy as it can change the C-C bonding features which can be depicted in XRD [163, 166-168].

Elemental analysis was used to determine the nominal and final contents of nitrogen in catalysts (see Table 7). While precursors based nominal nitrogen content was high (~34-46 wt%), the final catalysts after pyrolysis show lower nitrogen content ranging from 1.3-1.7 and from 3.2-8.3 for metal containing and metalfree samples, respectively. Obviously, the presence of metal drastically decreases the nitrogen doping onto the carbon backbone in the final catalyst. Additionally, increase of nitrogen precursor content from 1 to 6 g raised the final doping degree from 3.2 to 8.3 in the samples $HMTA_1$-C-3 to $HMTA_6$-C-3, correspondingly. The same trend was observed for the metal containing samples when the nitrogen content was increased. Apparently, change the iron content in different samples while nitrogen precursor was kept identical had not significant effect on the final nitrogen value. In this case, the final nitrogen weight percentage vary in the narrow range of 1.3-1.7 wt% by decreasing the metal in these samples (see Table 7). The observed trend confirmed that independent from the presence of metal, increasing the nitrogen precursor raised the N-doping degree. Additionally, metal decreased the introduction of the nitrogen onto the carbon backbone. Noteworthy, this final nitrogen content measured for metalfree samples were higher than the corresponding values observed for the nitrogen-doped materials discussed in other chapters of this work. These analyses confirmed our concept that high nitrogen/carbon ratio in starting precursors in combination with BM processing can increase the nitrogen-doping degree after high temperature pyrolysis in the metal free samples. The effective N-doping in ball-milled samples has been reported previously which attributed to the resulting disordered graphite structure confirmed by XRD. It has been suggested that the larger d-spacing observed in graphitization structure from XRD

pattern would facilitate the incorporation of N into the graphite structure and therefore the number of active sites[163, 166-168].

The rise in the oxygen level in carbon material might be caused by oxygen in the milling chamber; however this oxygen removed from the material after the heat treatment. (see Table 7)

We now turn to a discussion of the trends observed in elemental analysis (EA) and BET. Obviously, by increasing the N-doping into the carbonaceous structure, BET surface area decreased. This can be attributed to the blocking of the pores with nitrogen. Based on the ICP results summarized in Table 7 independent of the nominal metal content applied for the synthesis, iron content was located in the narrow range of 0.02-0.81 wt%. These very low contents of residual iron detected (<1 wt%) showed that acid leaching step was successfully performed. This observation was confirmed by TEM micrographs recorded for samples after acid leaching, as no iron particles were detected.

Moreover, it was not only crucial to quantify the total nitrogen and iron contents, but also to elucidate the chemical environment of the nitrogen and iron as well as their detailed binding/oxidation states. Therefore, XPS spectra were collected and analysed for the samples listed in Table 8.

Table 8. Contribution of nitrogen species extracted from XPS technique.

Sample	Pyridine / amide, amine / **quaternary N** / oxidized N (%)
$HMTA_1$ –Fe_2-C-2	34 / 37 / **27** / 2
$HMTA_1$ –Fe_2-C-4	34 / 16 / **41** / 9
$HMTA_1$ –Fe_3-C-2	20 / 41 / **34** / 5
$HMTA_1$ –Fe_3-C-4	29 / 16 / **46** / 9
$HMTA_1$-C-3	32 / 8 / **52** / 8
$HMTA_3$-C-3	24 / 10 / **55** / 11

Figure 46 shows the scans of N1s core level regions which were fitted to identify the types of nitrogen in the selected catalysts. Accordingly, in almost all the samples four contributions were found corresponding to pyridine, amide, quaternary and oxidized N functions in the order of increasing the binding energy. The peaks at ca. 398 eV refer to

the pyridinic nitrogen species, whereas the binding energies around 400 eV can be assigned to quaternary nitrogen. It has to be mentioned that quaternary nitrogen is firmly bound into carbon backbone (appear at low binding energy) while weak contributions assignable to oxidized nitrogen species are found at higher binding energy (402 eV). Nonetheless, oxidized nitrogen species were only of minor intensity and thus minor importance. This low level of oxygen is in agreement with EA results, which confirms that the oxygen incorporated during BM is removed from the material after pyrolysis. Additionally, XPS is a surface method, and carbon material tends to oxidize in contact with air, which is represented in this observation.

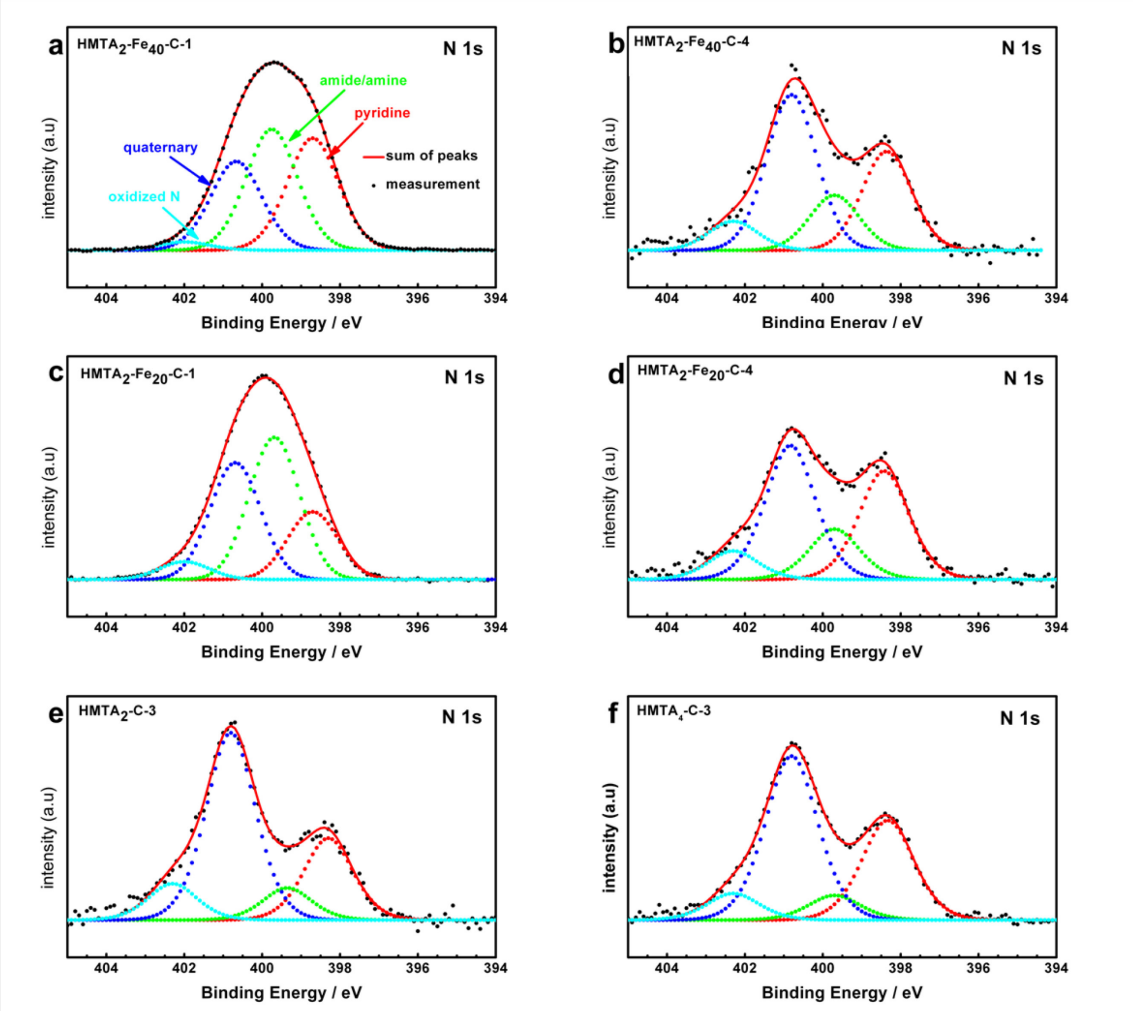

Figure 46. X-ray photoelectron spectra in the N 1s core level range of selected samples.

Accordant evaluations of the scan for the N1s orbital (see Table 8) show that in final catalysts quaternary N is the most dominant species. Contrarily, the chemical environment of the nitrogen atoms in the starting materials after ball milling is mainly amide. These spectra show that nitrogen indeed incorporated fully into the carbonaceous backbone and is not only present on the surface of the synthesized material. Additionally, a remarkable finding lies in the change of intensities between different types of doped nitrogen. Nitrogen is preferably doped at the edges of aromatic carbon layers (quaternary nitrogen). In metalfree samples the ratio between quaternary/pyridinic nitrogen is larger than the corresponding samples synthesized with metal. These results are in agreement with the literature, showing that quaternary nitrogen creating the highest activity in the catalysts. Noteworthy, the relative broad peaks indicating the similar species with slightly different surroundings. Due to small amount of iron and noisy representative spectra, it was not possible to draw more detailed information about the chemical environment of this element. There is no significant differences were observed between N 1s spectra of metalfree and metal containing samples.

In order to provide evidence for the homogeneity of the nitrogen distributed through the carbon backbone, elemental mapping based on energy dispersive X-ray spectroscopy (WDX) was performed for selected samples, $HMTA_1$-C-3 and $HMTA_1$-Fe_1-C-4. The data are depicted in Figure 47, showing clearly that the dopant (nitrogen) is spread homogenously throughout the material. Significant local concentration maxima cannot be observed in the recorded data. In particular, these results must be compared with the elemental mapping results observed for PANI-based catalysts in chapter 3.The nitrogen distribution in PANI-based material is less homogeneous with local accumulation. Noteworthy, the nitrogen doping degree detected in these samples were quiet low. Expectedly, the nitrogen content is higher in $HMTA_1$-C-3 (light points) which is in agreement with EA data.

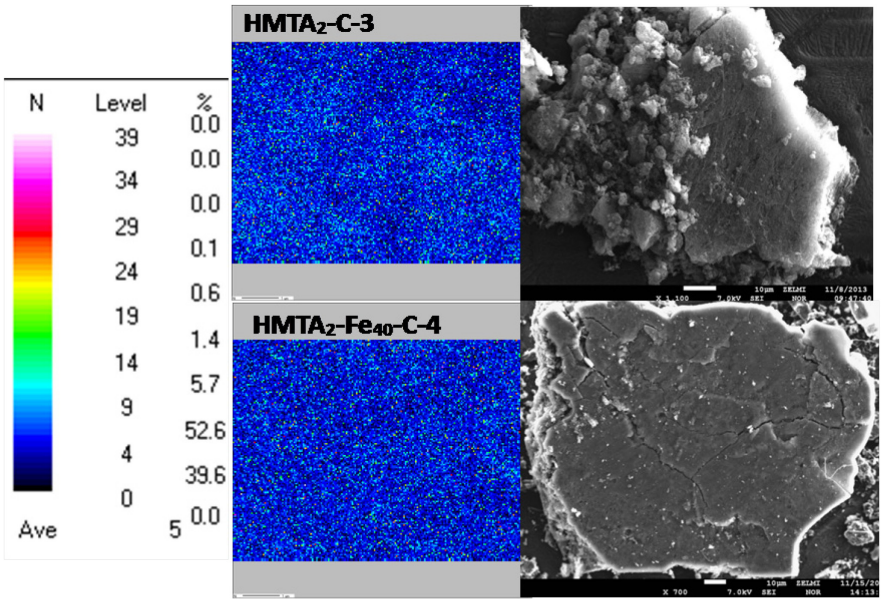

Figure 47. WDX-based elemental mapping for nitrogen measured at 7 kV.

After identifying the composition and morphology of the synthesized catalysts, electrochemical characterization was performed to correlate the catalyst functionality to observed characterizations.

Electrochemical Results. In the following, we tested the ORR performances of the aforementioned ball milled synthesized catalysts using rotating disk electrode (RDE). As the BM was the time consuming step in the synthesis, the optimization was initiated for BMT. In Figure 48(a), LSVs of $HMTA_2$-C-3 with different BMT are compared. Obviously, increasing this processing time causes a consequential difference in the performances of the samples. Noteworthy, the shapes of the LSVs are significantly influenced by the BMT. After 100 min, no defined limiting current is observed. Increasing the BMT to 300 min improves the current measured for the diffusion region. However, further increase to 500 min results in the optimized LSV shape with the current density of 6 mA cm^{-2}, expected for a high performance ORR catalyst. Accordingly, onset potential shifts from 0.79 to 0.81 and finally 0.93 by increasing the BMT from 100 to 300 and then 500 minutes, respectively.

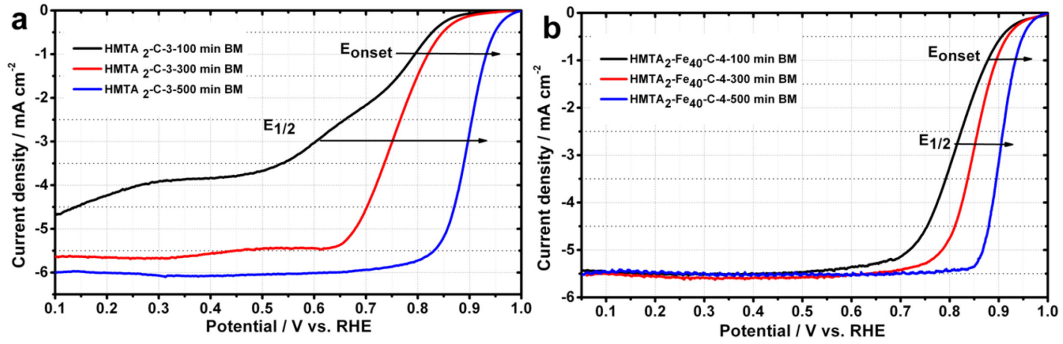

Figure 48. Effect of BMT (100-500 min) on the polarization curves and onset potentials during the electrochemical oxygen reduction reaction (ORR). A) metalfree sample $HMTA_2$-C-3 and b) metal containing sample $HMTA_2$-Fe_{40}-C-4. Conditions: 1500 rpm, cathodic scan rate of 10 mV s^{-1}, O_2-saturated 0.1 M KOH at room temperature.

The same effect is observed for the representative metal containing sample, $HMTA_2$-Fe_{40}-C-4. E_{onset} shifts from 0.88 to 0.93 V by increasing the BMT from 100 to 500 min, respectively; however all the samples show defined diffusion-limiting currents (see Figure 48(b)). Most likely, based on TEM/SEM micrographs, the transition structure from the Ketjen nanoparticles to the partial mesoporous-like morphology after 100 min was not appropriate for the efficient mass transfer in the catalyst films, in particular for the metalfree samples. Therefore, further samples were all processed by 500 min BM to achieve the well-formed porous structure.

Contrary to the catalysts discussed in other chapters of this work, from the very first measurements, the metalfree sample showed a comparable activity to the metal containing synthesized materials. Therefore, by appointing the 500 minutes BM, syntheses proceeded in parallel for both series of metalfree and metal containing groups to optimize the starting precursor ratios in each group.

To evaluate the intrinsic activity of the metalfree HMTA-C samples, linear sweep voltammetries of four materials with different HMTA precursor contents (see section 2.1.2) were recorded in O_2-saturated KOH (see Figure 49(a)).

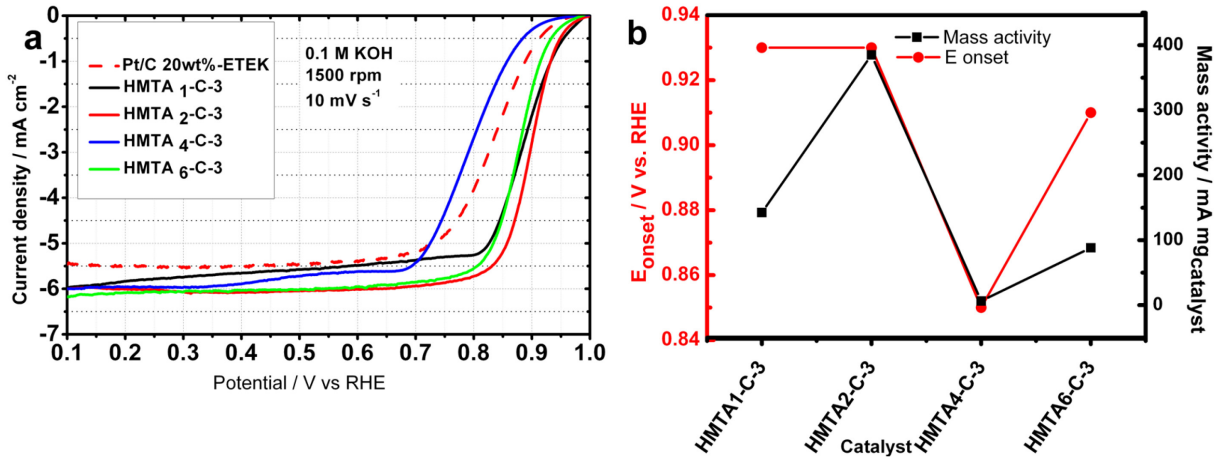

Figure 49. Effect of nitrogen precursor content (2-6 g HMTA) in metalfree catalyst samples ($HMTA_X$-C-3, x=g of the nitrogen content) on the polarization curves and onset potentials during the electrochemical oxygen reduction reaction (ORR). A) RDE polarization curves, b) onset potential and mass activity. Conditions: 1500 rpm, cathodic scan rate of 10 mV s^{-1}, O_2-saturated 0.1 M KOH at room temperature, NNMCs loading 0.8 mg cm^{-2}.

We now discuss the catalytic ORR activity in terms of the onset potential (E_{onset}) and mass activity (I_m), as sometimes different trends are observed for these two values as depicted in Figure 49(b). Notably, the metalfree catalyst $HMTA_1$-C-3 and $HMTA_2$-C-3 show a drastically high activity regarding E_{onset} with 0.07 V positive shifts compared to that of Pt/C reference. Additionally, $HMTA_2$-C-3 represents the highest mass activity (385 mA $mg_{catalyst}$) compared to all other metalfree samples in different chapters of this work. Noteworthy, this ORR activity is exceptionally higher than any other metalfree sample reported in this work. Likewise, a well-defined diffusion current regime and positive half wave potential (0.88 V vs. RHE) verified that this material is highly active with appropriate architecture for mass transportation of oxygen/water. Interestingly, increasing the nitrogen content from the values applied in the synthesis of $HMTA_1$-C-3 and $HMTA_2$-C-3 samples shifts the E_{onset} to more negative potentials and reduces the mass activity of the corresponding samples. This observation confirms that there is an optimum content of the heteroatom which tunes the ORR electrocatalysis. It has to be mentioned that the nitrogen doping degree in the final catalyst is a function of its nominal precursor value as approved by EA results (see Table 7). Furthermore, besides the positive onset potentials which are superior to that of Pt/C and the plateau limiting

currents, extremely positive half wave potentials of as-synthesized catalysts were remarkable which were never observed before for any NNMC reported in this work or the literature [17].

In order to show the influence of metal and its content on the catalytic performance, the ORR activities of the metal containing samples were recorded and depicted in Figure 50. Based on the results reported in other chapters of this work as well as the reported literature, we expected a meaningful improvement in activity by the introduction of metal in the syntheses. Markedly, the onset potential of the $HMTA_2$-Fe_{400}-C-4, the best performing metal containing sample, showed solely 0.02 V improvements to that of $HMTA_2$-C-3 with the identical nominal N/C composition. Decreasing the metal content shifts the onset potential down that is to the higher overpotentials. Typically, E_{onset} shifts from 0.95 to 0.93 V by decreasing the metal content for $HMTA_2$-Fe_{400}-C-4 to $HMTA_2$-Fe_2-C-4, respectively (see Figure 50).

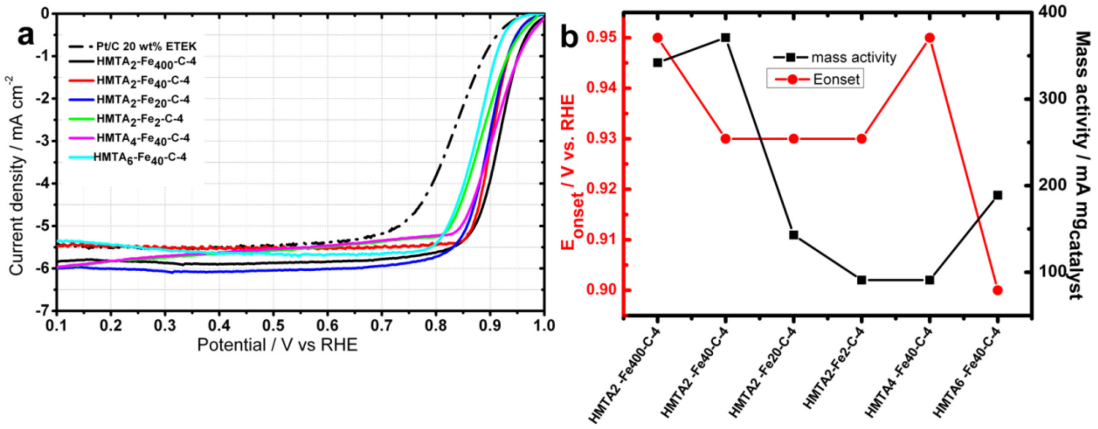

Figure 50. Effect of metal precursor content (2-400 g) in metal containing catalyst samples ($HMTA_2$-Fe_x-C-4, x=mg FeAc) and the effect of nitrogen precursor content in metal containing samples ($HMTA_x$-Fe_{40}-C-4, x=2-6 g HMTA) on the polarization curves, onset potentials and mass activity during the electrochemical oxygen reduction reaction (ORR). A) RDE polarization curves, b) onset potential and mass activity. Conditions: 1500 rpm, cathodic scan rate of 10 mV s^{-1}, O_2-saturated 0.1 M KOH at room temperature, NNMCs loading 0.8 mg cm^{-2}.

This shows that the presence of metal is important in very high contents; however the samples with lower amount show lower activities regarding the E_{onset}. The shapes of the LSVs with $E_{1/2}$ more positive than Pt/C are repeatedly noticed for all the metal

containing catalysts. Obviously, HMTA content in the metal containing samples is also a determining parameter (Figure 50). In this case, high content of nitrogen by using the excessive HMTA precursor fist increase the activity for $HMTA_4$-Fe_{40}-C-4 (E_{onset}=0.95 V vs. RHE) and then decrease for $HMTA_6$-Fe_{40}-C-4 (E_{onset}=0.9 V vs. RHE). Regarding the mass activity, sample $HMTA_2$-Fe_{40}-C-4 show the highest value which is comparable with the I_m calculated for $HMTA_2$-C-3 as illustrated in Figure 49(b).

The electrochemical results regarding onset potentials, half wave potentials, mass activity and Tafel slopes of all the catalysts in alkaline electrolyte are summarized in Table 9.

Table 9. Summary of the E_{onset}, $E_{1/2}$, mass activity (I_m) and Tafel slopes for different catalysts in 0.1 M KOH.

Catalyst	**E_{onset} (V vs.RHE)**	**$E_{1/2}$ (V vs. RHE)**	**I_m (mA $mg_{catalyst}$)**	**Tafel slope (mV $decade^{-1}$)**
$HMTA_2$–Fe_{400}-C-4	**0.95**	**0.91**	147	**48**
$HMTA_2$–Fe_{40}-C-4	0.93	0.9	**371**	**49**
$HMTA_2$–Fe_{20}-C-4	0.93	0.89	143	48
$HMTA_2$–Fe_2-C-4	0.93	0.88	91	62
$HMTA_4$–Fe_{40}-C-4	0.95	0.9	91	45
$HMTA_6$–Fe_{40}-C-4	0.9	0.87	189	61
$HMTA_1$-C-3	0.93	0.9	142	63
$HMTA_2$-C-3	**0.93**	0.88	**385**	**47**
$HMTA_4$-C-3	0.85	0.79	6	151
$HMTA_6$-C-3	0.91	0.87	88	53

To evaluate the PEMFC application of the catalysts, ORR tests were performed in 0.1 M $HClO_4$ for the best performing metalfree and metal containing catalysts. As it is depicted in Figure 51, the onset potential of 0.88 and 0.84 V vs. RHE are observed for $HMTA_2$-Fe_{400}-C-4 and $HMTA_2$-C-3, respectively. Expectedly, the onset potential in the acid electrolyte negatively shifts compared to the corresponding values in the alkaline electrolyte for the catalysts.

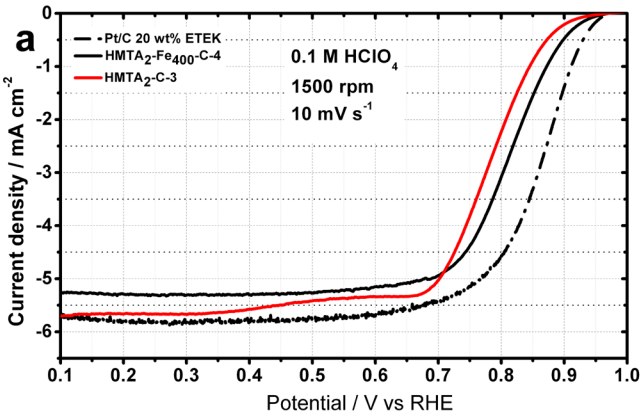

Figure 51. ORR catalytic activity of the best performing metalfree and metal containing samples in acid. Polarization curves of $HMTA_2$-Fe_{400}-C-4 (black solid curve) and $HMTA_2$-C-3 (red solid curve) compared to the Pt/C 20wt% (dashed black curve). Conditions: 1500 rpm, O_2-saturated 0.1 M $HClO_4$ (pH 1), room temperature. NNMCs loading of 0.8 mg cm^{-2} compared to Pt/C 20 wt%, 10 µg Pt.

The diffusion-limited current plateaus were also observed in the acid electrolyte; however the LSVs do not show the same shape as in alkaline medium. In acid, $E_{1/2}$ showed a more negative position compared to that of Pt/C. Noteworthy, in acid media, the metal containing sample showed higher activity compared to the metalfree sample.

Figure 52 presents the kinetically controlled currents, I_k, in the alkaline and acid medium of various NNMCs and the Pt/C catalyst. Tafel slopes are depicted for all NNMCs in the potential interval of 1-0.7 V vs. RHE with the values 45-63 mV $decade^{-1}$ for all the catalysts except $HMTA_4$-C-3 with high Tafel slope (see Figure 52(a)). All the NNMCs have the same loading of 0.8 $mg_{catalyst}$ cm^{-2}. Clearly, $HMTA_4$–Fe_{40}-C-4 catalyst has the best performance regarding the kinetic regime of the ORR.

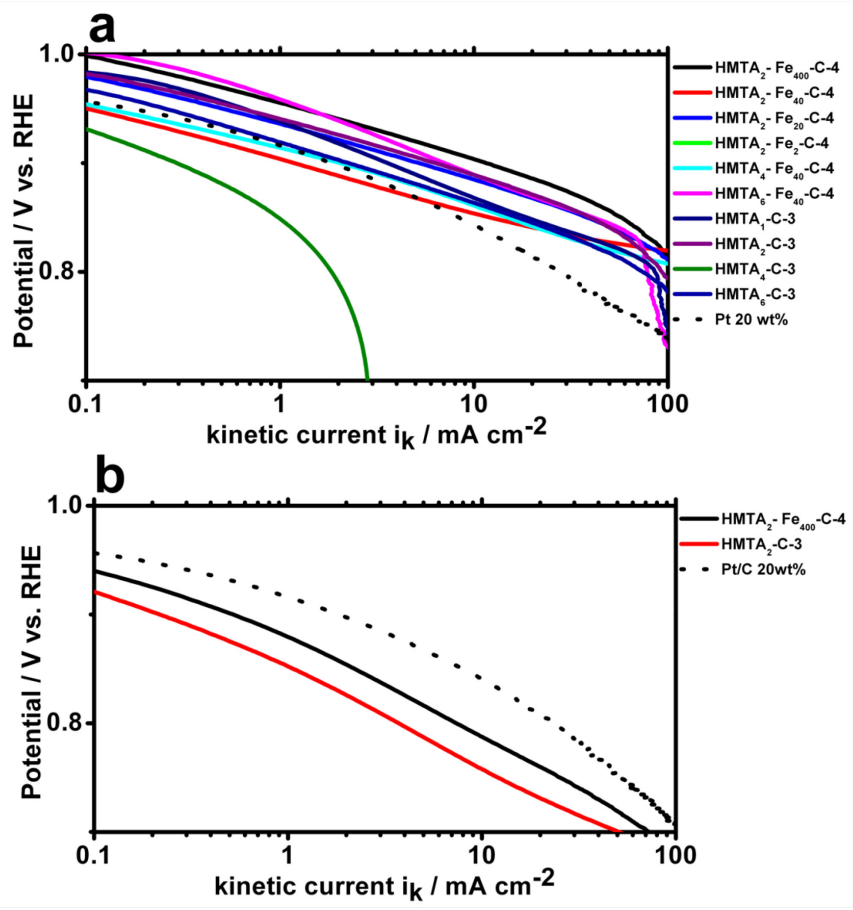

Figure 52. Tafel plots (E vs. log I_k) in RDE at 1500 rpm, O_2-saturated a) 0.1 M KOH (pH 13) and b) 0.1 M $HClO_4$ (pH 1).

In Figure 52(b)., Tafel plots and the corresponding Tafel slopes of selected catalysts in acid medium are compared with Pt/C. In acid electrolyte, the Tafel slope ranges from 83 to 79 for $HMTA_2$-C and $HMTA_2$-Fe_{400}-C catalysts. Obviously, the activity gap for ORR electrocatalysis between metalfree and metal containing samples is more dominant in acid medium.

In order to compare the stability of the synthesized catalysts in acid and alkaline electrolytes, the cycling stability tests were performed for the best performing catalysts. The mass activities before and after 9000 cycles are compared to that of the Pt/C catalyst in Figure 53. Expectedly, in alkaline medium, the mass activities remained unchanged while in acid electrolyte, the activity decreased, in particular for metal containing samples.

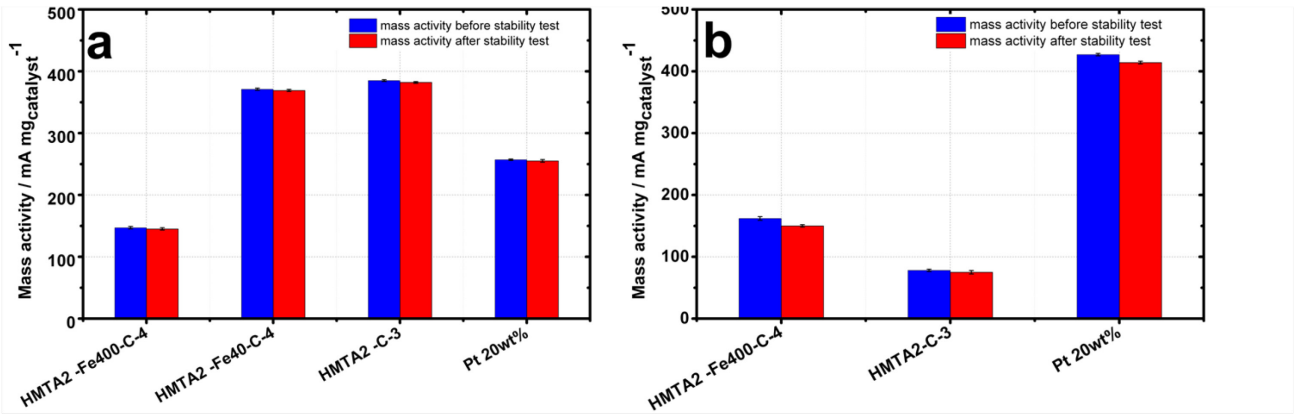

Figure 53. Stability cycling tests of the best performing catalysts. Mass activities at 0.8 V vs. RHE in RDE before and after stability test, a) in alkaline, b) in acid electrolytes.

Based on the achieved RDE results, one can conclude that ball milling is an important step in the formation of the final catalyst and strongly influences the observed catalytic performances. For instance, for sample $HMTA_2$-Fe_{40}-4, when BMT was raised from 100 to 500 minutes, the onset potential also increased from 0.88 to 0.93 V. Additionally, by increasing the BMT from 100 to 500 min, half-wave potential ($E_{1/2}$) shifts by 0.09 V(ΔE_{onset} ~ 0.09 V). These observations could be attributed to an enhanced or more efficient mixing of the precursors which facilitated interaction of nitrogen precursor with the carbon support. It should be taking into regard that in this case, ball milling is replaced for wet impregnation step utilized for other syntheses in this work. The effective interaction in combination with mesoporous-like morphology observed for ball-milled samples are most likely the decisive elements for ORR high performances of these materials. Additionally, we correlate the high activity of the final catalysts to the relatively high final nitrogen content in the materials. As nitrogen is certainly participating in the active site structure, most likely increasing the nitrogen doping degree can increase the active site density. However, there is a saturation level for the effect of nitrogen on electrochemical improvement results. Likewise, BET surface area is also determining in the active site density. BET surface area decreases as the nitrogen content increase (see Table 7). Therefore, most probably in the samples with higher nitrogen content, lower BET surface area result in a higher active site density. This effect is more dominant in metalfree samples. Obviously, the metal containing samples showed high BET surface area and low N-content. Contrary, for the metalfree samples, low BET surface area and high N-content was observed. Apparently, metal decrease the

possibility of the nitrogen doping even in the presence of high starting nitrogen precursor. However, due to the opposite trends observed for the BET surface area and N-content, it is difficult to draw a conclusion which correlate the activity with the N-content and BET surface area.

Positively shifted $E_{1/2}$ and well-defined diffusion currents pointed to an effective mass transport in the catalyst film which can be interpreted regarding the catalyst morphology (TEM/SEM). TEM micrographs showed the formation of different nanostructures for catalysts with various BMT. The morphology changes from individual nanoparticles to 3D continuous network by raising the BMT from 100 to 500 min. We believed that final mesoporous structure facilitates the mass transportation through the material and results in highly positive $E_{1/2}$ and plateau diffusion-limiting current.

4.4. Conclusion

In this chapter we have presented high performance ORR electrocatalysts which were synthesized via a novel and very efficient ball milling process. The synthesis strategy to create the final nanostructure is fast and scalable, while the nitrogen precursor HMTA with its high N/C content is low cost. In this work, high energy ball milling was shown to i) result in high nitrogen doping up to 4-8 wt%, ii) decrease the BET surface area (possibly due to the particle agglomerations), with the change in pore size distribution occurring mostly in the micropore range (<2 nm), ii) introduction of mesoporous-like structure and iv) increase the degree of carbon disorder. Primarily, three superiority ORR electrocatalytic features over other materials can be mentioned: i) very positive $E_{1/2}$, ii) very plateau diffusion current and iii) high ORR activity of metalfree samples regarding onset potential and mass activity. We attribute the high performance of the final materials to the specific holey structure and the mesoporous –like morphology and the effective N-doping of the carbon framework. Since the holey structure with high N-doping provide the catalyst with more active edge atoms, better accessibility to the electrolyte, faster electrolyte/oxygen and water diffusion and movement and larger accommodation space for ions are expected. Besides surface property, N content and species are also crucial in final activity. The materials exhibit an aromatic graphite backbone with remarkably high degrees. Elemental mapping showed a very homogeneous distribution of nitrogen on the catalyst surface while TEM/SEM and BET

isotherms confirmed the mesoporous-like structure of the final catalysts. In particular, the mesoporous-like structure facilitates mass transfer and most likely account for the significantly improved ORR half-wave potential of the prepared catalysts. These results are superior to the previously reported samples synthesized by ball milling [163, 166-168].

5. Heteroatom-doped Carbon derived from Ionic Liquids (ILs) with Tunable Enhanced ORR Performance: Nitrogen and Sulfur-/Phosphorus-/Boron- Co-Dopped Ketjen

5.1. Introduction

The ORR activity of nitrogen doped carbon nanostructures has been widely studied [15, 134, 169, 170]. Recently, other heteroatoms such as sulfur, phosphorous and in particular boron were used for (co)doping of carbon for energy storage applications, specifically oxygen reduction reaction [35-38, 170, 171]. However, all these previously reported materials showed lower ORR performances in the alkaline media than Pt/C catalysts. Numerous starting heteroatom precursors were used in these syntheses. Exemplarily, cyano functional ionic liquids (ILs) as precursors for carbon functionalization are promising starting materials because they have negligible vapor pressure as liquids (nonvolatile, fluid at <100 °C due to the salt-like structure) and are thus easily applicable towards the desired structures and morphologies. The unique architectures of ILs provided the possibility for diverse mixture of anions and cations resulting in the various heteroatom combinations (nitrogen co-doping with sulfur, phosphorus and boron) in the final materials [172]. Since 1914, when ethylammonium nitrate as the first fluid salt under ambient condition was introduced [173], multitude aspects of these precursors have been studied. During last decades, numerous applications of ILs were reported such as their use as solvents/electrolytes or in catalysis. However, their application in the syntheses of the functionalized carbon materials attracted the attention throughout the past few years. Meanwhile these materials have also entered the field of energy storage related applications [174-177].

The direct carbonization of ILs is yet not economical because of the low carbon yield of the final products due to their almost full decomposition into volatile compounds (more than 80 wt % decomposition, based on TGA studies) [120, 178], and the relatively high cost of the ILs in general. Recently, from the material point of view, it was shown that these precursors could be successfully applied for the formation of a thin carbonaceous film on other carbon nanostructures. Achieved composites exhibited significant doping degree of the heteroatoms and the beneficial influence of N-doping in carbons could be maintained, which was shown by the increased stability of electrochemically active platinum nanoparticles loaded on these hybrid materials

compared to those loaded on the untreated carbon host [15].Considering this first success, the application of IL derived carbons should be orientated towards their uses not as the main source of the carbonaceous materials but as the doping agents for functionalization of the plain carbons or creating a thin coating layer in composite materials accompanying with thermally stable carbon backbones.

5.2. Motivation

The influence of versatile heteroatom introduction originated from ILs onto the Ketjen structure on ORR activity of a spectrum of (co)doped materials was investigated. Selection of the ILs enabled us to designate simultaneous co-doping with two heteroatoms. The systematic synthesis procedure was followed to examine the synergic effect of N-doping and other heteroatoms (S, P, B-co-doping) with the aim of adjusting the properties in regard of electrocatalysis towards oxygen reduction reaction in alkaline and acid electrolytes. In these syntheses, the main structure of the precursor saved unchanged while the heteroatom is changed, so the observed drift in the activity could be correlated with the heteroatom type. Furthermore the influence of iron presence and its content in the catalyst composition was explored.

5.3. Results and discussion

The details of the synthesis of these catalysts are provided in section 2.1.2. The synthesis procedure and the starting precursors are depicted in Figure 54 and 55, respectively.

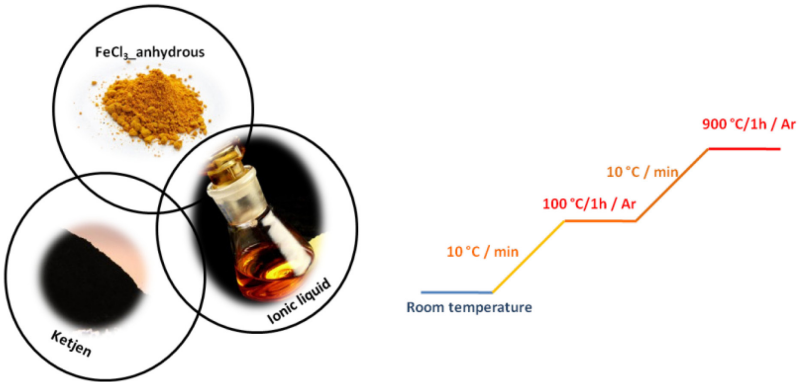

Figure 54. Schematic of the synthesis procedure for heteroatom-doped carbon material.

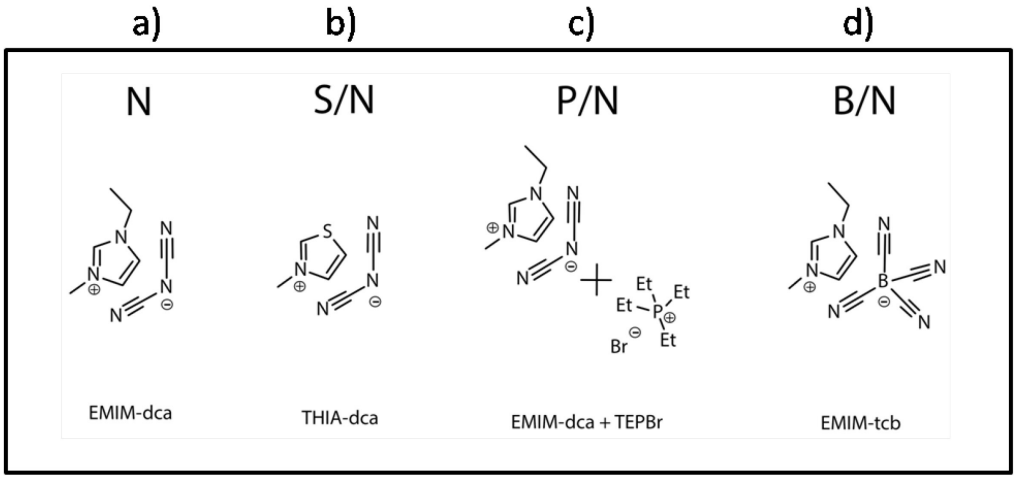

Figure 55. Molecular structure of different ionic liquid (IL) precursors (systems); a) *N,N*-ethylmethyl-imidazolium-dicyanamide (EMIM-dca) (used as N precursor); b) *N*-methyl-thiazolium-dicyanamide (THIA-dca) (used as S/N precursor); c)tetraethylphosphonium bromide (TEPBr)(used as P containing additive together with (EMIM-dca); d) *N,N*-ethylmethyl-imidazolium-tetracyanoborate (EMIM-tcb).

All obtained materials were analyzed regarding their microporosities (BET), morphologies (TEM/SEM) and their heteroatom contents/chemical environments (EA and XPS). By the nitrogen sorption isotherms measured on the as-synthesized materials, it can be shown that the microporosities of the final catalysts remained mostly unchanged as no severe drop of the BET surface area was observed compared to the starting Ketjen support. Therefore, it can be concluded that only negligible blocking of the micropores took place as the result of heteroatom doping of the carbon support. This feature can be followed in Figure 56. The major shape of the isotherms are not significantly altered by functionalizing the carbon support as in all the cases the isotherms can be classified as type I [179]. Thus, all the synthesized materials are microporous, while the relatively high slopes at the highest relative pressures represent a deviation from an ideal type I isotherm. This feature indicates the contributions of external surface area to the isotherm, which can be easily explained by the particular structure of the carbon. The particles also seem to aggregate and thereby form interparticular porosities, which are derived from the presence of very broad hysteresis

loops (type H3) [177, 180]. The surface areas lie between 800 $m^2 g^{-1}$ and 1100 $m^2 g^{-1}$ for most samples, with an exception for the metal free B/N-functionalized one.

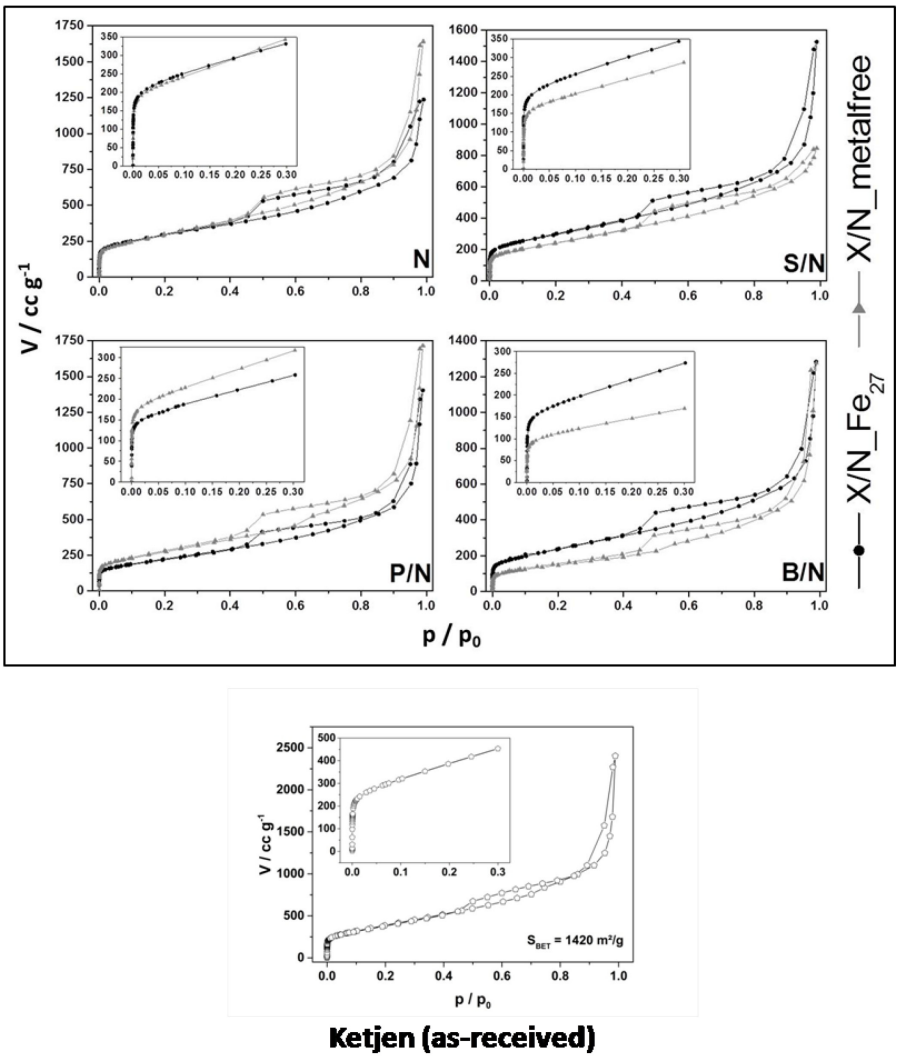

Figure 56. Nitrogen sorption isotherms of different materials synthesized with metal free protocols or using FeCl3 (27 wt% Fe respective to carbon during synthesis).

For B/N co-doped sample, the surface area loss is a bit more pronounced, but the resulting surface is still reasonable and the low pressure region of the isotherm still represents a significant microporosity. The effect of slightly reduced surface area can generally be explained as an additional component is added to the material and thus the probability of partial pore blocking is increasing.

The BET surface areas of different samples are summarized in Table 10.

Table 10 Composition of different single- and co-doped final catalysts based on elemental combustion analysis (EA) for C, N , S and ICP-OES for P, B, Fe, All values given in wt%. Nitrogen sorption (BET) surface area of differently functionalized carbon samples.

Sample		Elemental analysis					BET ($m^2\ g_{catalyst}^{-1}$)
		Combustion (wt%)		ICP.OES (wt%)			
		N	S	B	P	Fe	
N	Ketjen	-	-		-	-	1420
	metal free	2.35	-		-	-	1072
	N_Fe$_{27}$	1.24	-		-	1.44	1043
	N_Fe$_{10}$	1.03	-		-	1.12	918
	N_Fe$_{5}$	0.93	-		-	0.86	1125
	N_Fe$_{27}$_2	1.13	-		-	0.89	1072
	N_Fe$_{10}$_2	0.72	-		-	0.79	1169
	N_Fe$_{5}$_2	0.79	-		-	0.81	1174
S/N	**metal free**	2.82	-		-	-	881
	SN_Fe$_{27}$	1.51	-		-	1.54	1079
B/N	**metal free**	6.61		3.44	-	-	990
	▪ **BN_Fe$_{27}$**	2.34		0.29	-	1.34	806
P/N	**metal free**	1.64	-		2.87	-	530
	PN_Fe$_{27}$	1.96	-		1.32	1.48	885

A further important aspect is the homogeneity of the samples. It must be proven that the functionalized materials are formed homogeneously. Therefore, the possible formation of bulky nanostructures resulting from direct carbonization of ILs in the interparticular space of the Ketjenblack must be excluded. Only if a homogeneous structure is evidenced, a functionalization of the activated carbon can be concluded, while the parallel existence of two carbon species can be excluded.

Scanning electron microscopy (SEM) micrographs that have been obtained for the Ketjen (EC 600J) reference and exemplarily for the S/N_Fe_{27} material was used to evaluate the homogeneous structure of the functionalized materials. The morphology consisting of partially crosslinked particles is well maintained and not altered by the functionalization of support (see Figure 57). Furthermore, no interparticular bulk carbon residues can be identified, which is a clear hint on the successful functionalization of the carbon. It can thus be concluded that the interaction between the Ketjen carbon and the ionic precursors is sufficient to avoid the isolated carbonization of the precursors and to favor the functionalization. Therefore, one can claims that the materials under discussion are correctly described as homogeneously functionalized carbons or carbon hybrids.

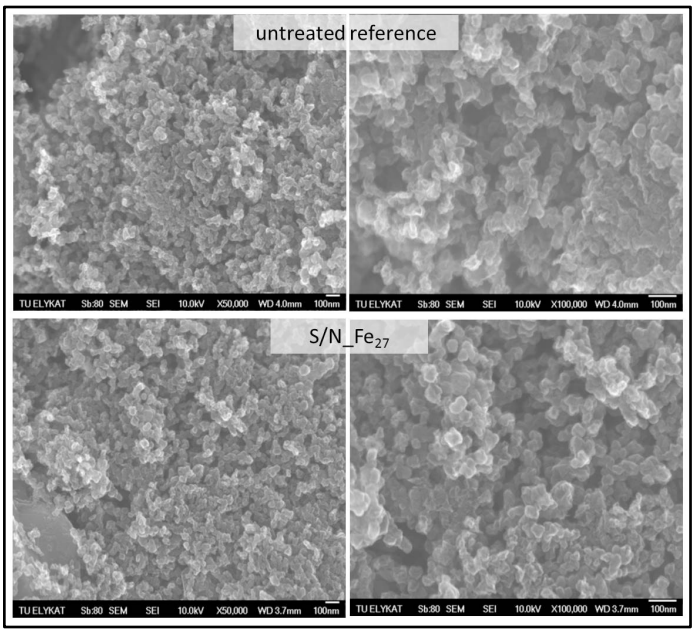

Figure 57. Morphology of support compared with IL-derived catalyst. SEM micrographs of untreated reference (Ketjen_as-received) and S/N_Fe_{27}.

A deeper insight into the particle size can be extracted from transmission electron microscopy (TEM). In comparison to the micrographs obtained from pure and untreated Ketjenblack carbon (see Figure 58 a), no significant changes can be tracked in the images obtained from of all synthesized materials. The TEM images for S/N_metalfree and S/N_Fe_{27} samples depicted in Figure 58 b and 58 c, respectively. The functionalized carbon nanoparticles depicting the size range of 10-50 nm which is identical to the Ketjen. Also these micrographs show the homogenous particular structure of the functionalized materials. Therefore, SEM and TEM techniques confirmed that in this case, ILs acted only as the doping agent for commercial support functionalization.

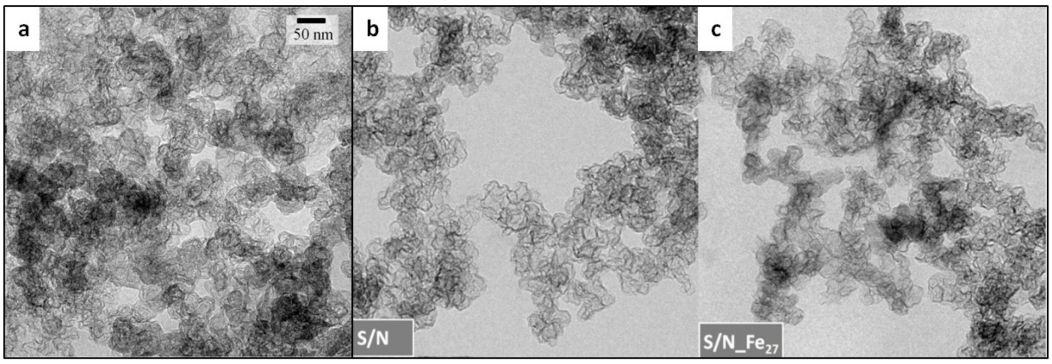

Figure 58. TEM micrographs of a) Ketjenblack (as-received); b) S/N-metalfree functionalized activated carbons and c) S/N_Fe_{27}. Scale bar is valid for all images.

While questions about the porosities, surface areas, morphologies and homogeneities could be answered, the major aspect of these materials still requires elucidation: the heteroatom-doping degree. As mentioned before, four different doping profiles have been targeted including: pure N-doping and N-doping with the additional co-dopants sulfur, phosphorus or boron, respectively. To elucidate the influence of doping on the catalytic functionality in the final materials, both doping quantification and determination of the chemical environments of the doped heteroatoms are crucial. While it is generally known that all applied precursors are suitable to form the respectively doped carbonaceous materials [181-183] under annealing, the primary analysis was performed by either elemental combustion analysis (EA) or Inductively Couple Plasma Optical Emission Spectroscopy (ICP-OES). The results can be followed in Table 10 (All values given in wt%).

Obviously, all the treated materials with ILs yielded the corresponding heteroatoms in the final carbon structures. It was interesting to see the influence of the iron chloride during the formation reaction. The metal is likely mediating the chemical reaction towards the doped carbon systems in a way that leads to a reduced incorporation of heteroatoms, except for the nitrogen in the P/N materials. Exceptionally, the amount of nitrogen is extraordinarily high for the metalfree B/N sample. We propose that it is due to the higher amount of polymerizable nitrile groups in the anion of the starting ionic liquid precursor used. This is nevertheless regulated in the B/N_Fe_{27} sample.

Powder X-ray diffraction offers an insight into the crystalline structure of the synthesized material, in particular the chemical state in that iron remains in the materials. The according XRD patterns are depicted in Figure 59.

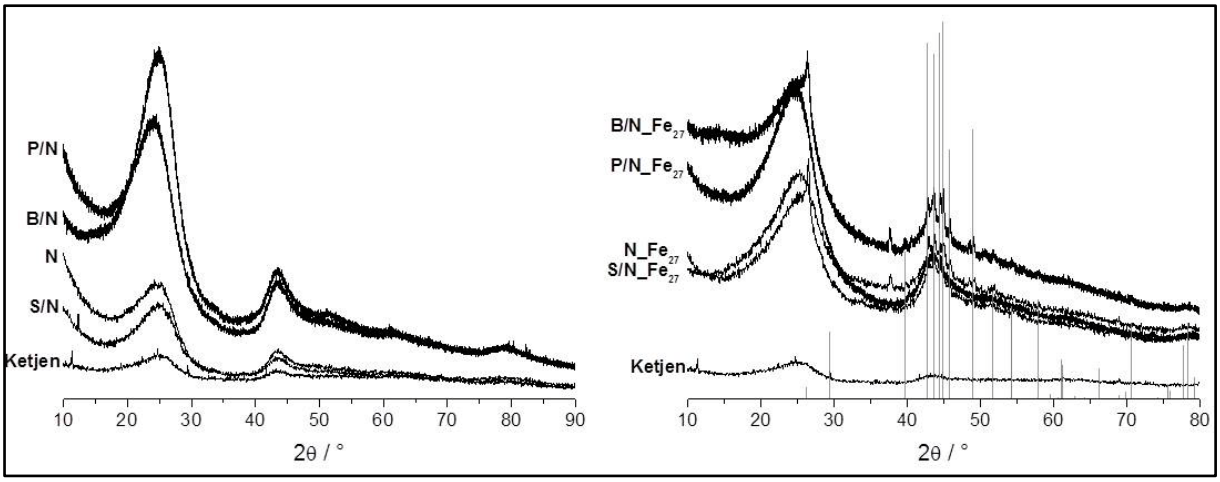

Figure 59. Powder XRD patterns of the differently functionalized materials. Left panel: metalfree / Right panel: Fe_{27}-materials. Grey lines indicate database derived Fe_3C diffraction lines.

All the X/N_Fe_{27} materials (except P/N_Fe_{27}) seem to have the iron residues in the form of iron carbide (cohenite) species, which is concluded from a comparison to database derived diffraction patterns of iron carbide [184]. Interestingly, this is not the case for P/N_Fe_{27}. Although, the iron content of this material is not decreased in comparison to the others (based on ICP results, see Table 10), no iron carbide diffraction is identified. Therefore, the iron must be present in a different chemical state here which is most likely not in a crystalline phase. This featureless XRD pattern for P-

doped material has been previously reported for P-doped carbon with Co [38]. Additionally, the XRD patterns exhibit the typical shape of condensed carbon materials with a limited degree of graphitization characterized by the broadened reflexes. Nevertheless, due to the thermal treatment the graphitization is slightly increasing during the functionalizing of the materials, which can be derived from the comparison with the pattern of the untreated Ketjen reference. However, pyrolysis even in the presence of metal in the X/N_Fe_{27} materials is not strongly influence the graphitization degree. Most likely, this is because real graphitization anyways occurs at much higher temperatures (>2000 °C). Apparently, iron has not strong influence on the graphitization of the IL-derived carbon. The more detailed information of the chemical environments of the heteroatoms in the functionalized materials could be derived from X-ray photoelectron spectroscopy (XPS) data. Iron could not be detected in the XN_Fe_{27}samples, which is astonishing considering the results of ICP-OES and the XRD patterns. This observation can be attributed to the high surface sensitivity of XPS. Apparently, iron carbide or other iron residual species are not present directly at the surface of the carbon particles. It is more likely that these iron sites are trapped within the micropores of the carbons and thus do not contribute to the XPS spectra. Furthermore, the identified oxygen spectra are attributed to the typical phenomenon as the surfaces of carbon materials tend to oxidize slightly when handled under ambient conditions. Usually, the resulting oxidation degree is sufficient to be detected in XPS. To achieve a more profound understanding of the influence, the detailed scans of the different heteroatom core levels (N1s, S2p, P2p, B1s) have been analyzed. The peaks have been deconvoluted and the different contributions have been assigned to different binding states of the respective element. The N1s core level spectra were investigated as depicted in Figure 60.

For the studied samples, all the N1s core level spectra exhibited an asymmetrical shape, meaning a broadened contribution at high binding energy values of < 404 eV. This broadness on the one hand can be attributed to the oxidized nitrogen species on the materials' surfaces. On the other hand, the feature can be interpreted as a satellite peak caused by π-electrons of nitrogen atoms bound in an aromatic chemical environment. This satellite feature is thus already elucidating initially the chemical state of the nitrogen atoms in the differently functionalized carbons. Most likely, nitrogen atoms

firmly bound into the carbon backbones created this characteristic, comparable to the effect seen in the C1s spectra in which the asymmetric shape was caused by a delocalized electron system. This is definitely confirmed by the presence of the two more dominant peak contributions that appear in all N1s spectra, at binding energies between 398.2 eV and 398.7 eV and at binding energies between ~400 eV and ~401 eV. The former corresponds to pyridinic or pyrrolic nitrogen, thus nitrogen atoms bound at the edges of graphite layers. The latter corresponds to graphitic nitrogen atoms, thus nitrogen atoms truly replacing carbon atoms in graphite-related binding environments with the excess electron delocalized in the π-system. Therefore, one can conclude that in these materials, the nitrogen is firmly incorporated into the carbon backbone of the functionalized material. This is the preferred position for the heteroatom in the doped carbon materials applied as electrocatalysts for the ORR. The comparison between the N1s orbitals in the single-doped nitrogen and co-doped samples showed no significant difference. This implied that no synergic effect of the second heteroatom was observed for different nitrogen species. It is also crucial to analyze the role of the iron chloride which is used in some of the syntheses. A comparison of the X/N_metalfree and the X/N_Fe_{27} samples shows that no clear tendency of the metal mediator on the formation of one of the two different major nitrogen bonding states can be identified.

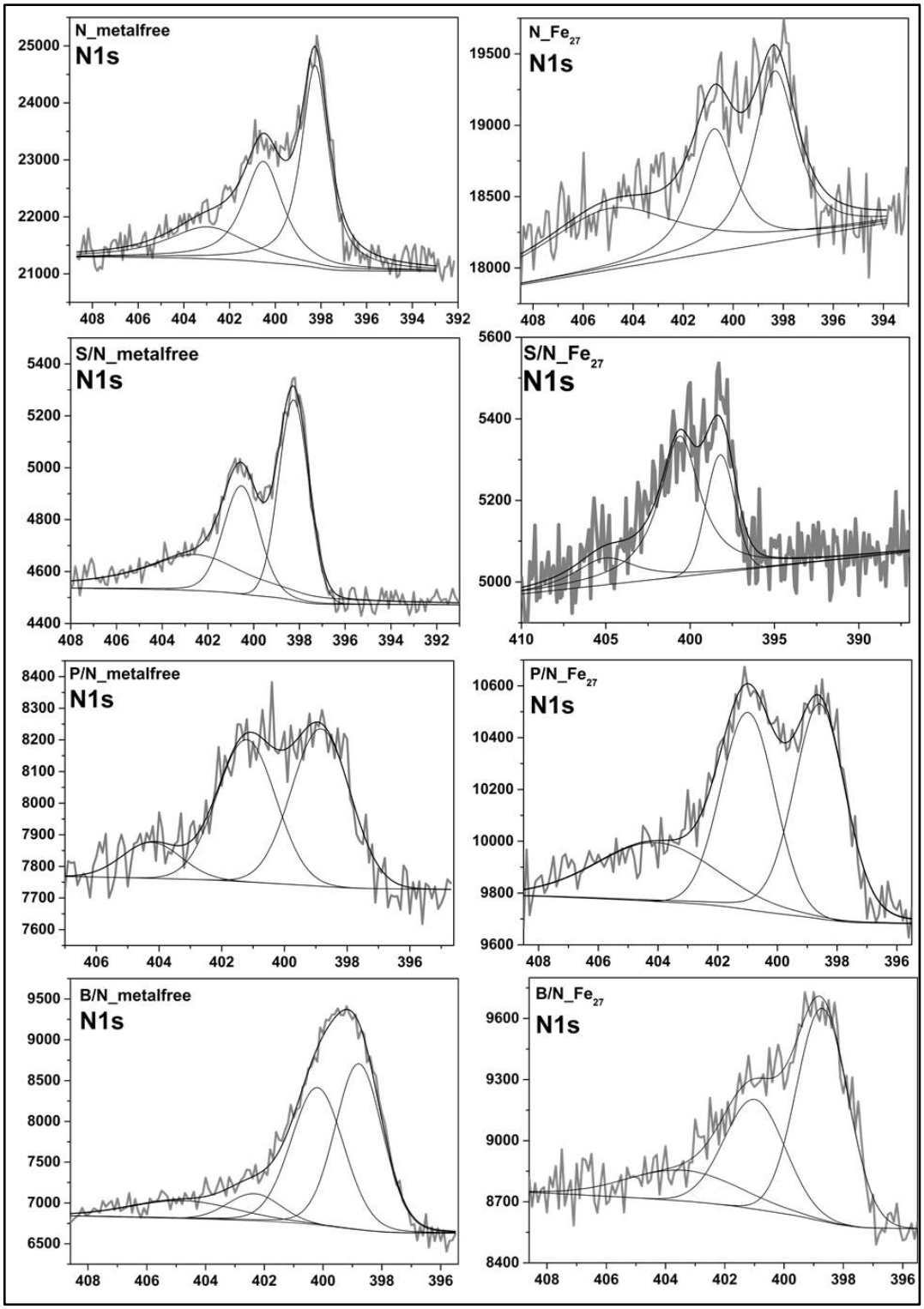

Figure 60. N1s core level XPS spectra of all X/N_metalfree and X/N_Fe27 materials. (x-axes: BE / eV, y-axes: counts/s).

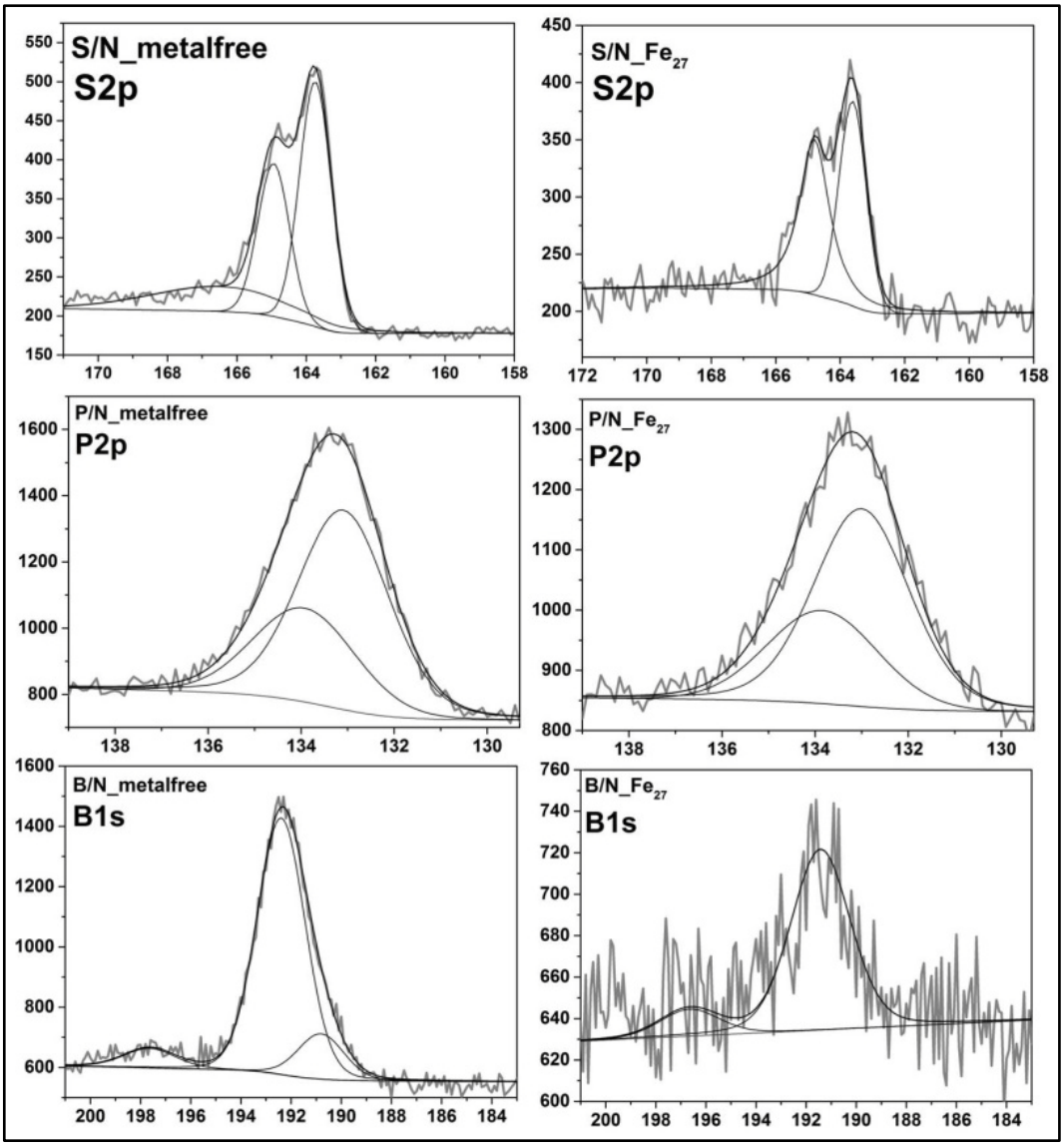

Figure 61. XPS core level spectra. Upper panel: S2p for S/N materials; medium panel: P2p for P/N materials; lower panel: B1s for B/N materials. (x-axes: BE / eV; y-axes: counts / s).

Apart from the nitrogen, the other heteroatoms in the co-doped materials were analyzed using the core level spectra of the S2p, P2p and B1s orbitals. The spectra including their deconvoluted peaks are depicted in Figure 61. A closer look at the S 2p core level spectrum reveals that both S/N_metalfree and S/N_Fe_{27} exhibit identical chemical environments for the sulfur atoms in the materials. The splitting into two peaks with maxima at ~163.6 eV and ~164.8 eV represents the spin-orbit related peak splitting of 1.18 eV for the S2p core level [185]. We can thus conclude that most likely the sulfur atoms are bound in one predominant chemical state. Binding energies of

~163.6 eV for the S2p 3/2 peak can either refer to aromatic, thiophene-like binding environments [185], sulfur bridges between aromatic carbon features or sulfur atoms building up double bonds to carbon [186]. The binding energies of sulfur atoms in these various chemical states are lying close to each other and can thus hardly be clearly distinguished. Yet they have the important idea in common that all representing sulfur that is firmly bound into a carbonaceous material, and thus a successful incorporation of the sulfur is evidenced. Furthermore, in studies on sulfur-substituted carbon nitride rather identical chemical binding energies have been reported, suggesting S-C-N-binding sites (caused by the replacement of nitrogen atoms in triazine units by sulfur) [187]. This is an additional hint on the successful co-doping of sulfur and nitrogen into the electrocatalyst.

Phosphorus was analyzed according to the P2p core level spectra. Although the amount of phosphorus varies between P/N metalfree and P/N_Fe27, the chemical environment of phosphorus is basically identical, as it can be seen in the medium panel of. Although two peaks appear in the deconvoluted spectra, this is only derived from the spin orbit related splitting of the P2p peak and refers to only one chemical binding side. The P 2p 3/2 peak at 133.02 eV (P/N_Fe_{27}) or 133.09 eV (P/N_metalfree) most probably represents phosphorus atoms directly bound to nitrogen [188]. Such a phosphazene-like binding environment could nevertheless not be clearly detected for nitrogen in the N1s core level spectra, which is due to the very similar binding energy to graphitic nitrogen. Another chemical state to that a binding energy of ~133 eV may refer are quaternary alkyl phosphonium sites, which is nevertheless more unlikely considering the high synthesis temperature [188].

Due to the relatively low amount of boron in the B/N_Fe_{27} the respective B1s core level spectrum (lower panel) is very noisy and the signal to noise ratio does not allow for an elucidating peak fitting. It can be estimated that the major peak exhibits its maximum between 191 and 193 eV, and weaker contribution at higher values of binding energies may be assumed. Due to the much higher amount of boron the B1s core level scan for the B/N metalfree material allows for a more explicit evaluation of the spectrum. Two dominant contributions appear at ~192.4 eV, and – with less intensity – at ~190.9 eV. These values nevertheless do not refer to boron atoms exclusively bound to carbon, as boron carbide related structures exhibiting smaller

values for the binding energies at < 189 eV. The binding energies rather refer to boron atoms directly neighboring nitrogen atoms, as similar binding energies have been reported for boron nitride materials [189]. The very broad and weak contribution at higher binding energy values may be a hint on the incorporation of the boron atoms into a graphite-like system, or refer to oxygenated boron species at the surface of the material.
Summing up all data derived from XPS measurements, it can be concluded that the materials under discussion can entirely be described as carbon materials with a structure exhibiting graphitic characteristics, while different heteroatoms are firmly bound and incorporated within these carbon backbones. Regarding the co-doped material a significant difference between the S/N-functionalized and the P/N- and B/N-functionalized materials can be determined: While for P/N and B/N the different types of heteroatoms seem to be predominantly neighboring each other with direct bonds between P and N or B and N, respectively, the sulfur and nitrogen atoms in the S/N-co-doped materials seem to be more independent from each other, as no evidence can be found for direct bounds between S and N. This crucial difference seems to have a tremendous influence on the electrocatalytic performance of the materials, as will be subject of the following chapters of this manuscript.

Applying various instrumental techniques, we could successfully show that the synthesized materials have the same microporosity and morphology of the starting carbon support. The applied synthesis strategy resulted in a homogeneous final structure confirmed by TEM/SEM. Regarding the metal in the synthesis precursors, for all the samples, except for phosphorous-doped, iron carbide crystalline phase was detected. Furthermore, XPS characterizations showed that different functionalized samples have the same functionality regarding chemical environment of heteroatoms.

Electrochemical Results. RDE characterization of heteroatom-doped catalysts was first performed on metalfree nitrogen-doped Ketjen in the alkaline electrolyte. Recorded linear sweep voltammetries (LSVs) of this catalyst compared to Pt/C and Ketjen (as-received) as blank and reference catalysts, respectively, are illustrated in Figure 62(a). The onset potential for the N-doped metalfree sample is at 0.68 V vs. RHE which shows a significant improvement in comparison to the Ketjenblack. However, it exhibited 0.2 V higher overpotentials compared to Pt/C (0.88 V vs. RHE). Additionally, not well-

defined diffusion current regime represents an inappropriate architecture of this starting catalyst for diffusion of oxygen/water. Measurements were continued for the samples synthesized with different iron contents. The results show a pronounced increase in the activity of catalyst having 5 wt% iron by 0.18 V positive shifts in the E_{onset} from the metalfree sample (see Figure 62(a). Detecting a well-defined diffusion current is additional evidence showing that the presence of metal in the synthesis process can facilitate the diffusion of oxygen/water through the catalyst film during the reaction.

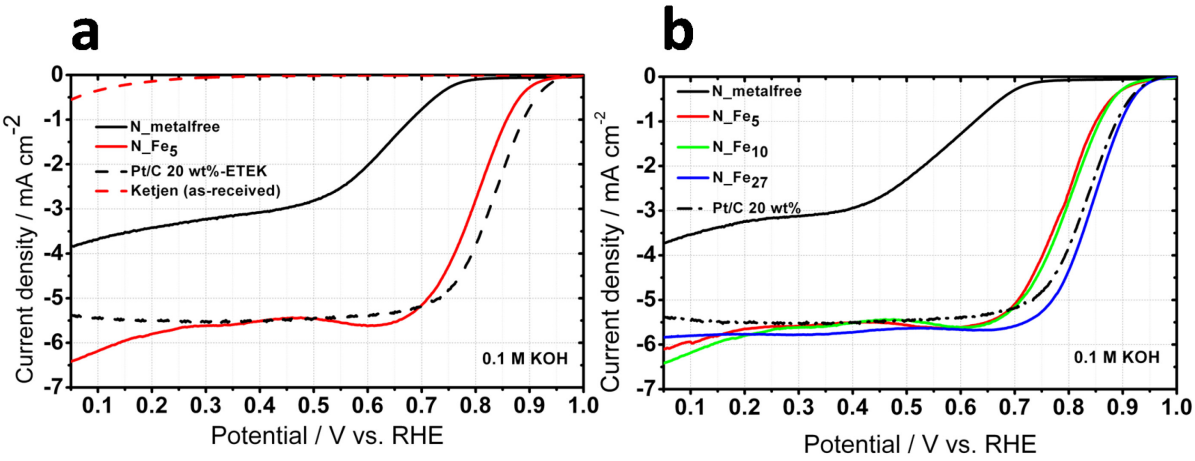

Figure 62. Effect of metal and its content on ORR electrocatalytic activity of the heteroatom doped-catalysts. Polarization ORR curves of a) N-metalfree (solid black curve), N_Fe_5 (solid red curve), Pt/C 20 wt% (dashed black curve) and Ketjen (as-received) (dashed red curve). b) different nominal Fe loadings, N_Fe_5 (solid red curve), N_Fe_{10} (solid green), N_Fe_{27} (solid blue curve) compared to N-metalfree (solid black curve). Conditions: O_2-saturated 0.1 M KOH at room temperature, rotating speed 1500 rpm, scan rate 10 mV s^{-1}, non-noble metal catalyst loading 0.8 mg cm^{-2} and Pt loading 10 µg cm^{-2}.

Noteworthy, the E_{onset} improvement observed for the Ketjenblack sample to N_Fe_5 is so far larger than the E_{onset} shift for the samples with different iron contents. While the 5 and 10 wt% metal containing materials show the same E_{onset} by overlaying of their voltammograms in the kinetic regime, the E_{onset} improves only 0.04 V by increasing the metal content from 5 wt% to 27 wt% (as shown in Figure 62(b)). Observing a plateau and well-defined diffusion current in all iron containing synthesized materials can strengthen the role of metal in the creation of the ORR-compatible catalyst structure.

In the next step, the RDE measurements were performed for the samples synthesized with 27 wt % nominal iron content as the optimized value with different heteroatoms. Accordingly, 27 wt% metal containing S/N, P/N and B/N synthesized catalysts were tested for ORR activity as depicted in Figure 63. Voltammograms show that the S/N_Fe_{27} (E_{onset}=0.93 V vs. RHE) is the most active catalyst system as its onset potential exceeds Pt/C. Other co-doped samples have lower E_{onset} ~0.86 V vs. RHE.

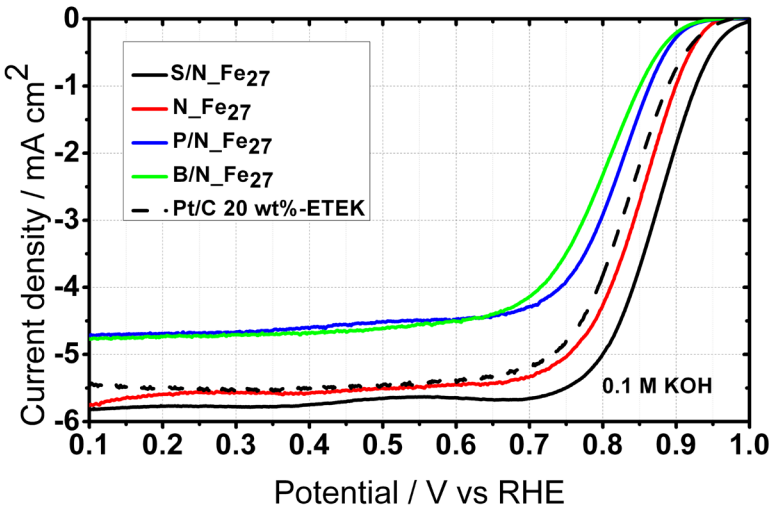

Figure 63. Effect of heteroatom type on catalytic activity. Polarization ORR curves of N_Fe_{27} (solid black curve), S/N_Fe_{27} (solid black curve), P/N_Fe_{27} (solid red curve) and B/N_Fe_{27} (solid green curve) compared with Pt/C 20 wt%. Conditions: O_2-saturated 0.1 M KOH, room temperature, rotating speed 1500 rpm, scan rate 10 mV s^{-1}, non-noble metal catalyst loading 0.8 mg cm^{-2}, Pt loading 10 µg cm^{-2}.

However, there is no significant difference between the materials co-doped with nitrogen and B or P with the nitrogen single-doped carbon. All these measurements carried out for 0.8 mg cm^{-2} loading of the final catalysts.

For further investigation, we performed the ORR test for the catalysts which were treated with the 2nd acid leaching and 3rd pyrolysis. While for previous samples, 0.8 mg cm^{-2} loadings are the optimized value to reach the most positive onset potential; these supplementary steps enable us to obtain the target E_{onset} with 0.4 mg cm^{-2} loading. As it is shown in Figure 64, apparently, the mass activity of N_Fe_x-2 (2 representing the 2nd acid leaching) values doubled after further acid leaching/pyrolysis step. In these samples, the final mass activities are independent of the nominal metal content and

show the same value (~ 13 mA g^{-1}). Mass activities of all the materials in the alkaline electrolyte are compared in Figure 64 and will be discussed in more details in the stability test section.

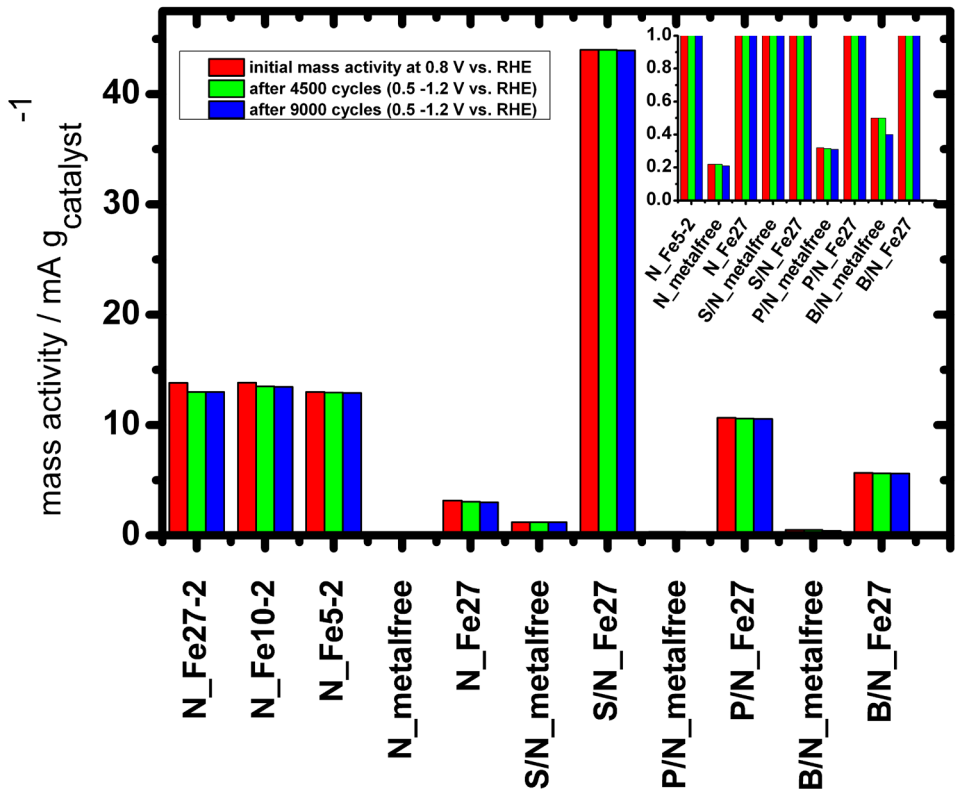

Figure 64. ORR mass activities at 0.8 V vs. RHE in RDE before and after stability tests measured after 9000 cycles from 0.5 to 1.2 V vs. RHE with the scan rate of 50 mV s^{-1} in 0.1 M KOH at room temperature.

All the RDE results regarding E_{onset}, $E_{1/2}$ and $i_{diffusion}$ for different single- and co-doped samples in alkaline electrolyte are summarized in Table 11

Table 11. Summary of E_{onset} (onset potential at 1 mA cm^{-2}), I_d and I_m (mass activity at 0.8 V vs. RHE) values for single- and co-doped samples in 0.1 M KOH. Non-noble metal catalyst loadings are 0.8 mg cm^{-2} except for N_Fe_x-2 samples with 0.4 mg cm^{-2} loadings. The RDE experiments were carried out at room temperature, rotating speed 1500 rpm, scan rate 10 mV s^{-}.

Catalyst		E_{onset}	$E_{1/2}$	I_d	I_m
N	metal free	0.68	-	Not defined	0.22
	N_Fe_{27}	0.9	0.85	5.7	8.25
	N_Fe_{10}	0.86	0.8	5.5	7.16
	N_Fe_5	0.86	0.79	6.4	5.8
	N_Fe_{27}-2	0.86	0.85	0.91	13.82
	N_Fe_{10}-2	0.85	0.84	0.91	13.84
	N_Fe_5-2	0.86	0.829	0.9	13
S/N	S/N-metalfree	0.85	-	Not defined	1.21
	S/N_Fe_{27}	**0.93**	**0.87**	**6.3**	**44**
P/N	P/N-metalfree	0.7	-	Not defined	0.32
	P/N_Fe_{27}	0.86	0.82	4.7	10.65
B/N	B/N-metalfree	0.78	-	Not defined	0.5
	B/N_Fe_{27}	085	0.8	4.7	5.65
Pt	Pt/C	0.88	0.82	5.5	

The ORR performances of metal containing samples were evaluated in the acid electrolyte (0.1 M $HClO_4$). Due to the low activity of metalfree samples even in alkaline electrolyte, these catalysts were not tested further in acid medium. In Figure 65, LSV of S/N_Fe_{27} is typically illustrated in acid and alkaline media. The onset potential of S/N_Fe_{27} is only 0.04 V negatively shifts compared to the reference Pt/C reference catalyst in the acid electrolyte. This activity improvement is a pronounced behaviour for non-noble metal catalysts in $HClO_4$ environment.

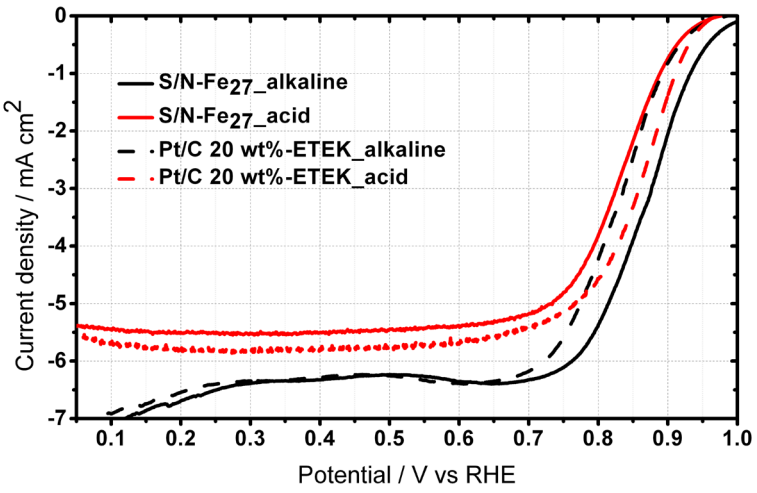

Figure 65. ORR electrocatalysis of best performing co-doped sample S/N-Fe_{27} Rotating disk electrode (RDE) measurements of S/N_Fe_{27} catalyst in 0.1 M KOH (solid black), in 0.1 M $HClO_4$ (solid red), Pt/C in alkaline (dashed black) and Pt/C in acid (dashed red).

The ORR activities of the corresponding co-doped catalysts in the acid electrolyte represent the same trend as that was observed for alkaline but lower mass activities to that of KOH medium (see Figure 66).

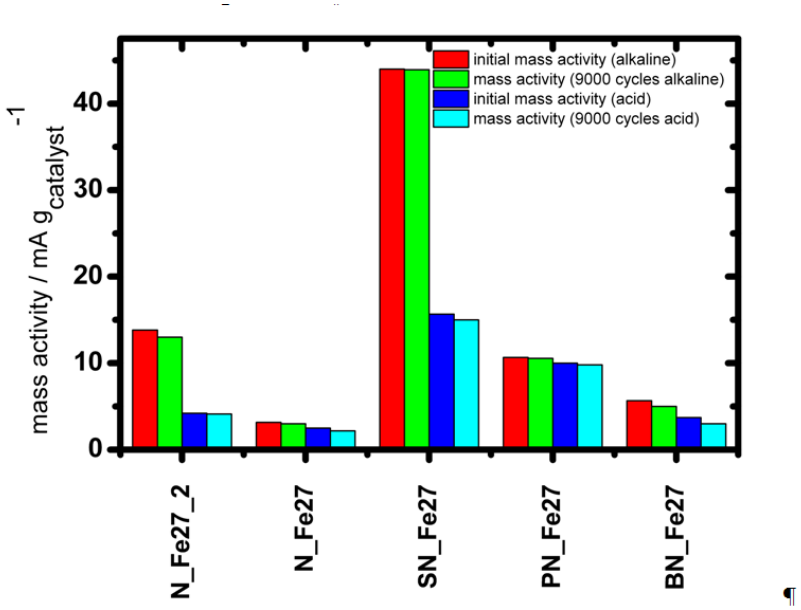

Figure 66. ORR mass activities at 0.8 V vs. RHE before and after stability tests 9000 cycles from 0.5 to 1.2 V vs. RHE in 0.1 M KOH compared with 0.1 M $HClO_4$.

To appraise the long term stabilities of the synthesized materials in alkaline and acid media, the initial mass activities of the catalysts (after 20 cleaning cycles) and final mass activities after the stability test (9000 CV between 0.5 to 1.2 V vs. RHE) were measured and plotted in Figure 66. At first sight, mass activity loss is more dominant after 4500 cycles and thereafter remains mostly unchanged. The activity drop is more pronounced in N-doped samples than co-doped systems. Additionally, the stability decreases after the cycling is more pronounced by increasing the metal content from 5 to 27 wt% in alkaline electrolyte. The mass activity drop is higher in acid than in alkaline, although the co-doping has a positive effect on stability of the catalysts in both mediums, as the N_Fe_{27} shows larger activity loss compared to that of X/N_Fe_{27} (X=S, P, B) samples

As a complementary assessment for the practical applications of the as-synthesized IL-derived catalysts, methanol resistance of the S/N_Fe_{27} sample in the alkaline medium was tested and compared with the reference catalyst. As it is shown in Figure 67, the chronoamperometry plot for Pt/C depicts a high turbulence in the current originating from methanol oxidation (positive current).

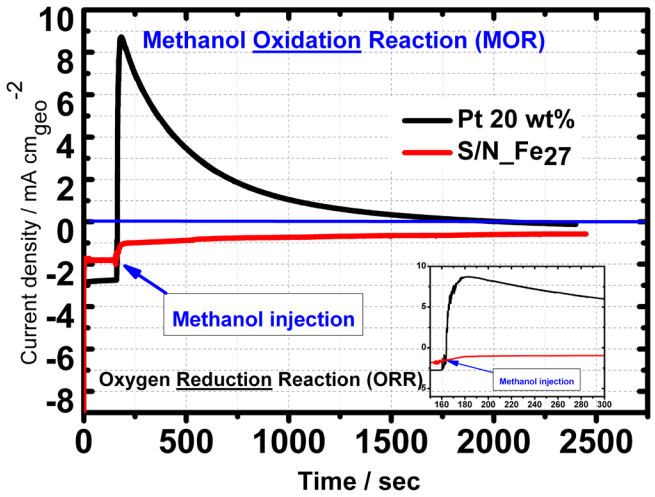

Figure 67. Chronoamperometry response with 10 % (w/w) methanol injected 150 s after starting the measurement in 0.1 M KOH.

Contrary, S/N_Fe_{27} functionalized Ketjen is thoroughly tolerant to the methanol oxidation as the reduction current in chronoamperometry remained relatively unchanged and the current recovered to the initial value after few seconds.

The above-performed RDE measurements in alkaline and acid medium showed that : :i) expectedly, the as-synthesized catalysts show higher activity in alkaline than in acid

electrolyte, ii) For each doped system, the metal-containing sample shows a drastically higher activity regarding the onset potential, diffusion current and mass activity in both electrolytes; iii) S/N_Fe_{27} functionalized Ketjen with E_{onset}=0.9 V vs. RHE exceeds the onset potential of Pt/C reference (0.88 V vs. RHE) in 0.1 M KOH electrolyte, also in acid the onset potential depicts only 0.04 V negative shifts from the reference. vi) the further acid leaching and pyrolysis steps doubled the mass activity for all the N-doped materials independent of their nominal iron content.

The mass activities rang broadly between 0.22 and 44 mA $g_{catalyst}^{-1}$ for N-metalfree and S/N_Fe_{27} samples, respectively. The mass activities of the metal containing (27 wt%) of single N-doped and co-doped samples scope between ~6 and 44 mA g^{1} with the following trend (B/N_Fe_{27}< N_Fe_{27}< P/N_Fe_{27}<S/N_Fe_{27}). Mass activities of N-doped samples increase by increasing the iron content from 5 wt% to 27 wt%. It can be concluded that S/N-co-doped catalyst show the highest onset potential and mass activity in alkaline and acid electrolytes.

We tried to correlate the observed activities with the structure and composition of the synthesized materials. At the first glance, the presence of metal which is mirrored in XRD patterns by the formation of iron carbide guided us to attribute the increase in the activity of metal containing samples to this crystalline phase. But observing the P/N_Fe_{27} XRD pattern without fingerprint reflexes for any crystalline structure reopen the question of the active material for ORR in as-synthesized catalysts. Based on two facts we cannot ignore this observation: i) the activity of P/N_Fe_{27} showed.0.25 V improvement in onset potential compared to P/N_metalfree sample which is in the same range observed for improvement by adding the metal for other (co)doped-samples; ii) the activity of P/N_Fe_{27} sample is close to N_Fe_{27} and B/N_Fe_{27} samples which contain the iron carbide phase. More likely, the presence of P prevents the formation of carbide, meaning the affinity of iron for bonding to phosphorous is dominant to its connection tendency to carbon. In summary, there are two possible explanations for the active material in X/N_Fe_{27} systems: i) iron carbide which is reported in several works as the active phase for ORR is not functioning the same in these material and has no role in defining the activity; or ii) the active moieties in P/N_Fe_{27} is completely different from other samples. Unfortunately, we did not detect any iron in XPS, otherwise we could draw clearer picture of the iron environment in the samples. One can conclude that

metal containing samples show better ORR activity due to the different active material formed in the presence of metal, which is not necessarily iron carbide.

Correlation of the BET and heteroatom content extracted from elemental analysis (EA) with ORR mass activity are illustrated in Figure 68. As it can be seen, mass activities change for different samples regarding their BET surface areas. Apparently, the samples show high activities have high BET surface areas (> 1000 m^2 $g_{catalyst}$).

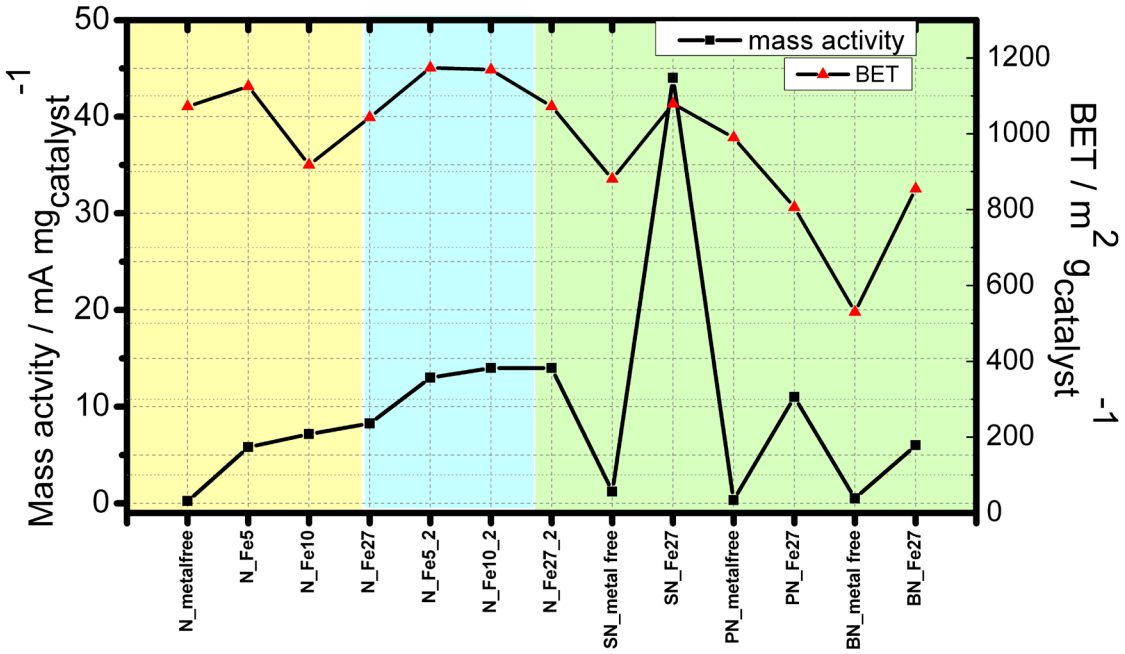

Figure 68. Course of BET surface area of different catalysts correlated to the corresponding mass activity mA g^{-1} (@0.8 V).

Furthermore for each co-doped system, the introduction of metal increases the BET surface area and consequently the mass activity, except for P/N-doped samples. In this case, introduction of metal decreases the surface area while mass activity increase.

The heteroatom type and doping degree are important factors to define the ORR activity. Based on EA and XPS results (see Figure 69) the introduction of metal decrease the doping degree of heteroatoms, however metal presence increases the ORR activity.

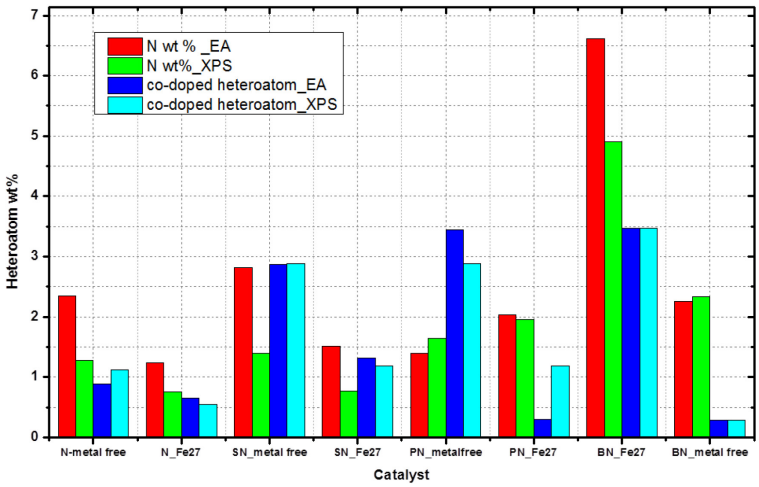

Figure 69. Course of elemental composition (heteroatom) of different catalysts correlated to the corresponding mass activity mA g^{-1} (@0.8 V).

We ascribed the differences seen between the detected heteroatom content (wt%) in EA and XPS to the high surface sensitivity of the XPS technique, while EA is a bulk technique to quantify the elements. The heteroatom contents based on XPS measurement are summarized in Table 12.

Table 12. Composition of different single- and co-doped final catalysts based on elemental combustion analysis (EA) for C, N , S and ICP-OES for P, B, Fe and X-ray photoelectron spectroscopy (XPS); all values given in wt%.

Sample	Elemental analysis (wt%)					
	XPS					
	C1s	N1s	O1s	S2p	P2p	B1s
N	**97.58**	1.28	1.14	-	-	-
N_Fe27	**96.69**	0.75	2.56	-	-	-
S/N	**92.48**	1.4	4.99	1.12		
S/N_Fe27	**95.8**	0.77	95.8	0.55		
B/N	**83.34**	4.91	83.34	-	3.47	
B/N_Fe27	**95.87**	2.34	95.87	-	8.28	
PN	**88.5**	1.64	88.5	-	-	6.97
P/N_Fe27	**92.54**	1.96	92.54	-	-	4.3

Based on the achieved RDE results, we propose that the nature of heteroatom and the presence of metal are the most determining parameters in the final activity of these samples. Interestingly, we observed that in XPS collected data, sulfur is individually doped onto the carbon backbone while B and P are connected with N. Therefore, increasing, the catalytic activity of the S/N-doped catalysts can be attributed to the different charge effect inside the carbon structure. However, the doping degree and crystalline phases observed in the XRD have minor parts.

5.4. Conclusions

We could successfully show that ILs can be used as the precursor for doping of high surface area carbon materials. This synthesis strategy is favored to the direct carbonization of ILs as they are expensive precursors.

It can be summed up that in our catalytic systems the nature of heteroatom and the synergic effect of S, P and B with N are important factors to tune the catalytic activity of the materials toward ORR. Apparently, simultaneous functionalization of carbon with sulfur and nitrogen result in the highest activity in the final materials. Expectedly, introduction of metal is a crucial parameter for determining the ORR electrocatalytic activity while the metalfree doped carbons show low ORR activity. BET surface area and heteroatom content as the determining factors for the active site density are not changing in straightforward trends. Mostly, the samples with higher BET surface area showing lower nitrogen contents which result in a lower active site density. These results show that ORR activity of the forming N-doped material can not only be transferred to other heteroatom types but the final co-doped catalyst shows an improved activity due to synergic effect of binary S/N system compared to single-doped nitrogen compounds. Our material showed a superior activity and stability compared to all the reported heteroatom co-doped material synthesized by the simultaneous introduction of N with B, S or P for oxygen reduction reaction [163, 166-168].These results show that it is promising to coat cheaper materials with thin layers of the IL-derived carbons to enhance their performance for ORR applications. In this way small amounts of ILs could be used for such a process which makes it economical.

6. Activity and Stability of Carbonized Polyformamidine (PFA) for Oxygen Reduction Reaction

6.1. Introduction

In the previous chapters of this thesis, different nitrogen precursors were applied for the N-doping of commercial carbon materials at high temperatures. As an example, in chapter 3 the catalytic activity of pyrolysed polyaniline (PANI) was tested for ORR. Heat treatment of PANI at 900 °C resulted in its carbonization to more or less graphitized nanostructures as observed in TEM micrographs. This carbonized PANI showed a higher overpotential toward ORR compared to that of Pt/C catalyst. By addition of an iron precursor to the synthesis, the activity of the resulting Fe/PANI composite at the same temperature could be improved. Furthermore, impregnation of Fe/PANI mixture on Ketjen support carbon nanoparticles resulted in a composite with even better activity compared to unsupported Fe/PANI. Therefore, carbonized PANI did not show high ORR activity, implying that its supporting on high surface area carbon support was necessary to improve its final activity.

In this chapter, the ORR activity of high surface area N-doped carbon materials derived from the carbonization of an organic polymer, containing formamidine subunits [R-N=(CH)-NH-R] as the key motif (Figure 70), was investigated. Material design and synthesis was performed by Laura Carolina Pardo in the group of Dr. Anna Fischer at the TU Berlin. This cheap and easy to produce polymer with integrated binding sites for metals was previously investigated as support for the synthesis of iron or ruthenium based catalysts for C-C bond formation [152]. However so far, this polymer was never investigated as precursor for the synthesis of N-doped carbons by carbonization nor was the ORR activity of the resulting materials investigated.

6.2. Motivation

In the synthesis, the polyformamidine polymer serves simultaneously as nitrogen and carbon source for the synthesis of N-doped carbon materials. Noteworthy, the polymer synthesis of starting from low cost precursors is facile with relatively high yield resulting in an economical synthetic pathway. Depending of the carbonization temperature and the added iron content prior carbonization, the degree of graphitization and the correlated nitrogen content of the final material could be varied and correlated with the ORR activity. Finally, as in the previous chapters, Ketjen was added to the synthesis and its effect on the ORR activity investigated.

6.3. Results and discussion

The synthesis of polyformamidine (PFA) was performed as reported in literature by Enthaler, Fischer and co-workers [152]. Synthesis parameters including temperatures, temperature treatment duration and gas flow were varied. The material after temperature treatment presents as a shiny highly porous monolith as shown in Figure 70. Thereafter, as for the other materials in this thesis, an acid leaching using 2M sulfuric acid followed by a 2nd pyrolysis step at 900 °C.

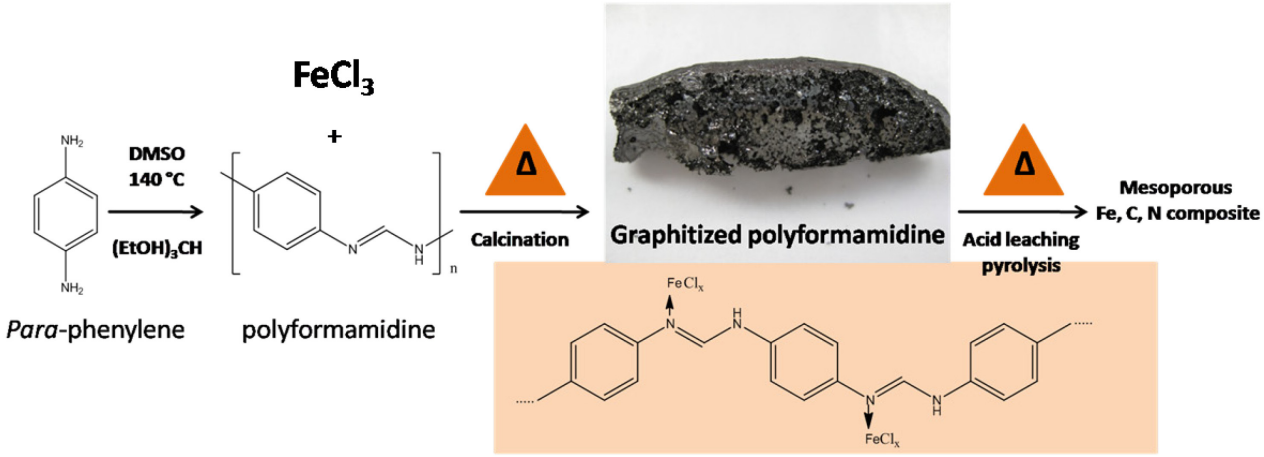

Figure 70. Synthesis of polyformamidine and the following calcination steps yield a foaming graphitized catalyst.

Series of catalysts were synthesized by varying the synthetic parameters, based on the priority including: calcination temperature (from 600°C to 1100°C), calcination duration (from 3 to 12h) and finally iron content (Fe_x-CN, x= 2.5 to 30 Fe wt %). To simplify the optimization, we confined to one variable optimization process. Therefore, for calcination conditions, the nominal metal content was chosen 20 wt% and kept unchanged in all the synthesis. After achieving the best synthesis conditions by RDE evaluation regarding the catalyst performance for ORR, different metal loadings (2.5, 5, 10, 30 Fe wt%) were applied for the synthesis and tested for their performances.

The main focus of this part of thesis is to determine the effect of carbonization temperature and nominal iron content on the ORR electrocatalysis of the final catalysts. Accordingly, powder X-ray diffraction, TEM, elemental analysis (EA) and ICP-OES were applied to characterize the composition and morphology of the materials. Powder XRD patterns of $Fe_{20\%}$-CN materials calcined at different temperatures (600 °C to 1100 °C) are depicted in Figure71. Apparently, calcination temperature has a pronounced effect on the graphitization degree of the carbonized materials. While $Fe_{20\ wt\%}$-CN-600 °C

shows only an extremely broad and weak peak at 2θ ~ 25°, increasing temperature up to 1100 °C, results in higher intensity and sharpness of this diffraction peak (see Figure 71), which shows a higher graphitization within the material. Supposedly, 600 °C is not enough to form graphitic-like structure. XRD reflections between 2θ=35-55 can be attributed to iron carbide, iron nitride and iron. However, cohenite (Fe_3C) is the dominant phase in this material in all the synthesized temperatures.

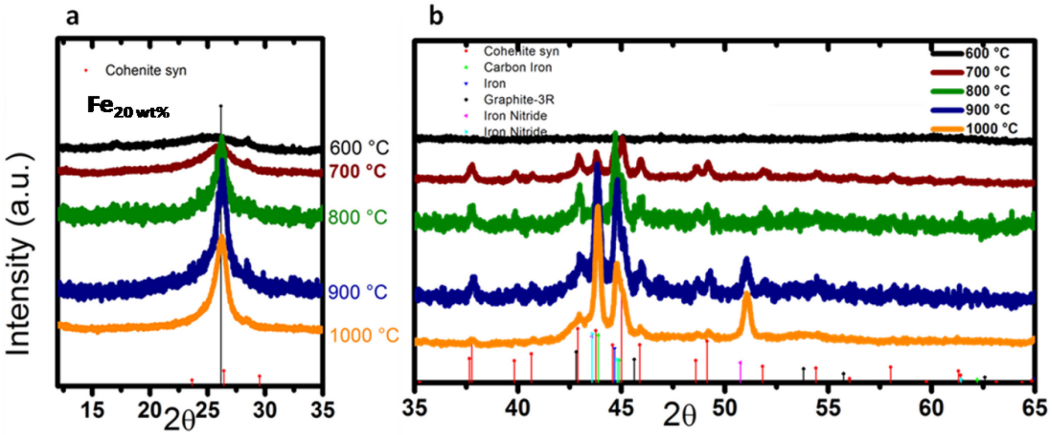

Figure 71. XRD patterns of polyformamidine (PFA)-based catalysts with 20 wt% nominal loading (Fe_{20}-CN) calcined at various temperatures varying from 600-900 °C.

Likewise, the influence of iron content on the catalyst structure was followed by XRD. These results are shown in 72. In this case, all catalysts-containing 5 wt% to 30 wt%- show clearly graphitized peak (at 2θ ~ 25) and iron carbide. This shows that, contrary to the calcination temperature, any metal content is mediating the formation of the same crystalline phase, in particular, iron carbide. Interestingly, after the acid leaching/pyrolysis step, the graphitization degree remained mostly unchanged and the cohenite phase is leached out (see Figure 72)

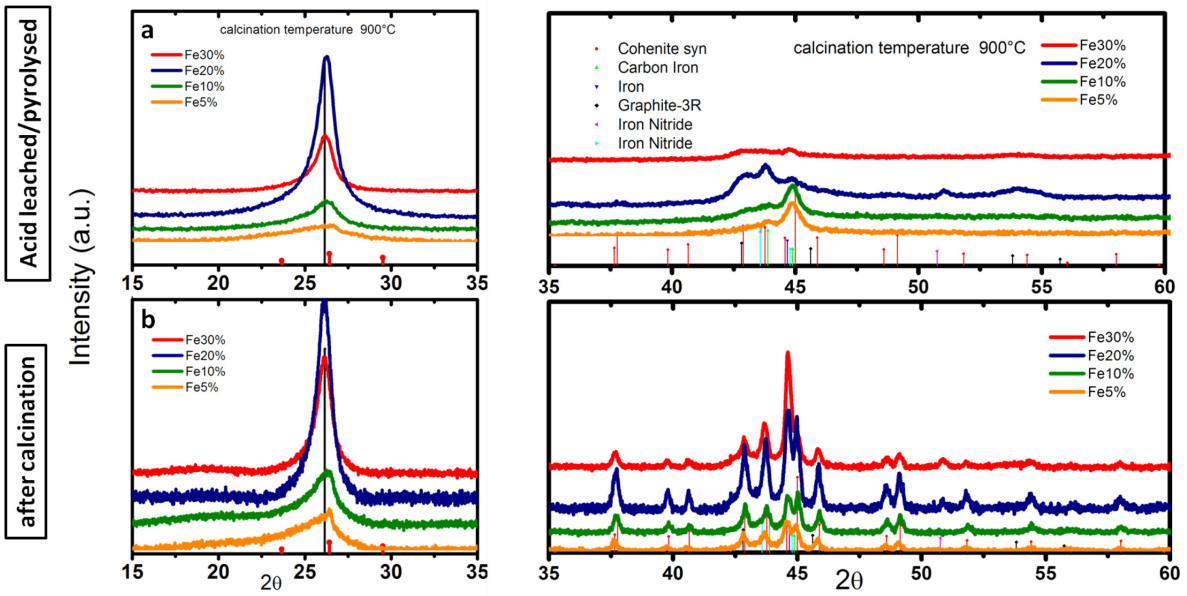

Figure 72. XRD patterns of Fe_x-CN synthesized with various nominal metal contents (x=Fe wt%), directly after calcination (pyrolysis) and after acid leaching.

TEM micrographs are also in agreement with XRD, meaning calcination temperature has a significant influence of the morphology.

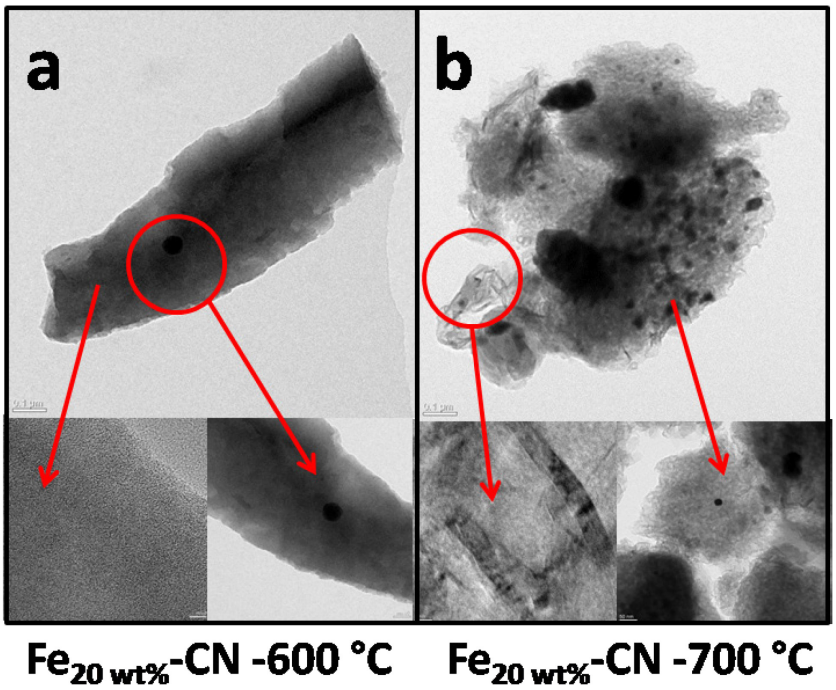

Figure 73. TEM micrographs of catalysts synthesized at a) 600 °C and b) 700 °C.

For two typical samples, calcined at 600 and 700 °C, TEM micrographs are depicted in Figure 73. Obviously, by increasing the temperature, the graphitization in the material is largely enhanced, as can be seen by the development of highly ordered graphitized domains mixed with remnants of amorphous material (see Figure 73).

TEM micrographs of samples calcined at 900 °C directly after the calcination and after the acid leaching step are depicted in Figure A1. As it is illustrated, the leaching step followed by the 2nd pyrolysis at 900 °C result in the removal of iron based moieties to a large extent, as verified by XRD. However, these iron moieties are still detectable inside the catalyst structure.

Electrochemistry characterization. Initially, activity of carbonized polymer (PFA-900°C) was evaluated for ORR and compared to commercial Pt/C catalyst in 0.1 M KOH (see Figure 29, red curve). PFA-900°C, as other N doped carbons, has a limited but existing intrinsic activity for ORR. The onset potential in the presence of oxygen of PFA-900°C showing an overpotential of 0.2 V relative to commercial Pt/C. This result is in line with recent reports for N-doped carbonaceous materials derived from N containing polymers, such as melamine foams [190].

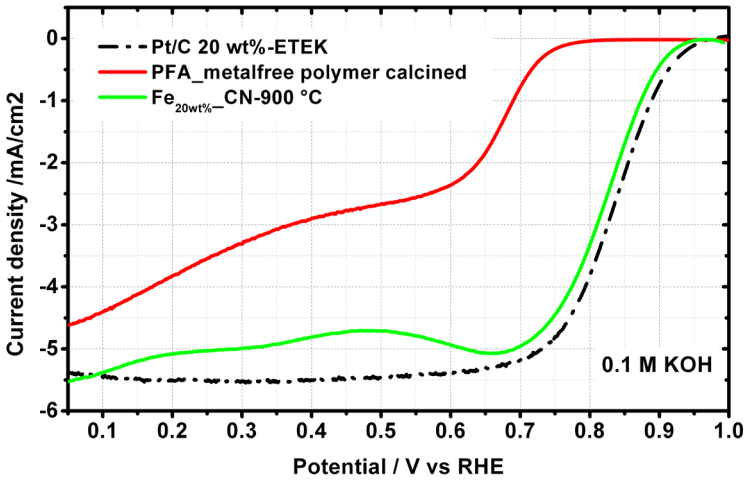

Figure 74. Influence of metal on ORR activity of polyformamidine. RDE Polarization curves of PFA-900°C (red curve), Fe20%-CN-900° (green curve) and commercial Pt/C catalyst (dotted black curve) measured at 1500 rpm in O_2 saturated 0.1 M KOH (pH 13) electrolyte at room temperature. The catalyst loading on the electrode was 0.8 mg cm^{-2}.

In order to improve the electrocatalytic performance of the polymer derived ORR catalyst, $FeCl_3$ (20 wt% to start) was added to the synthesis, i.e. impregnated onto the polyformamidine network prior pyrolysis (for more details see appendix) and acid leaching and a second pyrolysis.

As depicted in Figure 74, the resulting material Fe20%-CN-900° shows a pronounced positive shift of onset potential (0.18 V) compared to that of metalfree polymer calcined at the same temperature. In addition, the diffusion-limiting current regime is better developed when iron chloride was added to the synthesis. In order to investigate the effect of calcination temperature on the catalysts activity, materials with a nominal $FeCl_3$ content of 20 wt% and calcined at different temperatures (from 600°C to 1100°C) were investigates by RDE. The corresponding linear sweep voltammogramms (LSVs) are depicted in Figure 75. It can be seen that calcination temperature has a pronounced effect on onset potential. Increasing the temperature from 600 to 900 °C, improves the onset potential from 0.69 to 0.86 V vs. RHE. In contrast, further temperature increase from 900 to 1100 °C inversely decreases the onset potential to 0.72 V vs. RHE. Not only the onset potential but also the diffusion regime and the half-wave potential $E_{1/2}$ are influenced by the calcinations temperature of the pre-catalyst. With the exception of the material calcined at 1100°C, calcination at higher temperature improves the diffusion.

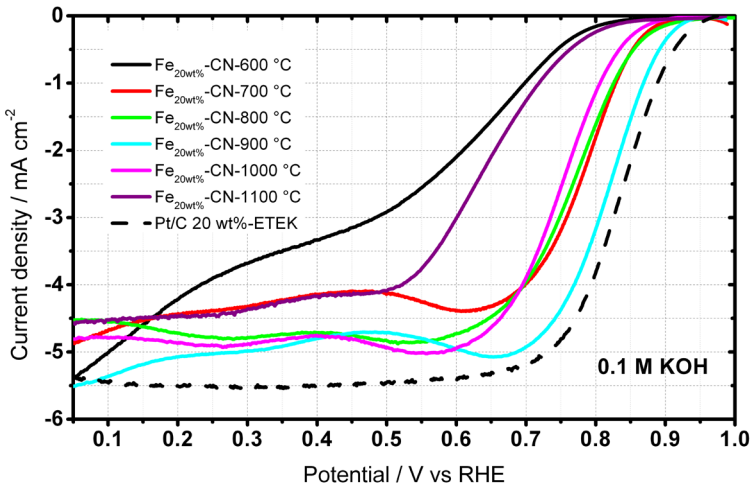

Figure 75. Effect of calcination temperature in ORR activity of different PFA derived catalysts with 20 wt% nominal $FeCl_3$ content. RDE Polarization curves at 1500 rpm in O_2 saturated 0.1 M KOH (pH 13) electrolyte at room temperature. Catalyst loading on the electrode was 0.8 mg cm^{-2}.

The influence of other synthesis parameters on the ORR activity such as calcination time and gas flow rates were also exemplifying studied for a nominal iron chloride loading of 20 wt% and a calcination temperature of 900°C. Therefore, calcination times of 12, 6 and 2 hours were applied for the synthesis of $Fe_{20wt\%}$-CN-900°C materials, as well as nitrogen gas flows of 60 and 300 ml/min. In Figure 76(a), the ORR activity of these materials, after acid leaching and 2nd pyrolysis, are compared.

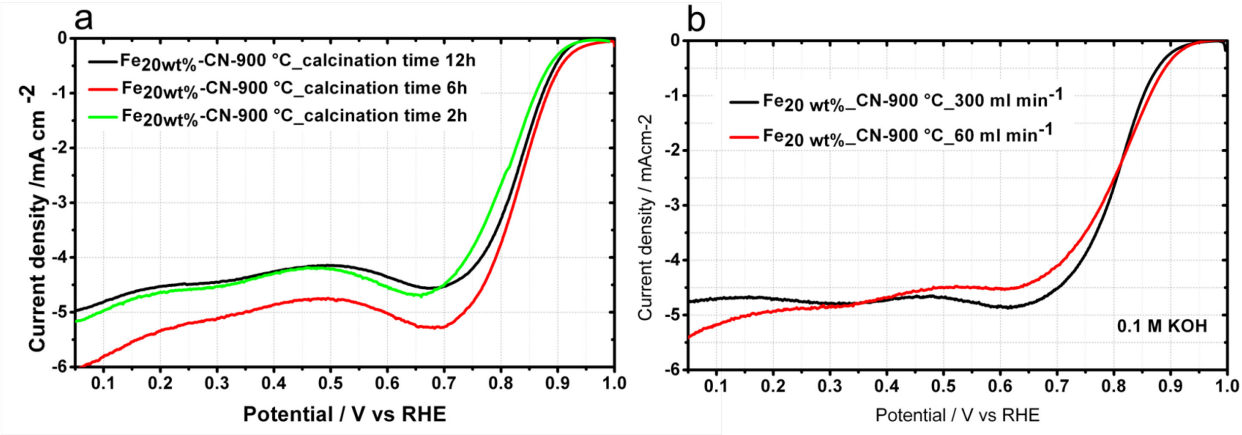

Figure 76. RDE Polarization curves at 1500 rpm, O_2 saturated 0.1 M KOH (pH 13) electrolyte at room temperature, catalyst loading = 0.8 mg cm^{-2}. a) effect of calcination time, b) effect of N_2 flow 300 ml min^{-1} (black curve) and 60 ml min^{-1} (red curve) during the synthesis.

Apparently, the calcination time has no drastic effect on the activity of the resulting materials, as revealed by the similar onset potentials. Similarly, the nitrogen gas flow rate during the synthesis does not play a major role in the final activity of the catalyst.

By choosing 900 °C, 12 hours and 60 ml min^{-1} N_2 flow as optimized calcination parameters, further PFA derived catalysts with different iron chloride loadings ranging from 2.5 to 30 wt% were synthesized to investigate the effect of iron loading on the ORR activity (see Figure 77). RDE measurements show that decreasing the iron content from 30 to 2.5 wt% shifts the onset potential from 0.87 to 0.92 V vs. RHE. It has to be noted, that in all cases, even for low iron loadings, the onset potential (E_{onset} > 0.87 V vs. RHE) is always largely improved compared to the metalfree PFA derived catalysts calclined under equal conditions (E_{onset} = 0.8). Interestingly, the catalysts with iron contents smaller than 10 wt% display all a very similar activity, which more importantly is higher than that of commercial Pt/C catalysts (improvement in onset potential of ~ 0.05 V). It is noteworthy to mention that there is not a meaningful difference in activity between $Fe_{5\ wt\%}$-CN and $Fe_{2.5\ wt\%}$-CN regarding

their very close E_{onset}. The same trend is observed for the $E_{1/2}$, i.e. a positive shift is observed with decrease in metal content.

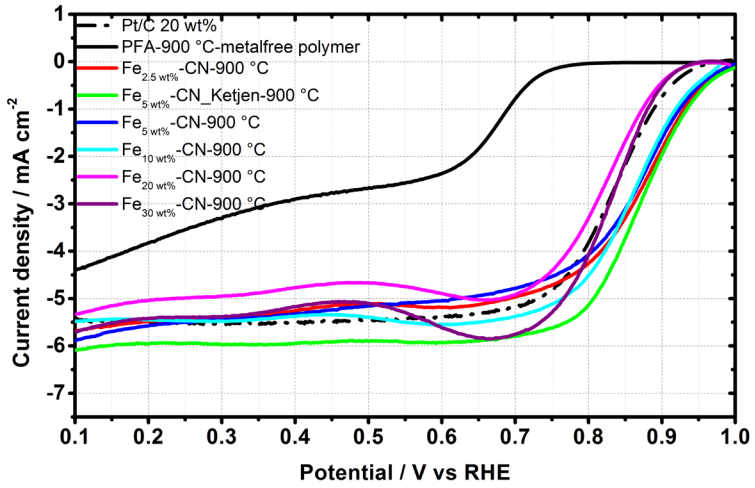

Figure 77. Effect of metal content in ORR activity of different PFA derived catalysts pyrolysed at 900 °C. RDE Polarization curves at 1500 rpm in O_2 saturated 0.1 M KOH (pH 13) electrolyte at room temperature. Catalyst loading on the electrode was 0.8 mg cm^{-2}.

Finally with the hope of achieving improved performance, especially in the diffusive part, a commercial high surface area carbon support (Ketjen) was added to the polymer prior iron chloride impregnation and calcination. The results show that addition of Ketjen did not have any compelling effect on the kinetic regime of the catalysts but, as hoped, slightly improved the diffusion regime, as evidenced by a plateau shaped limiting current (see Figure 78).

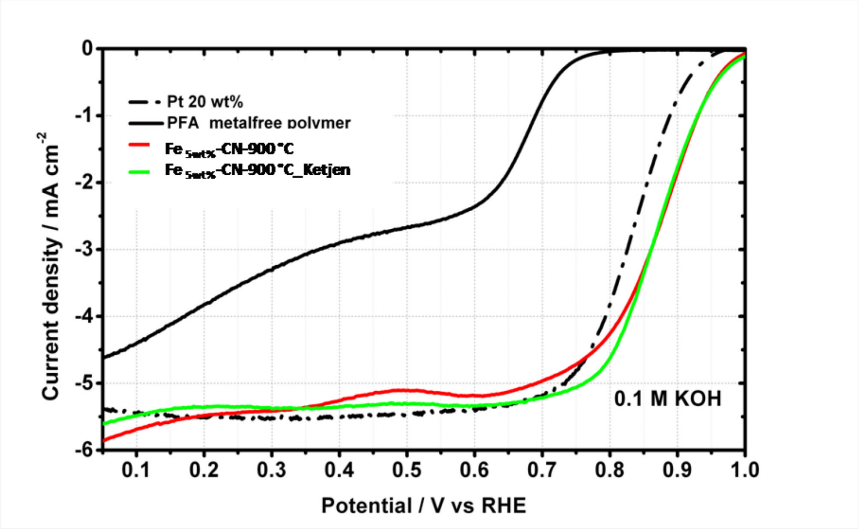

Figure 78. Effect addition of Ketjen nanoparticle during catalyst synthesis on ORR activity of $Fe_{5wt\%}$-CN-900 °C. RDE Polarization curves at 1500 rpm, O_2 saturated 0.1 M KOH (pH 13) electrolyte at room temperature, catalyst loading = 0.8 mg cm^{-2}.

Table 13 summarizes all the RDE data regarding, E_{0nset}, $E_{1/2}$ and mass activity in 0.1 M KOH.

Table 13.electrochemical results regarding E_{onset}, $E_{1/2}$ and mass activity of different catalysts in alkaline.

Catalyst	E_{onset} (V vs. RHE)	$E_{1/2}$ (V vs. RHE)	I_m (mA $mg_{catalyst}^{-1}$)
$Fe_{20\%}$CN_ 600°C	0.7	-	-
$Fe_{20\%}$CN_ 700°C	0.83	0.79	6.68
$Fe_{20\%}$CN_ 800°C	0.83	0.77	3.15
$Fe_{20\%}$CN_ 900°C	0.86	0.80	6.58
$Fe_{20\%}$CN_ 1000°C	0.8	0.75	1.85
$Fe_{20\%}$CN_ 1100°C	0.72	0.65	0.31
$Fe_{2.5\%}$CN_ 900°C	0.92	0.84	22.63
$Fe_{2.5\%}$CN_ 900°C-Ketjen	0.93	0.87	38
$Fe_{5\%}$CN_ 900°C	0.91	0.86	22.20
$Fe_{10\%}$CN_ 900°C	0.92	0.87	44.58
$Fe_{20\%}$CN_ 900°C	0.86	0.82	6.60
$Fe_{30\%}$CN_ 900°C	0.88	0.84	20.02

The ORR activity of the best performing catalyst in alkaline i.e. $Fe_{2.5\ wt\%}$-CN-900 °C_Ketjen, was as well examined in acid electrolyte (see Figure 79). In line with literature reports, the $Fe_{2.5\ wt\%}$-CN-900

°C catalyst exhibits lower onset potential in 0.1 M $HClO_4$ than in 0.1. M KOH with overpotential of 0.06 V compared to Pt/C. Besides, $E_{1/2}$ is also negatively shifted, confirming the lower catalytic performance of the catalyst in acid compared to alkaline electrolyte.

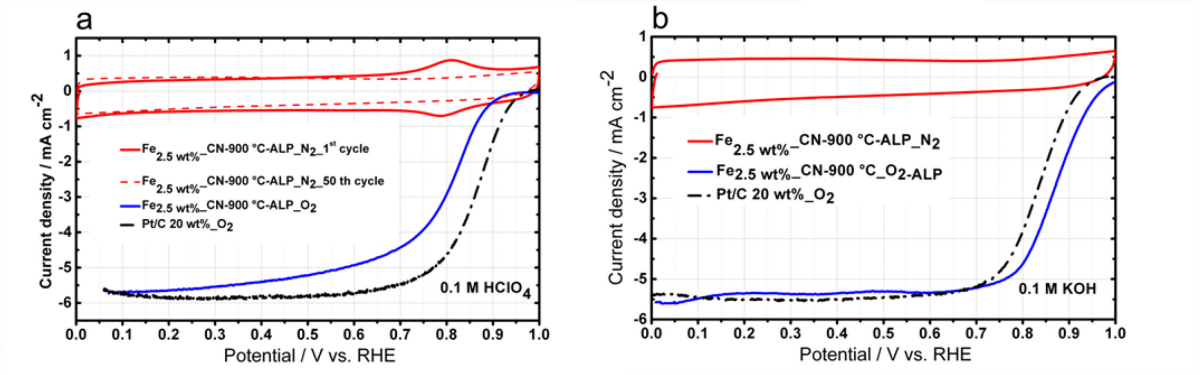

Figure 79. ORR activity of the best performing catalyst, $Fe_{2.5wt\%}$-CN-900 °C. RDE Polarization curves. A) ORR activity in 0.1 M $HClO_4$ (pH 1) dashed red line, CV after 50 cycles and b) ORR activity in 0.1 M KOH (pH 13). Conditions: 1500 rpm, room temperature in O_2-saturated electrolytes, NNMC loading = 0.8 mg cm^{-2}.

Cyclic voltammetry (CV) of the $Fe_{5\ wt\%}$-CN-Ketjen in N_2-saturated acid and alkaline electrolytes are illustrated in Figure 79(a) and 79(b), respectively. While the CV in N_2-saturated 0.1 M $HClO_4$ shows a reversible redox peak at 0.82 V vs. RHE (Figure 79(a)), the CV in 0.1 M KOH is featureless. It has to be mentioned that this peak disappears after 50 cycles in N_2-saturated $HClO_4$, most likely due to the removal of iron from the catalyst surface. (see Figure 79(b) red dashed line).

Stability tests were performed in acid and alkaline media for the best performing catalysts. Figure 80 summarizes the results. Obviously, in line with the previous CVs, the catalysts are more stable in alkaline medium. Moreover, increase of the metal content decreases the stability, in particular in acid medium.

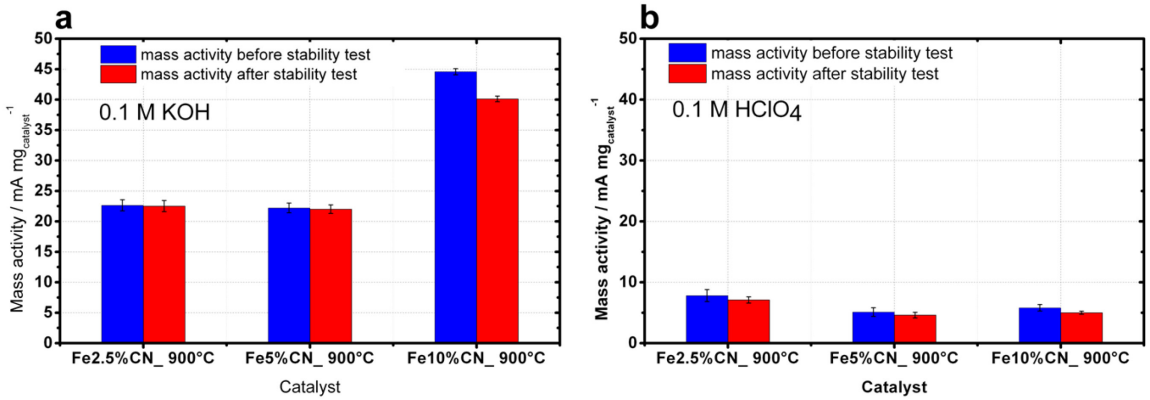

Figure 80. Stability tests of best performing catalysts in a) alkaline, b) acid after 9000 cycles, 50 mV s^{-1}, 0.5-1.2 V vs. RHE.

Methanol tolerance was evaluated in alkaline electrolyte for $Fe_{2.5\ wt\%}$-CN/Ketjen. Contrary to Pt/C. which is pronouncedly affected by methanol oxidation, $Fe_{2.5\ wt\%}$-CN/Ketjen show high tolerance towards methanol (MeOH) injection. From the chronoamperometric results showed in Figure 81, it is obvious that the current related to Pt/C immediately, after the MeOH injection, shifts to positive current with a sharp slope due to methanol oxidation. This positive value is retained even after few seconds. In contrast for $Fe_{5\ wt\%}$-CN, not only does the current remain negative (reduction current) but also it does recover extremely rapidly within 10 s with only minor turbulences.

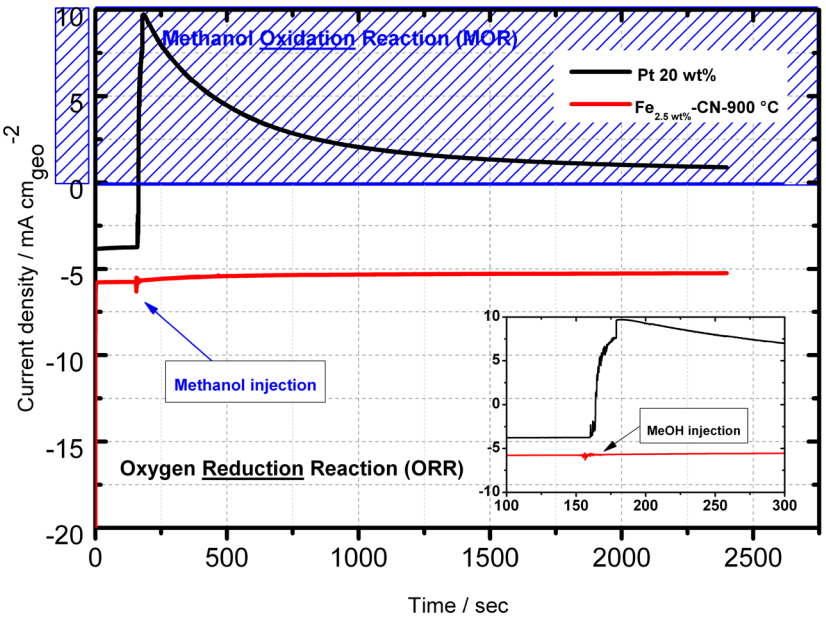

Figure 81. Chronoamperometry of $Fe_{5wt\%}$-CN-900 °C_Ketjen after injection of methanol.

Our RDE measurements show that calcination temperature and nominal metal contents are the crucial parameters regulating the activity of the final catalysts, while the calcination time and gas flow during calcinations have no drastic effect. Noteworthy, increasing the calcination temperature from 600 to 900 °C drastically improved the onset potential about 0.16 V. Additionally, tuning the metal content allows to improve the onset potential (E_{onset}) of further 0.08 V. Obviously, addition of iron drastically improves the catalytic activity of PFA-derived catalysts, although lower content of iron are preferable to generate the most active catalyst.

The values regarding nitrogen content, BET surface areas and graphitization degree of different catalysts are summarized in Table 14.

Table 14. Summary of material characterization of different samples.

Catalyst	Graphitization degree $1/(\alpha)^{\circ}$ As-synthesized	BET ($m^2\ g^{-1}$) As-synthesized
$Fe_{20\%}CN\_$ 600°C	0.14	-
$Fe_{20\%}CN\_$ 700°C	0.37	251.1
$Fe_{20\%}CN\_$ 800°C	0.917	227,6
$Fe_{20\%}CN\_$ 900°C	1.05	220.9
$Fe_{20\%}CN\_$ 1000°C	0.68	235,7
$Fe_{20\%}CN\_$ 1100°C	0.95	211.7
$Fe2._{5\%}CN\_$ 900°C	0.32	227.6
$Fe_{5\%}CN\_$ 900°C-Ketjen	0.3	96.83
$Fe_{5\%}CN\_$ 900°C	0.4	189.2
$Fe_{10\%}CN\_$ 900°C	0.52	216.9
$Fe_{20\%}CN\_$ 900°C	0.98	224.7
$Fe_{30\%}CN\_$ 900°C	0.95	-

In order to investigate the role of calcination temperature and metal content in the catalytic activity of the final catalysts, the determined E_{onset} values and graphitization degree of the different materials are plotted for various calcination temperatures and metal contents as depicted in Figure 82.

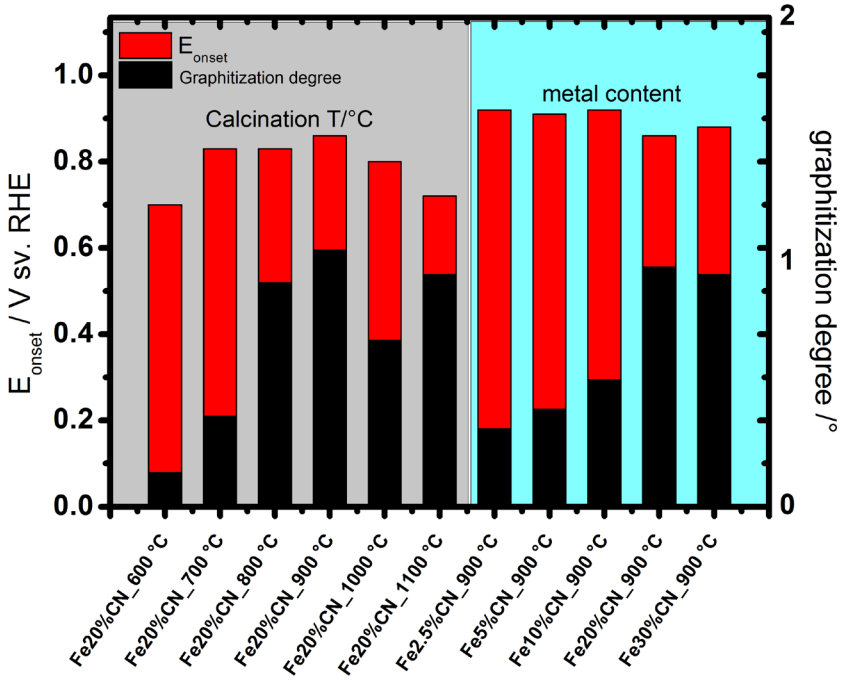

Figure 82. Course of onset potential and graphitization degree of different catalysts.

At first glance, $Fe_{20wt\%}$-CN-600°C and $Fe_{20wt\%}$-CN-700°C suffer from very poor graphitization (α~0.14°), as determined by TEM and XRD. By increasing the temperature to 900°C, α increases to ~ 1, maximum value among all the materials, resulting in the best performing catalyst for a nominal $FeCl_3$ loading of 20 wt%. Surprisingly, Further temperature increase to 1000°C and 1100°C, decreases the graphitization, presumably due to some oxidation at high temperature with ppm level O_2 remnants in the N_2 gas stream. One can conclude that up to 900 °C, graphitization and E_{onset} increase in line with each other while that trend is not given for higher calcination temperatures. Indeed while $Fe_{20\%}$CN_ 1100°C has a higher graphitization than $Fe_{20\%}$CN_ 1000°C, its activity for ORR is lower.

Independent of metal content, all the catalysts synthesized at 900 °C are active by showing close onset potential to 0.85 V vs. RHE. While increasing the metal content from 2.5 to 10 wt%, increases gradually the graphitization, all the samples show relatively close activity. Moreover, raising the metal content to 20 wt% and 30 wt% increases the graphitization but shifts negatively the E_{onset}. It is known that iron catalyzes the graphitization of carbonaceous structures. Based on these results, clearly, both

temperature and metal affect the graphitization i.e. the overall conductivity of the catalysts and therefore its ability to transfer electrons. However, it has to be noted that other present motifs such as iron carbide/nitride presence as well as total nitrogen content and surface area of the materials will strongly affect the final ORR activity. By having a look in Table 14 (Characteristics of the materials) one can see, that the material with the highest ORR activity, in terms of onset potential, was synthesized in the presence of iron, has a relatively low graphitization degree, a high surface area. In other words, the activity of the materials in this synthesis can be tuned along the activity determining parameters i.e. N content, Fe content, conductivity.

For a 4ē ORR reduction at 1500 rpm, a limiting current of ~ 6 mA cm^{-2} is expected. Based on this postulate, the number of electrons exchanged for the catalysts synthesized at 900 °C with Fe contents <10 wt% was evaluated. Those catalysts perform the ORR via a 4ē transfer mechanism. Additionally, $E_{1/2}$ as a transition part from kinetics to diffusion current is not as sharp as Pt/C for these catalysts. This feature can be related to the restricted porosity inside the catalyst film formed on the electrode which limits the mass diffusion of O_2 inside the pores and consequently to the double layer. Obviously applying Ketjen as the support in the synthesis steps can improve the diffusion properties by increasing the diffusion current to ~ 6 mA cm^{-2} with a plateau shape. This feature can be assigned to the well-defined porosity of Ketjen nanoparticles used during synthesis of the catalyst which result in a catalyst with proper diffusion characteristics.

6.4. Conclusion

It is not straightforward to correlate the observed catalytic activity to the composition-structure of the final products. This partially originates from the numerous parameters which can influence the catalyst performance, which mirrors the active site density. From the very initial measurements, to achieve activity for the ORR, presence of a metal (Fe), N and C going through a high temperature heat treatment *ca.* 900 °C is necessitated. Three major synthetic factors are apparently of particular importance for the activity of the catalyst: The calcination temperature, the metal content and the addition of Ketjen. These factors have a multivariable effect on the secondary major factors including (order of importance): the N content, the surface area/porous volume and especially the microporosity created during the heat treatment and the iron content, in terms of either inorganic iron species (iron, iron carbide, iron nitrides) or iron bound in M-N/C species located on the carbonaceous material formed.

In summary, our results show that calcination temperature is the assertive criteria to control the graphitization degree and formation of crystalline structures present in catalyst material as well as determining the nitrogen content and surface area of material. On the other hand, metal content has a dominant effect on graphitic structure and regulates the nitrogen content in the final material. However; mutual effect of these two factors makes it difficult to come to a one-word conclusion.

In summary,

These results show that PFA-derived catalysts synthesized by very cheap starting precursors can be successfully replaced by the expensive macrocyclic catalysts showing ORR activity.

7. Conclusions and Perspectives

In this thesis, the activity and stability of four different groups of carbon-based non noble metal catalysts towards ORR in acidic and alkaline electrolytes were investigated. The nature of metal –iron and manganese- and their synergic effects in bimetallic catalyst systems as well as the influence of nitrogen precursor and carbon source on the catalytic performance were examined. Moreover, the influence of synthesis procedure, pyrolysis conditions, post treatments (acid leaching) were established. All synthesized materials were extensively characterized by different physico-chemical techniques to determine their structure, composition and morphology as well as the chemical environment of the incorporated heteroatoms and metal ions. Consequently, the ORR electrocatalysis of different NNMCs was coordinated with the final material composition/morphology. It was also endeavored to probe the active site of the catalysts to answer the question about the presence of metal in the active centers. ORR activity of all the catalysts was compared with Pt/C reference in alkaline and acid media. This knowledge can be helpful to rationally design of electrocatalysts with improved performance by choosing appropriate precursors and synthesis strategies.

Polyaniline (PANI)-based catalysts. In the first part of this thesis, we addressed the following key questions: i) how does the nature of non noble metal and the synergic effect of metals in a bimetallic catalytic system affect the activity, ii) how does the synthetic routs/steps and composition of the starting precursors can influence the final performances, ii) how can type of carbon support affect the final material and its electrocatalysis, iv) how can the introduction of a second nitrogen source characterize the final catalytic activity and v) are the metal ions part of the active site of NNMCs or not. Our preliminary measurements showed that presence of metal and coating of the nitrogen/metal precursors on support are essential to achieve high catalytic activity of PANI-based catalysts. First, in order to assess the intrinsic activity of the manganese (Mn) catalysts for ORR, different loading of Mn in combination with PANI were impregnated on the Ketjen. The activity of the manganese catalysts were compared to the iron containing materials, as iron formed the best performing NNMCs for ORR [17]. The results show that manganese even in optimum loadings cannot create the catalysts as active as iron NNMCs and Pt/C 20wt% reference. For both monometallic catalysts, we could show that, first, by increasing the metal content from 17 to 27 wt%, the activity increased, but further increase of the nominal metal loading to 37 wt% can negatively decrease the activity. The Fe/PANI/Ketjen synthesized in this work showed a better activity than the-state-of-the-art Fe/PANI/Ketjen [17].

For bimetallic systems, we could show that with an optimized Mn:Fe ratio (1:1) at a nominal metal loading of 27 wt%, we could proceed the ORR activity of iron catalyst and Pt/C 20wt% in alkaline

media. After achieving the best composition and synthesis parameters in alkaline electrolyte, the best performing monometallic ($Fe_{27wt\%}$/PANI/Ketjen and $Mn_{27wt\%}$/PANI/Ketjen) and bimetallic (Mn:Fe=1:1 (metal=27wt%)/PANI/Ketjen) materials were tested in acidic electrolyte. The results showed that Fe and Mn:Fe=1:1 catalysts (27 wt% loadings) show the similar activity which is better than the-state-of-the-art material measured in acid, however the activity is still slightly lower than Pt/C 20wt% reference. Monometallic manganese catalyst showed a low catalytic activity in acid. Furthermore, the most active catalysts showed high stability in alkaline medium with no change in the mass activity after cycling stability test. However, in acid, they represented lower stability to that of in alkaline. Interestingly, bimetallic Mn:Fe=1:1 catalyst showed better stability compared to the monometallic iron catalyst in both media. This showed that the synergic effect of iron and manganese could influence the stability of the catalysts.

We could show that during the synthesis procedure, the acid leaching and a subsequent high temperature pyrolysis is the determining step to achieve a highly active electrocatalysts. These treatments are expected to recover the fresh surface of the catalysts and thus more active sites are free for ORR. Additionally, Ketjen-supported catalysts represented better performance than graphene oxide and carbon nanotubes-supported catalysts with the same composition, implying that the graphitization degree in the carbon support is important.

To address the key question of presence of metal in the active site, we used carbon monoxide (CO) as a probe molecule to examine the active sites. We could show that in the absence of metal, there is no interaction between the catalyst and CO. Interestingly, in the presence of metal, CO is adsorbed on the catalyst surface and the adsorption can be correlated to the catalytic activity, however we cannot determine the number of CO adsorbed on each active site. One conclusion could be that CO is adsorbed on the active sites which include the metal coordinated with number of nitrogen atoms.

All the catalysts were characterized by different techniques to study their morphology and composition. It has to be mentioned that there is no clear correlation between the electrocatalytic activity, BET surface area and nitrogen/metal content of different materials. However, the most active materials consists of a composite nanostructure composed of the carbon support and a graphene-like structure. The latter structure was created during the pyrolysis of PANI. These catalysts showed relatively high nitrogen content. The BET surface area decreased compared to the support; XRD patterns of the final catalysts did not show any crystalline structure except the graphitic structure of the support.

In conclusion, we could successfully create bimetallic manganese and iron catalyst which showed a better performance compared to the iron state-of-the-art and Pt/C reference catalysts in alkaline

medium while its performance is comparable with them in acid medium. However, the decisive factor for the electrocatalytic activity of Me/PANI/Ketjen materials remains unraveled and further investigations are necessary to unravel the structure and composition of the active site.

Hexamethyltetramine-based catalysts. In the second part of this work, hexamethyltetramine (HMTA) was used as the nitrogen precursor in combination with iron and Ketjen as metal and carbon support, respectively. Additionally, the wet impregnation synthesis strategy that had been used in other parts of this work was replaced by ball milling (BM) strategy. This part of the thesis focused on the application of a new nitrogen precursor with high N/C ratio and its influence on the final nitrogen content and the subsequent activity, as well as the influence of BM on the morphology of the final materials and their activity. Our results showed that applying a nitrogen-rich precursor resulted in relatively high nitrogen level in final materials; however it is in the range of the PANI-based catalysts. Noteworthy, using BM as a mixing strategy could drastically alter the morphology of the starting Ketjen nanoparticles to the final mesoporous-like structure. This morphology was largely influenced by the ball milling time, as there is an optimum 500 minutes BM necessary to achieve homogenous 3D-mesoporous morphology. Additionally, elemental mapping for nitrogen (N) showed that BM could result in a homogenous N-doping compared to the wet-impregnation strategy used in PANI-based catalysts. These catalysts showed an extraordinary catalytic activity for the metalfree samples which was not previously seen for other catalysts [163, 166-168]. Furthermore, creation of mesoporous-like structure could improve the mass transport inside the catalyst film which was mirrored in the diffusion regime of the RDE measurements. The cycling stability tests for the catalysts showed high stability in alkaline; however the catalysts stability in acid medium is lower. XRD patterns of these catalysts showed iron carbide crystalline phase as the dominant final structure. For all the metalfree or metal containing samples, the recorded linear sweep voltammetry shape regarding the very positive half wave potential confirmed the influence of morphology on final ORR electrocatalysis. BET surface area of these catalysts decreased compared to that of Ketjenblack; however it is in the same range of other materials investigated in this thesis. It has to be mentioned that BM could reduce the synthesis time and enabled us for up-scaling. In conclusion, the ORR catalytic activity measured for ball-milled samples was exceptionally high for metalfree catalysts compared to the previously reported state-of-the-art materials as well as metalfree sample reported in other parts of this thesis. Similarly, the metal containing samples represented a high catalytic activity in both acid and alkaline medium which is superior to previously reported catalysts synthesized by ball milling strategy [163, 166-168].

Ionic liquid-based catalysts. In the third part of this thesis, ionic liquids as the heteroatom precursors with flexible compositions were used for doping of commercial Ketjen. In this part, the key question was how the nature of the heteroatom could influence on the final catalytic activity. Here, single-doped nitrogen catalysts and co-doped S/N, P/N and B/N materials were synthesized. The ORR activity of co-doped materials as metalfree and metal containing samples were compared with N-doped Ketjen catalyst and Pt/C reference. Our results showed that S/N_$Fe_{27wt\%}$ catalyst represented the highest activity which was superior to the Pt/C reference in alkaline medium. Expectedly, the activity in acid medium is lower than Pt/C, but still is high compared to the state-of-the-art materials for NNMCs. Other co-doped materials, B/N_$Fe_{27wt\%}$ and P/N_$Fe_{27wt\%}$ showed similar activity to that of single-doped N_$Fe_{27wt\%}$ which is inferior to Pt/C catalyst even in alkaline medium. Similar to other catalysts in this thesis, the activity remained relatively unchanged after stability test in alkaline medium while in acid electrolyte, the activity decreased. For all the mono- and bimetallic systems, the presence of iron is necessary to achieve high activity. Our characterizations showed that the morphology of the heteroatom-doped final catalysts were similar to the starting Ketjen support. Heteroatom doping degree is lower than that was observed for PANI and HMTA in the previous parts. XRD patterns of the final catalysts for metal free samples showed graphitic-like structure of the Ketjen. Addition of iron precursor formed iron carbide in all the samples, except for P/N_$Fe_{27wt\%}$ which showed the identical structure as metalfree samples. BET surface area of these catalysts decreased compared to the starting support and is in the same range as other catalysts in this thesis. Compared to the state-of-the-art reported heteroatom-doped materials, our catalysts showed superior activity both in alkaline and acid medium. In conclusion, our results confirmed that ORR activity of N-doped materials can be successfully transferred to other heteroatoms, in particular S/N_$Fe_{27wt\%}$ co-doped catalysts.

Polyformamidine-based catalysts. The last part of this thesis addressed the ORR activity of unsupported carbonized polyformamidine. The focus of this part was ORR investigation of a NNMC resulted from direct carbonization of a polymer which is simultaneously served as nitrogen and carbon sources. The influence of calcination temperature /time and iron loading on the polymer showed that 900 °C is the optimum temperature while calcination time had no significant influence on the final activity; also, decreasing the metal content from 30 wt% to 2.5 wt% increased the activity. We could show that supporting of the polymer on commercial carbon Ketjen had not improved the final activity. These catalysts showed high stability in alkaline; however the activity decreased to a higher degree in acid medium. As these catalysts resulted from the direct carbonization of polymer at high

temperatures, therefore the catalyst morphology and composition is significantly affected by the calcination conditions. The nitrogen content of the final materials was relatively low compared to that of PANI and HMTA samples. Additionally, the BET surface area was in the range of other catalysts reported in this thesis. In conclusion, the activity of polyformamidine-based catalysts is in an acceptable range for N-doped ORR electrocatalysts, in particular in alkaline medium.

Based on the present results, we could show that NNMCs for ORR are material-based catalysts which their activity is significantly influenced by starting precursor types and synthesis strategies.

Perspectives. The future perspectives and challenges for future improved PEMFC electrocatalysts are

- The application of mesoporous high surface area carbon with the aim of increasing the active site density.
- The combination of two different support materials to investigate their synergic effects. For example, high surface area carbon with high graphitized support.
- The application of ball milling strategy under controlled conditions. For example, under nitrogen or ammonia atmosphere and/or temperature control.
- The designing of different NNMCs by using new nitrogen or other heteroatom sources.
- The investigation of the present catalysts for other chemical reactions, for example oxygen evolution reaction (OER) or water splitting.
- Performing fuel cell measurements in real measurement conditions to investigate the catalyst activity/stability.

8. List of Figures

Figure 1. Individual work packages of this thesis 8

Figure 2. Schematic of a) acidic, b) alkaline PEFCs and corresponding anodic/cathodic reactions 11

Figure 3. Volcano plot for ORR electrocatalysis of various metal phthalocyanines 15

Figure 4. Schematic overview on possible nitrogen bonding sites on a carbon backbone 18

Figure 5. Schematic illustration of the double-layer structure during ORR in acid (left) and alkaline (right) conditions. Insets (a) inner-sphere and (b) outer-sphere electron transfer processes 21

Figure 6. Tube furnace setup and samples in ceramic crucible with cover 25

Figure 7. Schematic of the synthesis procedure for non noble metal catalysts NNMCs) 25

Figure 8. Ball miller setup and sample holder with stainless balls 26

Figure 9. Polishing machine used in preparation of the electrode 31

Figure 10. Rotating disk electrode (RDE) setup, a) overall view of RDE, b and c) details of the electrochemical cell and electrodes, c) glassy rotating disk electrode (RDE), d) rotating ring disk electrode (RRDE) 32

Figure 11. a) Pulse chemisorption and TPD instrument. b) Schematic of reactor: 1) gas inlet/outlet, 2) sample holder cap, 3) thermocouple, 4) internal bulb, 5) external bulb, 6) glass wool, 7) sample 39

Figure 12. TGA profile of $Fe_{27wt\%}$/PANI/Ketjen in N_2 from 0 to 800 °C (5 °C min^{-1}) 42

Figure 13. TGA profiles of a) monometallic Mn and Fe catalysts with different metal loadings, b) bimetallic Mn:Fe catalysts with 27 wt% metal loading with different M:Fe ratios in N_2 from 0 to 800 °C (5 °C min^{-1}) 43

Figure 14. XRD patterns for various control catalysts: as-received commercial Ketjen (black line), Ketjen 4h-pyrolysed at 900 °C (red line), PANI/Ketjen 4h-pyrolysed at 900 °C (blue line) and unsupported PANI 4h-pyrolysed at 900 °C (greenline) 44

Figure 15. XRD patterns for $Fe_{27wt\%}$/PANI/Ketjen catalyst in different synthetic steps compared with Ketjen: a) Ketjen (as-received), b) catalyst precursors before pyrolysis, c) after 1st pyrolysis but before acid leaching, d) after acid leaching and 2nd pyrolysis 45

Figure 16. XRD patterns for $Mn_{27wt\%}$/PANI/Ketjen catalyst in different synthetic steps compared with Ketjen: a) Ketjen (as-received), b) catalyst precursors before pyrolysis, c) after 1st pyrolysis but before acid leaching, d) after acid leaching and 2nd pyrolysis 46

Figure 17. XRD patterns for bimetallic Mn:$Fe_{27wt\%}$1:1/PANI/Ketjen catalyst in different synthetic steps compared with Ketjen: a) Ketjen (as-received), b) catalyst precursors before pyrolysis, c) after 1st pyrolysis but before acid leaching, d) after 1st acid leaching and 2nd pyrolysis, e) after 2nd acid leaching and 3rd pyrolysis 47

Figure 18. WDX-based elemental mapping of Mn:$Fe_{27\ wt\%}$=1:1/PANI/Ketjen at 7 kV 49

Figure 19. N1s core level of representative catalysts, a) $Fe_{27wt\%}$/PANI/Ketjen, b) Mn:$Fe_{27wt\%}$=1:1/PANI/Ketjen 50

Figure 20. TEM micrographs of polyaniline (PANI) after *in situ* polymerization in the presence of oxidant (APS) 51

Figure 21. TEM micrographs of a) PANI, b) unsupported PANI/Fe pyrolysed at 900 °C/4h 51

Figure 22. TEM micrographs of composite PANI/Ketjen control catalyst pyrolysed at 900 °C (4 hour) 51

Figure 23. TEM micrographs of $Fe_{27wt\%}$/PANI/Ketjen in different synthesis steps: a-b) after 1st pyrolysis, composite structure of catalyst, c) metal-based particles hosted inside the catalyst composite of graphene and Ketjen, d) electron diffraction pattern of the metal-based particles, e-f) the catalyst structure after acid leaching and final pyrolysis steps result in the removal of metal from the catalyst.....52

Figure 24. TEM micrographs of $Fe_{27wt\%}$/PANI/Ketjen after the first pyrolysis and before the leaching step, a) bright field (BF) image and b) dark field (DF) image 53

Figure 25. TEM micrographs of Mn:$Fe_{27wt\%}$=1:1/PANI/Ketjen in different synthesis steps: a-b) after 1st pyrolysis, composite structure of catalyst, c) metal-based particles hosted inside the catalyst composite of graphene and Ketjen, d) electron diffraction pattern of the metal-based particles, e-f) the catalyst structure after acid leaching and final pyrolysis steps result in the removal of metal from the catalyst 54

Figure 26. BET surface area of different catalysts compared with Ketjen a) after the 1st acid leaching and 2nd pyrolysis, b) after 2nd leaching and 3rd pyrolysis 55

Figure 27. Electrocatalytic oxygen reduction of control catalysts. Influence of pyrolysis, addition of metal and support on catalyst onset potential. Conditions: 1500 rpm. O_2-saturated electrolyte of pH 13 at room temperature, catalyst loading 0.8 mg cm^{-2}.....56

Figure 28. Electrocatalytic oxygen reduction of monometallic $Fe_{X\ wt\%}$/PANI/Ketjen (x= metal weight %) with various nominal iron loadings. Conditions: 1500 rpm. O_2-saturated electrolyte of pH 13 at room temperature, catalyst loading 0.8 mg cm^{-2}.....57

Figure 29. Electrocatalytic oxygen reduction of monometallic $Fe_{27\ wt\%}$/PANI/Ketjen (x= 27 wt%) pyrolysed at 500 °C (blue curve(, 700 °C (red curve) and 900 °C (black curve) compared with Pt/C 20wt%. Conditions: 1500 rpm. O_2-saturated electrolyte of pH 13 at room temperature, catalyst loading 0.8 mg cm^{-2} 58

Figure 30. Influence of nominal metal loading (17-37 wt%) on ORR activity of various Me/PANI/Ketjen catalysts. Electrocatalytic oxygen reduction of monometallic a) $Mn_{27\ wt\%}$/PANI/Ketjen (x= 27 wt%) and b) $Fe_{27wt\%}$/PANI/Ketjen pyrolysed at 900 °C with various nominal metal loadings compared to Pt/C 20wt%. Conditions: 1500 rpm. O_2-saturated electrolyte of pH 13, catalyst loading 0.8 mg cm^{-2} 59

Figure 31. Influence of synthesis step in monometallic catalyst on ORR activity Electrocatalytic oxygen reduction of monometallic $Fe_{27\ wt\%}$/PANI/Ketjen (x= 27 wt% metal) pyrolysed at 900 °C. Conditions: 1500 rpm. O_2-saturated electrolyte of pH 13 at room temperature, non noble metal catalyst loading 0.8 mg cm^{-2} 60

Figure 32. ORR activity of the catalysts in alkaline and acid electrolytes. Electrocatalytic oxygen reduction of bimetallic best performing mono- and bimetallic catalysts pyrolysed at 900 °C compared with Pt/C 20 wt% a) in 0.1 M KOH (pH 13), b)in 0.1 M $HClO_4$ (pH 1). Conditions: 1500 rpm. O_2-saturated electrolyte at room temperature, non noble metal catalyst loading 0.8 mg cm^{-2} 61

Figure 33. Influence of nature of support on ORR activity. Electrocatalytic oxygen reduction of $Fe_{27wt\%}$/PANI/Ketjen, best performing mono catalyst- pyrolysed at 900 °C supported on Ketjen (black solid curve), graphene oxide (GO) (red solid curve) and multiwalled carbon nano tubes (MWCNTs) (blue solid curve) compared with Pt/C 20 wt% Conditions: 1500 rpm. O_2-saturated 0.1 M KOH, pH 13, electrolyte at room temperature, non noble metal catalyst loading 0.8 mg cm^{-2} 63

Figure 34. Stability cycling test result of best performing catalysts. Mass activity in a) alkaline and b) acid electrolytes before and after cycling stability tests.....64

Figure 35. Carbon monoxide (CO) pulse chemisorption profile for a) PANI/Ketjen (CN_x metal-free catalyst), b) $Fe_{27wt\%}$ /PANI/Ketjen after 1st acid leaching/2nd pyrolysis, c) $Fe_{27wt\%}$ /PANI/Ketjen after 2nd acid leaching/3rd pyrolysis 65

Figure 36. Correlation of mass activity and CO adsorption. Carbon monoxide (CO) uptake (mmol $g_{catalyst}^{-1}$) based on pulse chemisorption correlated with mass activity (mA $mg_{catalyst}^{-1}$) after 1st acid leaching/2nd pyrolysis in 0.1 M KOH based on RDE measurements 66

Figure 37. Temperature programmed desorption (TPD) spectrum of three different catalysts (a) $Fe_{27\ wt\%}$/PANI/Ketjen; (b) Fe-Mn (metal 27 wt%)/PANI/Ketjen; (c) $Mn_{27\ wt\%}$/PANI/Ketjen 67

Figure 38. A) Synthesis schematic of hexamethyltetramine (HMTA), b) crystalline structure of HMTA provided by powder XRD.....70

Figure39. TEM micrographs of a) $HMTA_2$-C-1, mixed precursor before ball milling, b) $HMTA_2$-C-2, ball-milled precursors for 500 min 71

Figure 40. TEM micrographs of $HMTA_2$–Fe_{40}-C, a) the precursors before ball milling $HMTA_1$–Fe_1-C-1, b) ball-milled sample (500 min), $HMTA_2$–Fe_{40}-C-2, c) after the 1st pyrolysis $HMTA_2$–Fe_{40}-C-3, d) after acid leaching step/2nd pyrolysis, $HMTA_2$–Fe_{40}-C-4.....72

Figure 41. The influence of ball milling time (BMT) on catalyst morphology, TEM micrographs of catalyst $HMTA_2$–Fe_{40}-C, a) before ball milling, b) after 100 min BM, c) 300 BM, d) 500 BM 74

Figure 42. Influence of ball milling (BM) on catalyst morphology. SEM micrographs of a) mixed precursors before ball milling $HMTA_2$–Fe_{40}-C-1, b) ball-milled sample for 500 min $HMTA_2$–Fe_{40}-C-2, c) after 1st heat treatment $HMTA_2$–Fe_{40}-C-3 75

Figure 43. SEM section micrograph of ball-milled precursors (500 min BMT) and after the 1st pyrolysis, $HMTA_2$–Fe_{40}-C-3 76

Figure 44. a) Nitrogen sorption isotherms and b) pore size distributions of the $HMTA_2$-Fe_{40}-C at two synthesis steps, directly after ball milling, $HMTA_2$-Fe_{40}-1 (red) and final catalyst, $HMTA_2$-Fe_{40}-4 (blue) compared to Ketjen (black) 77

Figure 45. Powder X-ray diffraction patterns of representative metalfree and metal containing samples, a) metalfree sample, $HMTA_2$-C and b) metal containing sample $HMTA_2$-Fe_{40}-C, c) the identified reflexes for different species in $HMTA_2$-Fe_{40}-C 81

Figure 46. X-ray photoelectron spectra in the N 1s core level range of selected samples 84

Figure 47. WDX-based elemental mapping for nitrogen measured at 7 kV 86

Figure 48. Effect of BMT (100-500 min) on the polarization curves and onset potentials during the electrochemical oxygen reduction reaction (ORR). A) metalfree sample $HMTA_2$-C-3 and b) metal containing sample $HMTA_2$-Fe_{40}-C-4. Conditions: 1500 rpm, cathodic scan rate of 10 mV s^{-1}, O_2-saturated 0.1 M KOH at room temperature 87

Figure 49. Effect of nitrogen precursor content (2-6 g HMTA) in metalfree catalyst samples ($HMTA_X$-C-3, x=g of the nitrogen content) on the polarization curves and onset potentials during the electrochemical oxygen reduction reaction (ORR). A) RDE polarization curves, b) onset potential and mass activity. Conditions: 1500 rpm, cathodic scan rate of 10 mV s^{-1}, O_2-saturated 0.1 M KOH at room temperature, NNMCs loading 0.8 mg cm^{-2} 88

Figure 50. Effect of metal precursor content (2-400 g) in metal containing catalyst samples ($HMTA_2$-Fe_x-C-4, x=mg FeAc) and the effect of nitrogen precursor content in metal containing samples ($HMTA_x$-Fe_{40}-C-4, x=2-6 g HMTA) on the polarization curves, onset potentials and mass activity during the electrochemical oxygen reduction reaction (ORR). A) RDE polarization curves, b) onset potential and mass activity. Conditions: 1500 rpm, cathodic scan rate of 10 mV s^{-1}, O_2-saturated 0.1 M KOH at room temperature, NNMCs loading 0.8 mg cm^{-2} 89

Figure 51. ORR catalytic activity of the best performing metalfree and metal containing samples in acid. Polarization curves of $HMTA_2$-Fe_{400}-C-4 (black solid curve) and $HMTA_2$-C-3 (red solid curve) compared to the Pt/C 20wt% (dashed black curve). Conditions: 1500 rpm, O_2-saturated 0.1 M $HClO_4$ (pH 1), room temperature. NNMCs loading of 0.8 mg cm^{-2} compared to Pt/C 20 wt%, 10 µg Pt 91

Figure 52. Tafel plots (E vs. log I_k) in RDE at 1500 rpm, O_2-saturated a) 0.1 M KOH (pH 13) and b) 0.1 M $HClO_4$ (pH 1).....92

Figure 53. Stability cycling tests of the best performing catalysts. Mass activities at 0.8 V vs. RHE in RDE before and after stability test, a) in alkaline, b) in acid electrolytes 93

Figure 54. Schematic of the synthesis procedure for heteroatom-doped carbon material.....97

Figure 55. Molecular structure of different ionic liquid (IL) precursors (systems); a) *N,N*-ethylmethyl-imidazolium-dicyanamide (EMIM-dca) (used as N precursor); b) *N*-methyl-thiazolium-dicyanamide (THIA-dca) (used as S/N precursor); c)tetraethylphosphonium bromide (TEPBr)(used as P containing additive together with (EMIM-dca); d) *N,N*-ethylmethyl-imidazolium-tetracyanoborate (EMIM-tcb) 98

Figure 56. Nitrogen sorption isotherms of different materials synthesized with metal free protocols or using FeCl3 (27 wt% Fe respective to carbon during synthesis) 99

Figure 57. Morphology of support compared with IL-derived catalyst. SEM micrographs of untreated reference (Ketjen_as-received) and S/N_Fe_{27} 101

Figure 58. TEM micrographs of a) Ketjenblack (as-received); b) S/N-metalfree functionalized activated carbons and c) S/N_Fe_{27}. Scale bar is valid for all images 102

Figure 59. Powder XRD patterns of the differently functionalized materials. Left panel: metalfree / Right panel: Fe_{27}-materials. Grey lines indicate database derived Fe_3C diffraction lines.....103

Figure 60. N1s core level XPS spectra of all X/N_metalfree and X/N_Fe27 materials. (x-axes: BE / eV, y-axes: counts/s).....106

Figure 61. XPS core level spectra. Upper panel: S2p for S/N materials; medium panel: P2p for P/N materials; lower panel: B1s for B/N materials. (x-axes: BE / eV; y-axes: counts / s) 107

Figure 62. Effect of metal and its content on ORR electrocatalytic activity of the doped-catalysts. Polarization ORR curves of a) N-metalfree (solid black curve), N_Fe_5 (solid red curve), Pt/C 20 wt% (dashed black curve) and Ketjen (as-received) (dashed red curve). b) different nominal Fe loadings, N_Fe_5 (solid red curve), N_Fe_{10} (solid green), N_Fe_{27} (solid blue curve) compared to N-metalfree (solid black curve). Conditions: O_2-saturated 0.1 M KOH at room temperature, rotating speed 1500 rpm, scan rate 10 mV s^{-1}, non-noble metal catalyst loading 0.8 mg cm^{-2} and Pt loading 10 µg cm^{-2} ..110

Figure 63. Effect of heteroatom type on catalytic activity. Polarization ORR curves of N_Fe_{27} (solid black curve), S/N_Fe_{27} (solid black curve), P/N_Fe_{27} (solid red curve) and B/N_Fe_{27} (solid green curve) compared with Pt/C 20 wt%. Conditions: O_2-saturated 0.1 M KOH, room temperature, rotating

speed 1500 rpm, scan rate 10 mV s^{-1}, non-noble metal catalyst loading 0.8 mg cm^{-2}, Pt loading 10 µg cm^{-2} 111

Figure 64. ORR mass activities at 0.8 V vs. RHE in RDE before and after stability tests measured after 9000 cycles from 0.5 to 1.2 V vs. RHE with the scan rate of 50 mV s^{-1} in 0.1 M KOH at room temperature 112

Figure 65. ORR electrocatalysis of best performing co-doped sample S/N-Fe_{27} Rotating disk electrode (RDE) measurements of S/N_Fe_{27} catalyst in 0.1 M KOH (solid black), in 0.1 M $HClO_4$ (solid red), Pt/C in alkaline (dashed black) and Pt/C in acid (dashed red) 114

Figure 66. ORR mass activities at 0.8 V vs. RHE before and after stability tests 9000 cycles from 0.5 to 1.2 V vs. RHE in 0.1 M KOH compared with 0.1 M $HClO_4$ 114

Figure 67. Chronoamperometry response with 10 % (w/w) methanol injected 150 s after starting the measurement in 0.1 M KOH 115

Figure 68. Course of BET surface area of different catalysts correlated to the corresponding mass activity mA g^{-1} (@0.8 V) 117

Figure 69. Course of elemental composition (heteroatom) of different catalysts correlated to the corresponding mass activity mA g^{-1} (@0.8 V) 118

Figure 70. Synthesis of polyformamidine and the following calcination steps yield a foaming graphitized catalyst 121

Figure 71. XRD patterns of polyformamidine (PFA)-based catalysts with 20 wt% nominal loading (Fe_{20}-CN) calcined at various temperatures varying from 600-900 °C 123

Figure 72. TEM micrographs of catalysts synthesized at a) 600 °C and b) 700 °C 124

Figure 73. Influence of metal on ORR activity of polyformamidine. RDE Polarization curves of PFA-900°C (red curve), Fe20%-PFA-900° (green curve) and commercial Pt/C catalyst (dotted black curve) measured at 1500 rpm in O_2 saturated 0.1 M KOH (pH 13) electrolyte at room temperature. The catalyst loading on the electrode was 0.8 mg cm^{-2} 126

Figure 74. Effect of calcination temperature in ORR activity of different PFA derived catalysts with 20 wt% nominal $FeCl_3$ content. RDE Polarization curves at 1500 rpm in O_2 saturated 0.1 M KOH (pH 13) electrolyte at room temperature. Catalyst loading on the electrode was 0.8 mg cm^{-2} 127

Figure 75. RDE Polarization curves at 1500 rpm, O_2 saturated 0.1 M KOH (pH 13) electrolyte at room temperature, catalyst loading = 0.8 mg cm^{-2}. A) effect of calcination time, b) effect of gas flow during the synthesis 128

Figure 76. Effect of Ketjen nanoparticle addition during catalyst synthesis on ORR activity of $Fe_{2.5wt\%}$-CN-900 °C. RDE Polarization curves at 1500 rpm, O_2 saturated 0.1 M KOH (pH 13) electrolyte at room temperature, catalyst loading = 0.8 mg cm^{-2} 129

Figure 77. Effect of Ketjen nanoparticle addition during catalyst synthesis on ORR activity of $Fe_{2.5wt\%}$-CN-900 °C. RDE Polarization curves at 1500 rpm, O_2 saturated 0.1 M KOH (pH 13) electrolyte at room temperature, catalyst loading = 0.8 mg cm^{-2} 130

Figure 78. Stability tests of best performing catalysts in a) alkaline, b) acid after 9000 cycles, 50 mV s^{-1}, 0.5-1.2 V vs. RHE 131

Figure 79.Chronoamperometry of $Fe_{2.5wt\%}$-CN-900 °C_Ketjen after injection of methanol 132

Figure80. Course of onset potential and graphitization degree of different catalysts 133

List of Tables

Table 1. Comparison of the acidic and alkaline PEFCs 12

Table 2. Summary of precursor composition used in the syntheses of different catalysts with 200 mg Ketjen as-received 29

Table 3. Catalysts ink formulation applied in preparation of thin film optimized for various catalysts 31

Table 4. ICP-OES results of Fe and Mn for final catalysts after 1st acid leaching / 2nd pyrolysis, and Elemental analysis (EA) for nitrogen level in various catalysts in starting precursor and final materials. $Me_{X\ wt\%}$/PANI/Ketjen, X=metal wt% 49

Table 5.Surface area of various catalysts synthesized with different metal composition and contents 56

Table 6. Electrochemical characterization results regarding onset potential (E_{onset}), half wave potential ($E_{1/2}$) and mass activity (I_m) for various mono- and bimetallic catalysts 62

Table 7. Elemental analysis and BET surface area results for different metal containing and metalfree samples at two different synthesis steps, directly after BM and the final catalyst 78

Table 8. Contribution of nitrogen species extracted from XPS technique 83

Table 9. Summary of the E_{onset}, $E_{1/2}$, mass activity (I_m) and Tafel slopes for different catalysts in 0.1 M KOH ..90

Table 10 Composition of different single- and co-doped final catalysts based on elemental combustion analysis (EA) for C, N , S and ICP-OES for P, B, Fe, All values given in wt%. Nitrogen sorption (BET) surface area of differently functionalized carbon samples 100

Table 11. Summary of E_{onset} (onset potential at 1 mA cm^{-2}), I_d and I_m (mass activity at 0.8 V vs. RHE) values for single- and co-doped samples in 0.1 M KOH. Non-noble metal catalyst loadings are 0.8 mg cm^{-2} except for N_Fe_x-2 samples with 0.4 mg cm^{-2} loadings. The RDE experiments were carried out at room temperature, rotating speed 1500 rpm, scan rate 10 mV s^{-1} 113

Table 12. Composition of different single- and co-doped final catalysts based on elemental combustion analysis (EA) for C, N , S and ICP-OES for P, B, Fe and X-ray photoelectron spectroscopy (XPS); all values given in wt% 119

Table 13.electrochemical results regarding E_{onset}, $E_{1/2}$ and mass activity of different catalysts 129

Appendix

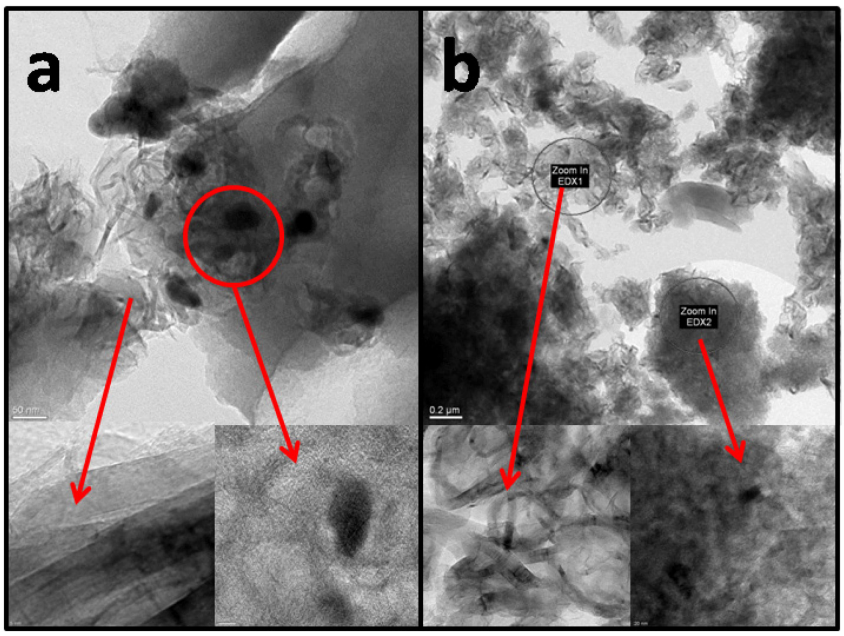

Figure A_1. TEM micrographs of $Fe_{20wt\%}$-CN calcined at 900 °C a) directly after the calcination and b) after acid leaching and 2nd calcination at 900 °C.

References:

1. H.A. Gasteiger, S.S.K., B. Sompalli, F.T. Wagner,, Appl. Catal. BEnviron., 2005. **56**: p. 9.
2. Li, X., Principles of Fuel Cells; Taylor-Francis: New York, , 2006.
3. Rao, A.M., J.; Samuelsen, S. , J. Power Sources 2004. **134**: p. 181–184
4. Lutz, A.E.L., R. S.; Keller, J. O. , Int. J. Hydrogen Energy 2002. **27**: p. 1103–1111.
5. O'hayre, R.C., S.-W.; Colella, W.; Prinz, F. B. , *Fuel Cell Fundamentals; Wiley: New York.* 2006.
6. www.hydrogen.energy.gov/program_records.html, 2013.
7. Bilgen, E., *Domestic hydrogen production using renewable energy.* Solar Energy 2004. **77**: p. 47–55.
8. *Fuel Cell Report to Congress, Multi-Year Research, Development and Demonstration Plan.* February 2003.
9. Koh, S.K., Shirlaine); Strasser, P (Strasser, Peter), *Dealloyed Pt Nanoparticle Fuel Cell Electrocatalysts: Stability and Aging Study of Catalyst Powders, Thin Films, and Inks.* JOURNAL OF THE ELECTROCHEMICAL SOCIETY, 2010. **157**: p. B585-B591.
10. Yang, R.Y., Ruizhi); Leisch, J (Leisch, Jennifer); Strasser, P (Strasser, Peter); Toney, MF (Toney, Michael F.), *Structure of Dealloyed PtCu3 Thin Films and Catalytic Activity for Oxygen Reduction.* CHEMISTRY OF MATERIALS, 2010. **22**: p. 4712-4720.
11. Ratndeep R Srivastava, P.P.M., Nathan N Hahn and Peter P Strasser, *Efficient oxygen reduction fuel cell electrocatalysis on voltammetrically dealloyed Pt-Cu-Co nanoparticles.* Angew Chem Int Ed Engl, 2007. **46(47)**: p. 8988-91
12. Wagner, F.T., Lakshmanan, B.,Mathias, M.F., J. Phys. Chem. Lett., 2010. **1**: p. 2204.
13. F. Hasché, M.O.a.P.S., ChemCatChem, , 2011. **3**: p. 1803–1813.
14. Y. Shao-Horn, W.C.S., S. Chen, P. J. Ferreira, E. F. Holby and D. Morgan, , Top. Catal., 2007. **46**: p. 285–305
15. Xenia Tuaev , J.P.P., René Illgen , Arne Thomas and Peter Strasser, *Nitrogen-doped coatings on carbon nanotubes and their stabilizing effect on Pt nanoparticles.* Phys. Chem. Chem. Phys., 2012. **14**: p. 6444-6447.
16. I. Herrmann-Gepperta, J.R., U.I. Kramma, S. Fiechtera and P. Bogdanoffa, ECS Transactions, 2011. **41 (1)**: p. 1161-1171.
17. Gang Wu, K.L.M., Christina M. Johnston, Piotr Zelenay, *High-Performance Electrocatalystsfor Oxygen Reduction Derivedfrom Polyaniline, Iron, and Cobalt.* Science, 2011. **332**: p. 443-447.
18. Jose H. Zagal, F.B., Jean-PolDodelet, *N_4-Macrocyclic Metal Complexes.* 2006.
19. Jasinski, R., Nature, 1964. **201(492**: p. 1212-3.
20. Sen RK, Z.J., Yeager E, Inorganic Chemistry, 1977. **16(12)**: p. 3379e80.
21. H., J., *Cathode reduction of oxygen on organic catalysts in sulfuric acid.* Berichte Der Bunsen-Gesellschaft für physikalische chemie, 1968. **72(8)**: p. 1053.
22. Andr´easson, J., A. Kyrychenko, J. M˚artensson, and B. Albinsson, Photochem. Photobiol. Sci., 2002. **1(2)**: p. 111–119.
23. weiss, E.A., M.J.Ahrens, L.E. Sinks, A.V. Gusev, M.A. Ratner, and M.R. Wasielewski, J. Am. Chem. Soc. , 2004(126(17)): p. 5577–5584.
24. L. Zhang, J.J.Z., D.P. Wilkinson, H.J. Wang, J. Power Sources, 2006. **156**: p. 171.
25. Wang, B., Journal of Power Sources, 2005. **152**: p. 1-15.
26. Gang Liu , X.L., Jong-Won Lee and Branko N. Popov *A review of the development of nitrogen -modified carbon-based catalysts for oxygen reduction at USC.* Catal. Sci. Technol, 2011. **1**: p. 207-217.

27. J. Marcinkoski, J.P.K.a.T.G.B., *Progress in the US DOE fuel cell subprogram efforts in polymer electrolyte fuel cells.* nt. J Hydrogen Energy, 2008. **33**: p. 3894–902
28. M. Lefevre, E.P., F. Jaouen and J. P. Dodelet, Science, 2009. **324**: p. 71–74.
29. Nalini P. Subramanian, X.L., Vijayadurda Nallathambi, Swaminatha P. Kumaraguru, Hector Colon-Mercado, Gang Wu, Jong-Won Lee, Branko N. Popov, Journal of Power Sources, 2009. **188**: p. 38-44.
30. Khomenko, V.G.B., V. Z.; Katashinskii, A. S., Elechtrochim. Acta, 2005. **50**: p. 1675.
31. Rajesh, B.Z., P., *A Class of Non-precious Metal CompositeCatalysts for Fuel Cells.* Nature, 2006. **443**: p. 63–66.
32. L. X. Liu Gang, G.P., N. Popov Branko., , Applied Catalysis B: Environmental, , 2009. **93,156e65,**: p. 25.
33. Gang Wu, Z.C., Kateryna Artyushkova, Fernando H. Garzon, and a.P. Zelenay, *Polyaniline-derived Non-Precious Catalyst for the Polymer Electrolyte Fuel CellCathode.* ECS Transactions, 2008. **16 (2)** p. 159-170
34. Liu H, S.Z., Zhang J, Zhang L, Zhang J., Journal of Materials Chemistry, 2009. **19(4)**: p. 468-70.
35. Shuangyin Wang, E.I., Ajit Roy, Yuhua Xue, Dingshan Yu, and Liming Dai, Angew. Chem. Int. Ed. , 2011. **50**: p. 11756 –11760.
36. Asao, O.J.-i.A.T.K.N.O., Carbon, 2006. **44**: p. 3358-3361.
37. Zhen-Huan Sheng , H.-L.G., Wen-Jing Bao , Feng-Bin Wang and Xing-Hua Xia, J. Mater. Chem. , 2012. **22**: p. 390-395.
38. Jiao Wu, Z.Y., Xiaowei Li, Qijun Sun, Chao Jin, Peter Strasser and Ruizhi Yang, Journal of Materials Chemistry A, 2013. **1**: p. 9889–9896.
39. Sendt, K., L.A. Johnston,W.A. Hough, M.J. Crossley, N.S. Hush, and J.R. Reimers, J. Am. Chem. Soc., 2002. **124(31)**: p. 9299–9309.
40. Zimmermann, J., U. Siggel, J.-H. Furhop, and B. R¨oder, J. Phys. Chem. , 2003. **107(25)**: p. 6019–6021.
41. Pescitelli, G., S. Gabriel, Y. Wang, J. Fleischauer, R.W. Woody,and N. Berova, J. Am. Chem.Soc., 2003. **125(25)**: p. 7613–7628.
42. P.H. Matter, L.Z., U.S. Ozkan, J. Catal., 2006. **239**: p. 83.
43. P.H. Matter, E.W., M. Arias, E.J. Biddinger, U.S. Ozkan, J. Phys. Chem. B, 2006. **110**: p. 18374–18384.
44. Matter, P.H.Z., L.; Ozkan, U. S., J. Catal., 2006. **239**: p. 83.
45. Matter, P.H.W., E.; Arias, M.; Biddinger, E. J.; Ozkan, U. S., J. Phys. Chem. B, 2006. **110**: p. 18374.
46. Ulrike I. Kramm, J.H., a Nicholas Larouche,a Thomas M. Arruda, Michel Lefe` vre,a Fre´de´ ric Jaouen,a Peter Bogdanoff,b Sebastian Fiechter, Irmgard Abs-Wurmbach, Sanjeev Mukerjeec and Jean-Pol Dodelet, *Structure of the catalytic sites in Fe/N/C-catalysts for O2-reduction in PEM fuel cells.* Phys. Chem. Chem. Phys., 2012. **14**: p. 11673–11688.
47. Dodelet, F.d.r.J.a.J.-P., *Non-Noble Electrocatalysts for O2 Reduction: How Does Heat Treatment Affect TheirActivity and Structure? Part I. Model for Carbon Black Gasification by NH3: ParametricCalibration and Electrochemical Validation.* J. Phys. Chem. C, 2007. **111**: p. 5963-5970.
48. Lefe`vre, M.D., J. P.; Bertrand, P., J. Phys. Chem. B, 2002. **106**: p. 8705.
49. Dieter von Deak, D.S., Jesaiah C. King, Umit S. Ozkan, *Use of carbon monoxide and cyanide to probe the active sites on nitrogen-dopedcarbon catalysts for oxygen reduction.* Applied Catalysis B: Environmental, 2012. **113-114**: p. 126-133.
50. Matthew S. Thorum, J.M.H., and Andrew A. Gewirth, *Poisoning the Oxygen Reduction Reaction on Carbon-Supported Fe and Cu Electrocatalysts:Evidence for Metal-Centered Activity*J. Phys. Chem. Lett., 2011. **2**: p. 295-298.

51. A.A. Serov, M.M., G. Chai, S. Han, S.J. Seo, Y. Park, H. Kim, C. Kwak, J. Appl.Electrochem. Commun., 2009. **39**: p. 1509–1516.
52. C. Ruzie, P.E., D. Ricard, T. Roisnel, B. Boitrel, Inorg. Chem., 2006. **45**: p. 1338–1348.
53. I.T. Bae, D.S., J. Phys. Chem. B, 1998. **102**: p. 2519–2522.
54. L. Birry, J.H.Z., J.P. Dodelet, Electrochem. Commun., 2010. **12**: p. 628–631.
55. Grove, W.P.M., J. Sci. , 1839. **14**.
56. Schoenbein, C.F., Phil. Mag. , 1839: p. 43-45.
57. Spiegel, C.S., Designing and Building Fuel Cells. Mcgraw-Hill Professional: 2007.
58. Penner, S.S., Assessment of Research Needs for Advanced Fuel Cells;Pergamon Press: Oxford, U.K.,, 1986. **11**: p. 1-2.
59. McLean, G.F.N., T.; Prince-Richard, S.; Djilali, N.,, *An assessment of alkaline fuel cell technology.* International Journal of Hydrogen Energy, 2002. **27,(5)**: p. 507-526.
60. Kinoshita, K., *Electrochemical Oxygen Technology, Wiley: New York,.* 1992: p. p 448.
61. Varcoe, J.R.S., R. C. T.; Yee, E. L. H. , Chem. Commun., 2006. **1428**.
62. Slade, R.C.T.V., J. R. , Solid State Ionics 2005. **176**: p. 585.
63. Spendelow, J.S.W., A. Phys. Chem. Chem. Phys. , 2007. **9**: p. 2654.
64. Rempel, U., B. Vonmaltzan, and C. von Borczyskowski Chem. Phys. Lett., 1995. **245**: p. 253-261.
65. Lee, P.C.a.D.M., J. Phys. Chem. , 1982. **86**: p. 3391.
66. Jennings, C.A., J. Kovac, and R. Aroca Langmuir, 1993. **9**: p. 2151.
67. Chang, R.K., Ber. Bunsen Phys. Chem., 1987. **91**: p. 296.
68. Jennings, C.A., J. Kovac, and R. Aroca *Near-infrared surface-enhanced Raman scattering from metal island films.* J. Phys. Chem., 1992. **96**: p. 1340.
69. Fleischmann, M., P.J. Hendra, and A.J. McQuillan Chem. Phys. Lett., 1974. **26**: p. 163.
70. Harstein, A., J.R. Kirtley, and J.C. Tsang Phys. Rev. Lett., 1980. **45**: p. 201.
71. Osawa, M.a.M.I., J. Phys. Chem., 1991. **95**: p. 9914.
72. S. Gupta, D.T., I. Bae, W. Aldred and E. Yeager, J. Appl. Electrochem., 1989. **19**: p. 19-27.
73. Taylor, H.S., *The role of these three kinds of active sites in promoting selective catalytic transformations has ... In the case of heterogeneous catalysis, the concept of active centre has many manifestations.* Proc Roy Soc., 1952. **A108**: p. 105-111.
74. G. Liu, X.L., P. Ganesan and B. N. Popov, *Studies of oxygen reduction reaction active sites and stability of nitrogen-modified carbon composite catalysts for PEM fuel cells.* Electrochim. Acta, 2010. **55**: p. 2853–8.
75. Mukerjee, N.R.a.S., J. Phys. Chem. C 2011. **115** p. 18015–18026.
76. SanjeevMukerjee, N.R.a., Advances in Physical Chemistry. **Volume 2012**: p. 17 pages.
77. Yeager, E., Elechtrochim. Acta, 1984. **29**: p. 1527.
78. Yeager, E., *Dioxygen electrocatalysis: mechanisms in relation to catalyst structure.* J Mol. Catal., 1986. **38**: p. 5–25
79. Wiesener, K., *N4-chelates as electrocatalyst for cathodic oxygen reduction.* Electrochim. Acta, 1986. **31**: p. 1073–8.
80. V. Nallathambi, X.L., J. W. Lee and B. N. Popov, *Development of nitrogen-modified carbon-based catalysts for oxygen reduction in PEM fuel cells.* ECS. Trans., 2008. **16**: p. 405–17.
81. N. P. Subramanian, X.L., V. Nallathambi, S. P. Kumaraguru, H. Colon-Mercado, G. Wu, J. W. Lee and B. N. Popov, *Nitrogen-modified carbon-based catalysts for oxygen reduction reaction in polymer electrolyte membrane fuel cells.* Power Sources, 2009. **188**: p. 38–44.
82. Gojkovic, S.G., S.; Savinell, R., J. Electroanal. Chem., 1999. **462**: p. 63.
83. Gouerec, P.B., A.; Contamin, O.; Scarbeck, G.; Savy, M.; and J.W. Riga, L. T.; Bertrand, P., 1997. **422**: p. 61.
84. Wiesener, K., Elechtrochim. Acta, 1986. **31**: p. 1073.
85. P.H. Matter, U.S.O., Catal. Lett., 2006. **109**: p. 115–123.

86. A. L. Bouwkamp-Wijnoltz, W.V., J. A. R. van Veen, and and S.C. Tang, Electrochimica Acta, 1999. **45**: p. 379–386.
87. A. L. Bouwkamp-Wijnoltz, W.V., J. A. R. van Veen, E., A.M.v.d.K. Boellaard, and S. C. Tang , and p. 50, 2002., Journal of Physical Chemistry B, 2002. **106**: p. 12993–13001.
88. A. L. Bouwkamp-Wijnoltz, W.V., and J. A. R. van Veen, , Electrochimica Acta, 1998. **43**: p. 3141–3152.
89. J. McBreen, W.E.O.G., D. E. Sayers, C. Y. Yang, and K. and S.S. I. Pandya, S. Wagner, and H. Wroblowa,Eds, The Electrochemical Society, Pennington, NJ, USA. **87**: p. 182.
90. H. Schulenburg, S.S., V. Sch¨unemann et al., , Journal of Physical Chemistry B, 2003. **107**: p. 9034–9041.
91. M. Lefèvre, J.P.D.a.P.B., *Molecular oxygen reduction in PEM fuel cells: Evidence for the simultaneous presence of two active sites in Fe-based catalysts.* J Phys. Chem. B, 2002. **106**: p. 8705–13.
92. M. Lefevre, J.P.D., Elechtrochim. Acta, 2003. **48**: p. 2749.
93. M. Lefevre, J.P.D., and P. Bertrand, , Journal of Physical Chemistry B, 2000. **104**: p. 11238–11247.
94. M. Lef`evre, J.P.D., and P. Bertrand Journal of Physical Chemistry B, 2002. **106**: p. 8705–8713.
95. M. Lef`evre, E.P., F. Jaouen, and J. P. Dodelet, , Science, 2009. **324**: p. 71-74.
96. Lalande, G.C.t., R.; Guay, D.; Dodelet, J. P.; Weng, L. T.; and P. Bertrand, Electrochim. Acta, 1997. **42**: p. 1379.
97. G. Lalande, R.C.o.e., D. Guay, J. P. Dodelet, L. T. Weng, and P. Bertrand, Electrochimica Acta, 1997. **42**: p. 1379–1388.
98. . Lalande, R.C., G. Tamizhmani, D. Guay, J. P. Dodelet, L. Dignard-Bailey, L. T. Weng and P. Bertrand, *Physical, chemical and electrochemical characterization of heat-treated tetracarboxylic cobalt phthalocyanine adsorbed on carbon black as electrocatalysts for oxygen reduction in polymer electrolyte fuel cells.* Electrochim. Acta, 1995. **40**: p. 2635–46.
99. Ch, R.V., Viswanathan B, The Journal of Physical Chemistry C, 2007. **111(44)**: p. 16538e43.
100. Meier H, T.U., Zimmerhackl E, Albrecht W., Investigation of acid resistant electrocatalysts for fuel cell.Rep. No. BMV g-FBWT, 1975: p. 75.-6.
101. R. Baker, D.P.W.a.J.Z., *Electrocatalytic activity and stability of substituted iron phthalocyanines towards oxygen reduction evaluated at different temperatures.* Electrochim. Acta, 2008. **53**: p. 6906–19.
102. Heilgendorff MH, D.I., Schulenburg H, Bron M, Fiechter S, Bogdanoff P, Tributsch H, et al, Platinum-free chelatecatalyst material for the selective reduction of oxygen and method for production thereof., 2004:.
103. Pylypenko S, M.S., Olson TS, Atanassov P., Electrochimica Acta, 2008. **53(27)**: p. 7875-83.
104. Gojkovic SL, G.S., Savinell RF., Electrochimica Acta, 1999. **45(6)**: p. 889-97.
105. Martinez Millan WM, S.M., Journal of Applied Polymer Science, 2009. **112(5)**: p. 2959-67.
106. C.J. Chang, L.L.C., D.G. Nocera, J. Am. Chem. Soc., 2003. **125**: p. 1866–1876.
107. S. L. Gojković, S.G.a.R.F.S., *Heat-treated iron(III) tetramethoxyphenyl porphyrin chloride supported on high-area carbon as an electrocatalyst for oxygen reduction:: Part III Detection of hydrogen-peroxide during oxygen reduction.* Electrochim. Acta, 1999. **45**: p. 889–97.
108. Suzuki, K.S.a.N., *Heat-treated transition metal hexacyanometallates as electrocatalysts for oxygen reduction insensitive to methanol.* J Electrochem. Soc., 2004. **151(5)**: p. A682–88.
109. S. Yamazaki, Y.Y., T. Ioroi, N. Fujiwara, Z. Siroma, K. Yasuda and Y. Miyazaki, *Estimation of specific interaction between several Co porphyrins and carbon black: its influence on the electrocatalytic O2 reduction by the porphyrins.* J Electroanal. Chem, 2005. **576**: p. 253–9
110. Bashyam R, Z.P., Nature, 2006. **443**: p. 7107.
111. B.C.H. Steele, A.H., Nature, 2001. **414**: p. 345.

112. F. Jaouen, F.C., J.P. Dodelet, J. Electrochem. Soc., 2006. **153**: p. 689.
113. Yuyan Shao, J.S.c., Geping Yin a, Yunzhi Gao, Applied Catalysis B: Environmental, 2008. **79**: p. 89-99.
114. V.V. Strelko, V.S.K., P.A. Thrower, Carbon, 2000. **38**: p. 1499.
115. H.J. Burch, J.A.D., E. Brown, L. Hao, S.A. Contera, N. Grobert, J.F.Ryan, Appl. Phys. Lett., 2006. **89**: p. 143110.
116. M. Terrones, A., Rev. Mater. Res., 2003. **33**: p. 419.
117. M. Terrones, P.R., N. Grobert, S. Trasobares, W.K. Hsu, H. Terrones, Y.Q. Zhu, J.P. Hare, C.L. Reeves, A.K. Cheetham, M. Ruhle, H.W. Kroto, D.R.M. Walton, Adv. Mater., 1999. **11**: p. 655.
118. A.B. Fuertes, S.A., Carbon, 2004. **42**: p. 3049.
119. Calle-Vallejo F, M.J., Rossmeisl J., *Density functional studies of functionalized graphitic materials with late transition metals for Oxygen Reduction Reactions.* Phys Chem Chem Phys., 2011 **13(34)**: p.:15639-43.
120. Jens Peter Paraknowitsch , A.T.a.M.A., J. Mater. Chem. , 2010. **20**: p. 6746-6758.
121. S. S. Zhang, X.Z.Y., J. N. C. Hin, H. J. Wang, K. A. Friedrich and M. Schulze, J. Power Sources, 2009. **194**: p. 588-600.
122. K. J. J. Mayrhofer, J.C.M., S. J. Ashton, G. K. H. Wiberg, F. Kraus, M. Hanzlik and M. Arenz, Electrochem. Commun., 2008. **10**: p. 1144–1147.
123. Ozkan, P.H.M.a.U.S., Catal. Lett., 2006. **109**: p. 115-123.
124. R.A. Sidik, A.B.A., N.P. Subramanian, S.P. Kumaraguru, B.N. Popov, J. Phys. Chem. B, 2006. **110**: p. 1787.
125. C.L. Sun, L.C.C., M.C. Su, L.S. Hong, O. Chyan, C.Y. Hsu, K.H. Chen, T.F. Chang, L. Chang, Chem. Mater., 2005. **17**: p. 3749.
126. P.H. Matter, E.W., J.-M.M. Millet, U.S. Ozkan, J. Phys. Chem. C, 2007. **111**: p. 1444–1450.
127. 1Yuchen Ma, A.S.F., A. V. Krasheninnikov, and R. M.Nieminen, Phys. Rev. B, 2005. **72**: p. 205416.
128. Chakraborty, J.B.a.T., Phys. Rev. B 2009. **80**: p. 115430.
129. 3S. F. Huang, K.T., T. Ozaki, T. Ikeda, M. Boero, M. Oshima, J. Ozaki, and S. Miyata, Phys. Rev. B 2009. **80**: p. 235410.
130. H. Wang, T.M.a.X.W., ACS Catal., 2012. **2**: p. 781–794.
131. P.H. Matter, E.W., U.S. Ozkan, J. Catal. , 2006. **243** p. 395–403.
132. Stanislav R. Stoyanova, b., Alexey V. Titova, Petr Krála, Coordination Chemistry Reviews, 2009. **253**: p. 2852–2871.
133. Haibo Wang, T.M., and Xin Wang, *Review on Recent Progress in Nitrogen-Doped Graphene: Synthesis,Characterization, and Its Potential Applications.* Catal. Sci. Technol, 2012. **2**: p. 781−794.
134. K. Gong, F.D., Z. Xia, m. Durstock, L. Dai, Science, 2009. **323**: p. 760.
135. Matter, P.H.W., E.; Arias, M.; Biddinger, E. J.; Ozkan, U. S., *Oxygen Reduction Reaction Activity and Surface Propertiesof Nanostructured Nitrogen-Containing Carbon.* . J. Mol. Catal.A: Chem., 2007. **264**: p. 73–81.
136. Faubert, G.C.t., R.; Dodelet, J. P.; Lefe`vre, M.; Bertrand, P., Electrochim. Acta, 1999. **44**: p. 2589.
137. Herranz, J.J., F.; Lefevre, M.; Kramm, U. I.; Proietti, E.; Dodelet, J.-P.; Bogdanoff, P.; Fiechter, S.; Abs-Wurmbach, I.; Bertrand, P.; Arruda, T.; Mukerjee, S. , J. Phys. Chem. C 2011. **115**: p. 16087.
138. Maldonado, S.S., K. J., *Influence of Nitrogen Dopingon Oxygen Reduction Electrocatalysis at Carbon NanofiberElectrodes.* J. Phys. Chem. B, 2005. **109**: p. 4707–4716.
139. M. Lefevre, E.P., F. Jaouen, J.-P. Dodelet, Science, 2009. **324** p. 71–74.

140. Biddinger, E.v.D., D.; Ozkan, U., *Nitrogen-ContainingCarbon Nanostructures as Oxygen-Reduction Catalysts.* Top.Catal. , . 2009. **52**: p. 1566–1574.
141. Jang-Soo Lee, G.S.P., Sun Tai Kim, Meilin Liu, and Jaephil Cho, Angew. Chem. Int. Ed., 2013. **52**: p. 1026 –1030.
142. C. W. B. Bezerra, L.Z., K. Lee, H. Liu, A. L. B. Marques,E. P. Marques, H. Wang and J. Zhang, Electrochim. Acta, 2008. **53**: p. 4937–4951.
143. D. B. Sepa, M.V.V., L. M. Vracar, and A. Damjanovic, Electrochimica Acta, 1987. **32**: p. 129–134.
144. A. Damjanovic, M.A.G., and J. O'M Bockris, , The Journal of Chemical Physics, 1966. **45**: p. 4057–4059.
145. H. S. Wroblowa, Y.-C.P., and G. Razumney, Journal of Electroanalytical Chemistry, 1976. **69**: p. 195–201.
146. N. A. Anastasijevi´c, V.V.c., and R. R. Adˇzi´c, Journal of Electroanalytical Chemistry, 1987. **229**: p. 305–316.
147. Adzic, R.I.E.L., J., Ross, P. N., Eds.;Wiley-VCH: New York,, 1998: p. 197.
148. Strbac, S., Electrochim. Acta. **56**: p. 1597.
149. Tarasevich, M.R.S., A.; Yeager, E. In Comprehensive Treatise of Electrochemistry; Conway, B. E., Bockris, J. O. M., Yeager, E.,Eds.; Plenum Press: New York, 1983. **7**: p. 301.
150. Blizanac, B.B.R., P.N.;Markovic,N.M. 2264., Electrochim. Acta, 2007. **52**: p. 2264.
151. Jens Peter Paraknowitsch, B.W., Yuanjian Zhang, and Arne Thomas, Chem. Eur. J. , 2012. **18**: p. 15416 – 15423.
152. Stephan Enthaler, S.K., Jan Dirk Epping,b Björn Eckhardt, Steffen M. Weidnerd and a.A. Fischer, Polymer Chemistry, 2012. **3**: p. 751.
153. Knop-Gericke, A., et al., *Chapter 4 X-Ray Photoelectron Spectroscopy for Investigation of Heterogeneous Catalytic Processes*, in *Advances in Catalysis*, C.G. Bruce and K. Helmut, Editors. 2009, Academic Press. p. 213-272.
154. Alexey Serov, M.H.R., Mayat Smolnik, Plamen Atanassov, Electrochimica Acta 2012. **80**: p. 213–218.
155. H. E. King and C. T. Prewitt, A.C.B., 1982. **38**: p. 1877.
156. al., C.e., Green Chem., 2011. **13**: p. 406-412.
157. al., B.e., Carbon. **40**: p. 1521-1531.
158. al., P.e., Energ. Fuel., 2006. **20**: p. 1275-1280.
159. al., H.e., Carbon, 2003. **41**: p. 951-957.
160. XPS Database 20, V., Nat. Inst. of Standards and Technology, Gaithersburg.
161. G. Wu, K.L.M., C.M. Johnston and P. Zelenay, Science, 2011. **332**: p. 443.
162. Thomas, A., Angew. Chem. Int. Ed. , 2010. **49**: p. 8328 – 8344.
163. Tan Xing, J.S., Wenrong Yang, Yongbai Yin, Alexey M. Glushenkov,Lu Hua Li, Patrick C. Howlett and Ying Chen, *Ball milling: a green mechanochemical approach for synthesis of nitrogen doped carbon nanoparticles.* Nanoscale, 2013. **5**: p. 7970–7976.
164. S. L. James, C.J.A., C. Bolm, D. Braga, P. Collier,T. Friscic, F. Grepioni, K. D. M. Harris, G. Hyett, W. Jones,A. Krebs, J. Mack, L. Maini, A. G. Orpen, I. P. Parkin,W. C. Shearouse, J. W. Steed and D. C. Waddell Chem. Soc.Rev., 2012. **41**: p. 413-447.
165. Kaupp, G., CrystEngComm, 2019. **11**: p. 388-403.
166. Eric Proietti, F.J., Michel Lefèvre, Nicholas Larouche, Juan Tian, Juan Herranz & Jean-Pol Dodelet, *Iron-based cathode catalyst with enhanced power density in polymer electrolyte membrane fuel cells.* Nature communications, 2011.
167. Y. Chen, M.C., J. Williams and J. Zou, J. Mater. Res.,, 2002. **17**: p. 1896–1899.
168. L. Li, L.H.L., Y. Chen, X. J. Dai, T. Xing, M. Petravic and X. Liu, Nanoscale Res. Lett., 2012. **7**: p. 417.

169. Tim-Patrick Fellinger, F.r.H., Peter Strasser, and Markus Antonietti, |J. Am. Chem. Soc, 2012. **134**: p. 4072−4075.
170. Zhi Yang, Z.Y., Guifa Li,Guoyong Fang,Huagui Nie, Zheng Liu,Xuemei Zhou,Xi'an Chen, and Shaoming Huang, ACS NANO, 2012. **6**: p. 205-211.
171. Thomas, J.P.P.a.A., Energy Environ. Sci. , 2013. **6**: p. 2839–2855
172. Pasquale F. Fulvio, J.S.L., Richard T. Mayes, Xiqing Wang,Shannon M. Mahurina and Sheng Dai, Phys. Chem. Chem. Phys.,, 2011. **13**: p. 13486–13491.
173. P. Walden, i.B.A.S.S.P., 405–422.
174. Hua Zhao, S.X.a.P.M., 2005. **80**: p. 1089–1096
175. Shengdong Zhu, Y.W., Qiming Chen, Ziniu Yu, Cunwen Wang, Shiwei Jin, Yigang Dinga and Gang Wu, Green Chem., 2006. **8**: p. 325–327
176. Michel Armand, F.E., Douglas R. MacFarlane, Hiroyuki Ohno & Bruno Scrosati, Nature Materials, 2009. **8**: p. 621-629.
177. Zhao, D.W., M.; Kou, Y.; Min, E., Catalysis Today, 2002. **74**: p. 157-189.
178. Jens Peter Paraknowitsch, A.T., Macromol. Chem. Phys. , 2012. **213**: p. 1132−1145.
179. G.Q. Lu, X.s.Z., eds, Nanoporous Materials: Science and Engineering, Imperial college Press, chapter 11, 2004.
180. J. Am. Chem. Soc., 1940. **62**: p. 1723-1732.
181. Wen Yang, T.-P.F., and Markus Antonietti, J. AM. CHEM. SOC. , 2011. **113**: p. 206–209.
182. Jens Peter Paraknowitsch, J.Z., Dangsheng Su, Arne Thomas, and Markus Antonietti, Adv. Mater., 2010. **22**: p. 87–92.
183. Tim-Patrick Fellinger, D.S.S., Markus Engenhorst, Devendraprakash Gautam, Robert Schloegl and Markus Antonietti, J. Mater. Chem., 2012. **22**: p. 23996.
184. Powder Diffraction File, v., The International Centre for Diffraction Data,2009.
185. Moulder, S., Sobol, Bomben, IN: Handbook of X-ray photoelectron spectroscopy, Ed.: J. Chastain, Perkin-Elmer, Eden Prairie, 1992.
186. Physica Scripta. Vol. 1, -., year 1970, X-ray Photoelectron Spectroscopy Database 20, version 3.0, National Institute of Standards and Technology, Gaithersburg.
187. Carl W. Liskey, X.L., and John F. Hartwig, J. AM. CHEM. SOC., 2010. **132**: p. 11389–11391
188. XPS database, C., lasurface.com, Thin Solid Films 538 (2013) 21–24.
189. Jacobsohn, L.G.S., R. K.; Maia da Costa, M. E. H.; Nastasi, M., Surface Science, 2004. **527**: p. 418-424.
190. Lee, J.-S.P., G. S.; Kim, S. T.; Liu, M.; Cho, J. , Angewandte Chemie (International ed. in English), 2013. **52**: p. 1026–30.